AD_____

Award Number: DAMD17-00-1-0455

TITLE: Scanning Microwave Induced Acoustic Tomography

PRINCIPAL INVESTIGATOR: Lihong Wang, Ph.D.

CONTRACTING ORGANIZATION: Texas Engineering Experiment Station
College Station, Texas 77843-3000

REPORT DATE: October 2003

TYPE OF REPORT: Annual

20040203 031

PREPARED FOR: U.S. Army Medical Research and Materiel Command
Fort Detrick, Maryland 21702-5012

DISTRIBUTION STATEMENT: Approved for Public Release;
Distribution Unlimited

The views, opinions and/or findings contained in this report are
those of the author(s) and should not be construed as an official
Department of the Army position, policy or decision unless so
designated by other documentation.

REPORT DOCUMENTATION PAGE

Public reporting burden for this collection of information is estimated to average 1 hour per response, including the time for reviewing instructions, searching existing data sources, gathering and maintaining the data needed, and completing and reviewing this collection of information. Send comments regarding this burden estimate or any other aspect of this collection of information, including suggestions for reducing this burden to Washington Headquarters Services, Directorate for Information Operations and Reports, 1215 Jefferson Davis Highway, Suite 1204, Arlington, VA 22202-4302, and to the Office of Management and Budget, Paperwork Reduction Project (0704-0188), Washington, DC 20503

1. AGENCY USE ONLY (Leave blank)	2. REPORT DATE October 2003	3. REPORT TYPE AND DATES COVERED Annual (1 Oct 2002 – 30 Sep 2003)

4. TITLE AND SUBTITLE
Scanning Microwave Induced Acoustic Tomography

5. FUNDING NUMBERS
DAMD17-00-1-0455

6. AUTHOR(S)
Lihong Wang, Ph.D.

7. PERFORMING ORGANIZATION NAME(S) AND ADDRESS(ES)
Texas Engineering Experiment Station
College Station, Texas 77843-3000

E-Mail: lwang@tamu.edu

8. PERFORMING ORGANIZATION REPORT NUMBER

9. SPONSORING / MONITORING AGENCY NAME(S) AND ADDRESS(ES)
U.S. Army Medical Research and Materiel Command
Fort Detrick, Maryland 21702-5012

10. SPONSORING / MONITORING AGENCY REPORT NUMBER

11. SUPPLEMENTARY NOTES

12a. DISTRIBUTION / AVAILABILITY STATEMENT
Approved for Public Release; Distribution Unlimited

12b. DISTRIBUTION CODE

13. ABSTRACT (Maximum 200 Words)
Since the previous report in 2002, we have published five peer-reviewed journal articles and delivered 12 invited talks. For the invited plenary talk given at UK, all travel related expenses were covered by the conference host.

The combination of ultrasound and microwave has provided us a unique opportunity for early-cancer imaging with high resolution and high contrast. A good imaging modality should have both high contrast and high spatial resolution. Our imaging technology combines synergistically radiofrequency waves and ultrasonic waves, where the former provides high contrast and the latter provides high spatial resolution. Only non-ionizing radiation is used. No painful breast compression is required. In addition, our images are free of speckle artifacts, which are prevalent in conventional ultrasound images. Our ultimate goal is to detect early breast cancer. Specifically, we have made further progress in the reconstruction alogrithims (MP Aug. 2002 and IEEE-TBE 2003), in the mechanism of spatial resolution (PR 2003), in the understanding of heterogeneity (IEEE-UFFC 2003), and in extending the technology to other electromagnetic sources (MP Dec. 2002). We have also images several mastectomy specimens at M.D. Anderson Cancer Center in Houston.

14. SUBJECT TERMS Detection, photoacoustic effect, microwave, ultrasonography	15. NUMBER OF PAGES 79
	16. PRICE CODE

17. SECURITY CLASSIFICATION OF REPORT Unclassified	18. SECURITY CLASSIFICATION OF THIS PAGE Unclassified	19. SECURITY CLASSIFICATION OF ABSTRACT Unclassified	20. LIMITATION OF ABSTRACT Unlimited

Table of Contents

Introduction

A novel imaging technology, scanning microwave-induced-acoustic tomography, will be developed for breast imaging. X-ray mammography and ultrasonography are the current clinical tools for breast-cancer screening and detection. Mammography is the "gold standard", however, uses ionizing radiation and has difficulties imaging pre-menopausal breasts, which are radiographically dense. Ultrasonography is an adjunct tool to x-ray mammography and cannot detect many of the nonpalpable tumors. The cure rate of breast cancers is improved if they are detected early. To provide a new non-invasive, non-ionizing diagnostic tool for detection of early breast cancers, we will develop real-time microwave-induced-acoustic tomography for breast imaging. Microwave-induced-acoustic tomography is based on the photoacoustic effect, generation of acoustic wave by deposition of short-pulse electromagnetic energy safely into biological tissues. The microwave for this technology is short-pulsed, and its power is within the IEEE safety limits. The microwave-induced acoustic wave is then detected with an ultrasonic detector for imaging. The contrast between tumors and normal tissues in the microwave regime is significantly better than other imaging modalities. Cancerous breast tissues are found to be 2-5 times more strongly absorbing than surrounding normal breast tissues in the microwave, which has been attributed to an increase in bound water and sodium within malignant cells. However, pure-microwave imaging is fundamentally limited to poor resolution (on the order of 10 mm) because of the large wavelength of microwave. Ultrasonic imaging has good resolution (on the order of 1 mm) but has a poor contrast between tumors and normal tissues. Microwave-induced-acoustic tomography combines the contrast advantage of pure-microwave imaging and the resolution advantage of pure-ultrasonic imaging, therefore, has the potential for detection of early breast cancers and for assessing and monitoring treatments as well.

Body

In this section, we present our study of pulsed-microwave-induced thermoacoustic tomography in biological tissues. A short-pulsed microwave source was used to irradiate the tissue samples, and the thermoacoustic waves excited by thermoelastic expansion were then measured by a wide-band ultrasonic transducer along a circular path that encloses the sample under study. The acquired data were then used to reconstruct the microwave absorption distribution. Both an exact reconstruction solution and an approximate modified backprojection algorithm were derived. Experiments demonstrated that the images calculated by the backprojection method agreed with the original samples very well, and the spatial resolution in reconstruction was as good as 0.5 millimeter (500 micrometers).

Introduction to thermoacoustic tomography

In thermoacoustic tomography, a short-pulsed microwave source is used to irradiate the tissue. Absorbed microwave energy causes thermoelastic expansion and radiates thermoacoustic waves from within the irradiate tissue. The relatively long wavelength of the microwave, e.g., ~3 cm at 3 GHz in tissues, serves to illuminate the tissue homogeneously. The microwave heating must be rapid to produce thermoacoustics waves; in other words, static temperature distribution or slow heating cannot produce thermoacoustic waves. A wide-band ultrasonic transducer can then be employed to acquire the thermoacoustic signals excited by thermoelastic expansion, which carries the microwave absorption property of the tissue. The ultrasonic transducer is very sensitive in detecting small vibrations from an object that are caused by weak energy absorption.

The key problem with this technique is how to determine the microwave absorption distribution from the measured data, i.e., how to map the inhomogeneity of the tissue. One approach is to use focused ultrasonic transducers to localize the thermoacoustic sources in linear or sector scans and then construct the images directly from the data as is often done in pulse-echo ultrasonography. An alternative method is to use wide-band unidirectional point detectors to acquire thermoacoustic data and then reconstruct the microwave absorption distribution. To date, we have not seen an exact inverse solution for this specific problem, although some researchers have arrived at approximate reconstruction algorithms, such as the weighted delay-and-sum method, the optimal statistical approach, and the Radon transform in far field approximation.

Based on spherical harmonic functions, we first deduced an exact solution of the problem in the three-dimensional case, which can be carried out in the frequency domain. We assume that the wide-band unidirectional ultrasonic transducer is set on a spherical surface, which encloses the sample under investigation. The data acquired from different directions are sufficient to allow us to reconstruct the microwave absorption distribution. In our case, the diameter of the sphere of detection is much larger than the ultrasonic wavelength. Next, an approximate algorithm is deduced, which is a modified backprojection of a quantity related with the thermoacoustic pressure. This approximate algorithm can be carried out in the time domain and is much faster than the exact solution. We have also tested a set of tissue samples. These experiments demonstrate that the images calculated by the modified backprojection method agree with the original samples very well. Moreover, the images have both the high contrast associated

5

with pure-microwave imaging and the 0.5-millimeter spatial resolution associated with pure-ultrasound imaging.

Results and discussion of thermoacoustic tomography

Spatial resolution

We quantified the line-spread function (LSF) of the imaging system. A metal wire with a diameter of 0.2 mm was buried in pork fat and then imaged by our imaging system with a scan radius of 75 mm. The thermoacoustic image of the embedded wire is shown in **Fig. 1**(a). Fig. 1(b) shows the profile of the LSF across the wire, where the ringing is caused primarily by the limited bandwidth of the detected signals. The full width at half maximum (FWHM) of the LSF is 0.5 mm. In analogy to the Rayleigh criterion, an alternative definition of spatial resolution is the horizonal displacement between the maximum and the first minimum of the LSF, which is 0.55 mm [Fig. 1(b)]. The superposition of two LSFs that are 0.55 mm apart is shown in Fig. 7(c), in which two represented wires can be clearly distinguished. Because the wire has a 0.2-mm diameter, the actual resolution is as fine as 0.35 mm, which agrees with the theoretical limit for 2-MHz thermoacoustic signals whose half wavelength is 0.38 mm in soft biological tissues.
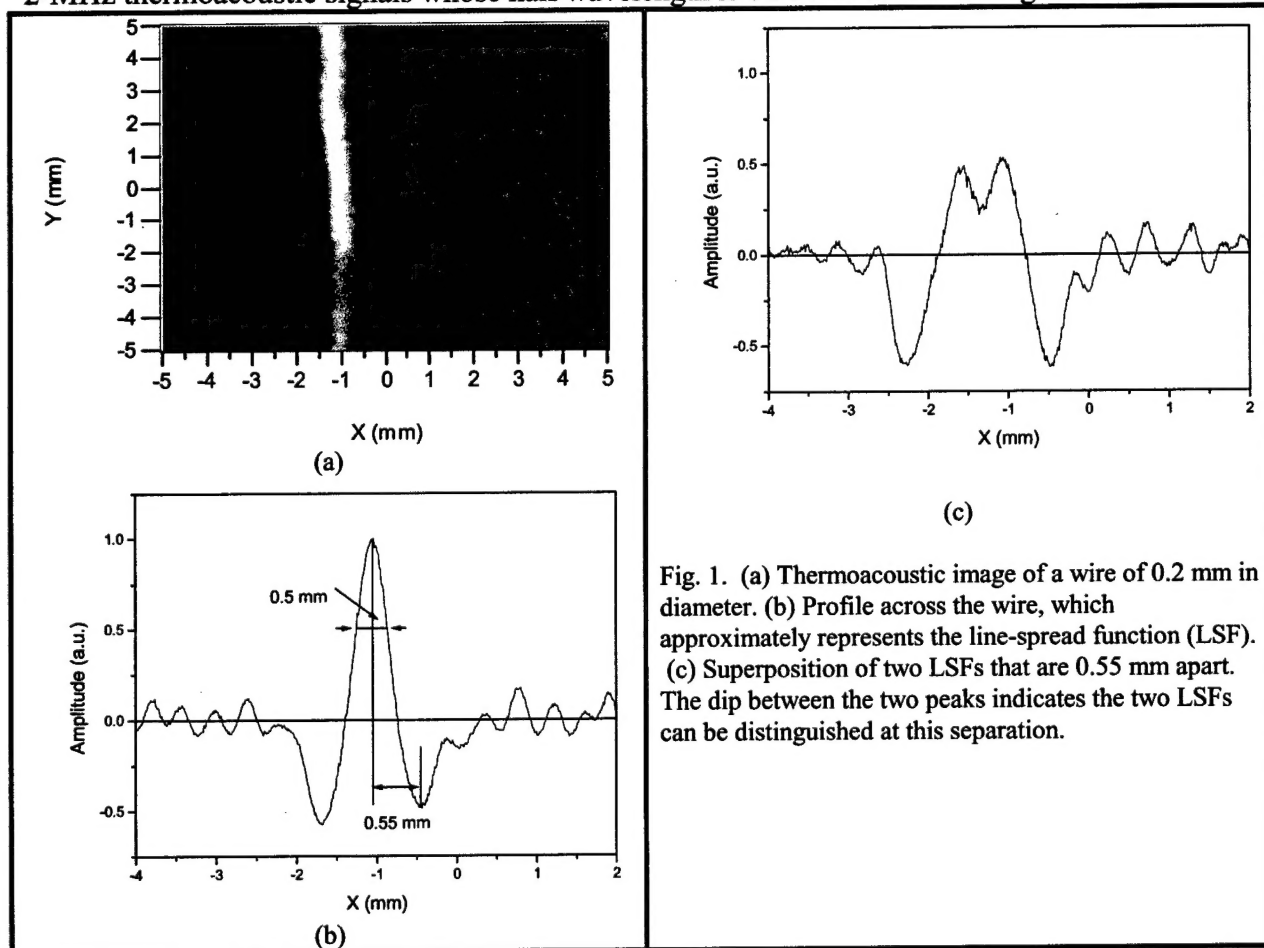

Fig. 1. (a) Thermoacoustic image of a wire of 0.2 mm in diameter. (b) Profile across the wire, which approximately represents the line-spread function (LSF). (c) Superposition of two LSFs that are 0.55 mm apart. The dip between the two peaks indicates the two LSFs can be distinguished at this separation.

Of course, the detecting transducer has a finite physical size. If it is close to the thermoacoustic sources, it cannot be approximated as a point detector. Its size will blur the

6

images and decrease the spatial resolution. Therefore, in experiments, the transducer must be placed some distance away from the tissue samples. In general, due to the finite size of the transducer, the farther away the transducer is from the detection center, the better the resolution at the expense of the signal.

Other factors limiting spatial resolution are the duration of the microwave pulse and the impulse response of the transducer. In general, using a shorter microwave pulse will produce more high-frequency components in the thermoacoustic signals. Selection of the duration of the pulse is dependent on the experimental conditions and measurement systems.

Imaging of excised breast (mastectomy) tissues

Several excised breast (mastectomy) specimens were imaged at the University of Texas M.D. Anderson Cancer Center using our thermoacoustic imaging system. A mammogram obtained before the mastectomy surgery of the breast is shown in **Fig. 2**(a). After the surgery performed by Dr. Hunt, the excised specimen was placed in a plastic cylindrical container with a diameter of 10 cm; and it was then imaged by three imaging modalities. The nipple of the specimen faced the bottom of the container to simulate the proposed *in vivo* configuration. The thickness of the specimen in the container was ~6 cm. The container had minimal effect on the transmission of RF, ultrasound, and x-ray. Another radiograph of the specimen was taken from the top of the cylindrical container [Fig. 2(b)]. The contrast of the lesion in Fig. 10(b) was lower than that shown in Fig. 10(a) because the specimen was quite thick in the container. A conventional B-mode gray-scale sonogram of the specimen [Fig. 2(c)] was taken by Dr. Fornage using a real-time scanner (HDI 5000, Philips-ATL, Bothell, WA) equipped with a 5–12 MHz broadband linear array electronic transducer. The lesion was located ~2 cm above the bottom of the container. The specimen was also imaged in the slice 2 cm above the bottom of the container using our thermoacoustic imaging system [Fig. 2(d)]. A circular scan was carried out by a cylindrically focused ultrasound detector (2.25 MHz center frequency and 0.9 mm diameter) with a step size of 2-1/4 degrees. The scan radius was 7.5 cm. The reconstructed image was computed by the backprojection method. The tumor was marked by a red circle. After these imaging experiments, the specimen was rendered to the Department of Pathology for histopathological diagnosis. This lesion was diagnosed as invasive lobular carcinoma with a size of ~1.5 cm.

The yellow rectangle in Fig. 2(d) marks the wave-guide aperture. The wave-guide for this experiment was not large enough to cover the entire specimen. Since then, we have upgraded our system with a larger wave-guide to overcome this problem. More experiments on mastectomy specimens using the improved imaging system have yet to be done.
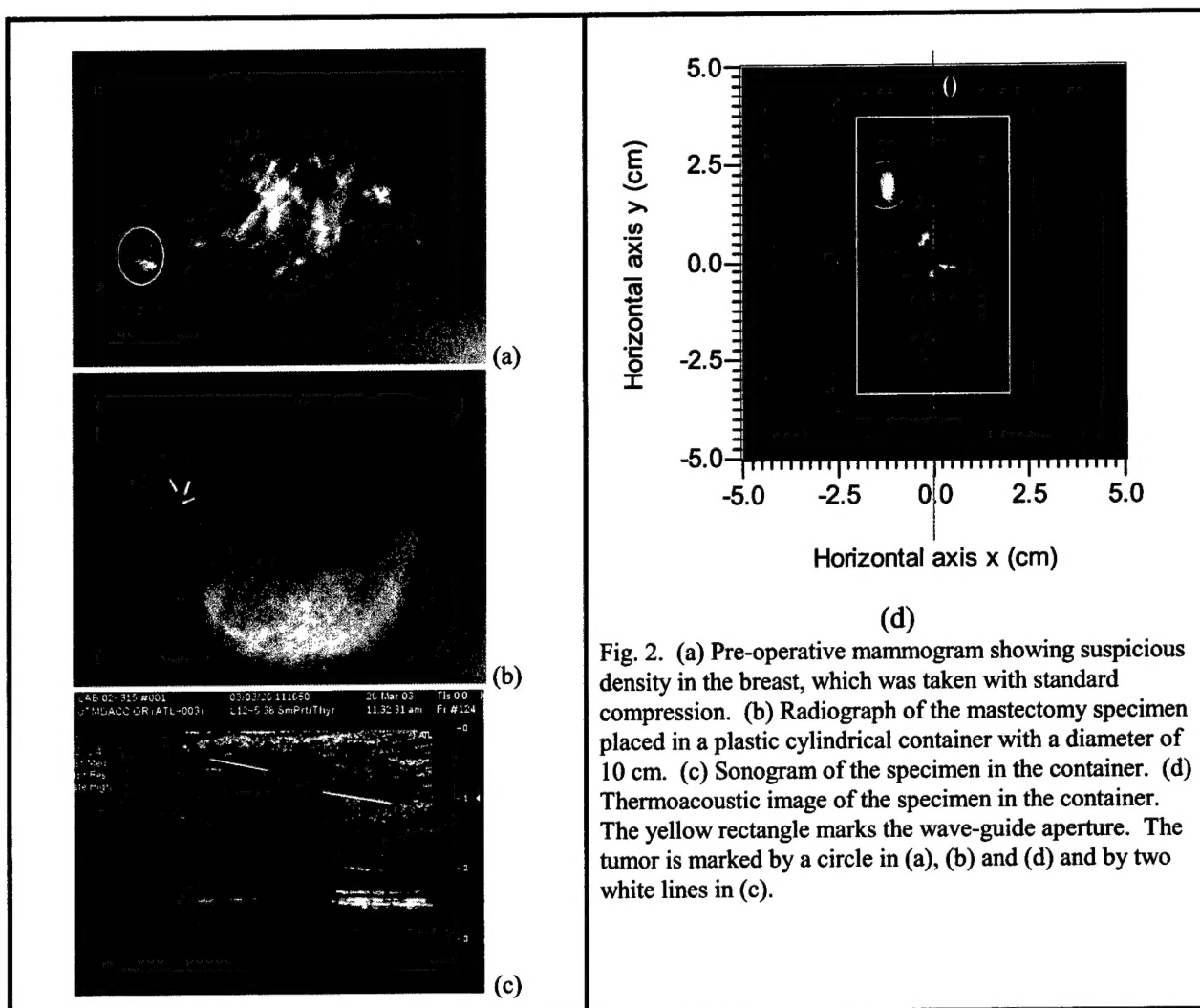
Fig. 2. (a) Pre-operative mammogram showing suspicious density in the breast, which was taken with standard compression. (b) Radiograph of the mastectomy specimen placed in a plastic cylindrical container with a diameter of 10 cm. (c) Sonogram of the specimen in the container. (d) Thermoacoustic image of the specimen in the container. The yellow rectangle marks the wave-guide aperture. The tumor is marked by a circle in (a), (b) and (d) and by two white lines in (c).

Statement of Work

Task 1: Setting up the scanning microwave-induced-acoustic tomography (SMIAT) instrument, Months 1–12:

  a. Modify/connect the microwave generator and the ultrasonic scanner.
  b. Image biological tissues in vitro with SMIAT.

Task 2. Extensive evaluation and optimization of the SMIAT setup, Months 13-36:

  a. Simulate microwave-induced-acoustic signals to provide guidance on the experiments.
  b. Optimize the ultrasonic and microwave parameters for good resolution and signal-to-noise ratio.
  c. Quantify the maximum imaging depth with SMIAT.
  d. Image biological tissues in vitro with SMIAT and quantify the imaging resolution.
  e. Image biological tissues in vitro with SMIAT and ultrasonography and quantify the contrast improvement of SMIAT over ultrasonography.

f. Co-register the SMIAT images with the conventional ultrasonograms.

Both tasks have been successfully accomplished. We went beyond the original planned task by imaging mastectomy specimens at M.D. Anderson Cancer Center.

Key Research Accomplishments

We have accomplished the following during the past year:

- Further progress in the reconstruction algorithms (MP Aug. 2002 and IEEE-TBE 2003).
- Better understanding of the mechanism of spatial resolution (PR 2003).
- Better understanding of the effect of heterogeneity on the images (IEEE-UFFC 2003).
- Extension of the technology to other electromagnetic sources (MP Dec. 2002).
- Imaging of mastectomy specimens at M.D. Anderson Cancer Center in Houston (unpublished yet).

Reportable Outcomes

Peer-reviewed journal articles

1. M. Xu and L.-H. Wang, "Pulsed-microwave-induced thermoacoustic tomography: Filtered backprojection in a circular measurement configuration," Medical Physics 29 (8), 1661–1669 (August 2002).

2. X. Wang, Y. Xu, M. Xu, S. Yokoo, E. S. Fry, and L.-H. Wang "Photoacoustic tomography of biological tissues with high cross-section resolution: Reconstruction and experiment," Medical Physics 29 (12), 2799–2805 (December 2002).

3. M. Xu and L.-H. Wang, "Analytic explanation of spatial resolution related to bandwidth and detector aperture size in thermoacoustic or photoacoustic reconstruction," Physical Review E 67 (5), 056605, 1–15 (May 2003).

4. M. Xu, Y. Xu, and L.-H. Wang, "Time-domain reconstruction algorithms and numerical simulations for thermoacoustic tomography in various geometries," IEEE Transactions on Biomedical Engineering 50 (9): 1086–1099 (September 2003).

5. Y. Xu and L.-H. Wang, "Effects of acoustic heterogeneity on thermoacoustic tomography in the breast," IEEE Transactions on Ultrasonics Ferroelectrics and Frequency Control 50 (9), 1134–1146 (September 2003).

Invited talks given by the PI

1. Clinical Center, NIH, Bethesda, Maryland.

2. Dept. of Biological Engineering, Univ. of Missouri, Columbia, Missouri.

3. Dept. of Radiology, Univ. Chicago, Chicago, IL.

4. Dept. of Bioengineering, Univ. of Illinois at Chicago, Chicago, IL.

5. Annual Ultrasonic Transducer Conference, Univ. of Southern California, Los Angeles, CA.

6. 3rd Int'l Conf. on Photonics and Imaging in Biology and Medicine, Wuhan, China. Plenary.

7. 6th Int'l Conf. on Correlation Optics, Chernivtsi, Ukraine. Plenary.

8. Int'l Conf. on Adv. Laser Tech., Cranfield, UK. Plenary keynote. Expenses covered by host.

9. School of Electrical and Electronic Engineering, University of Nottingham, UK.

10. Institute of Cancer Research and Royal Marsden NHS Trust, Surrey, UK.

11. Saratov Fall Meeting on Optical Technologies in Biophysics & Medicine, Russia. Plenary.

12. Frontiers in Optics, OSA Annual Meeting, Tucson, Arizona.

Degrees
- Y. Xu, Biomedical Eng., Texas A&M University.
- S. Jiao, Biomedical Eng., Texas A&M University.

Note: Both have defended successfully and the degrees will be conferred in Dec. 2003.

Conclusions

Since the previous report in 2002, we have published five peer-reviewed journal articles and delivered 12 invited talks. For the invited plenary talk given at UK, all travel related expenses were covered by the conference host.

The combination of ultrasound and microwave has provided us a unique opportunity for early-cancer imaging with high resolution and high contrast. A good imaging modality should have both high contrast and high spatial resolution. Our imaging technology combines synergistically radiofrequency waves and ultrasonic waves, where the former provides high contrast and the latter provides high spatial resolution. Only non-ionizing radiation is used. No painful breast compression is required. In addition, our images are free of speckle artifacts, which are prevalent in conventional ultrasound images. Our ultimate goal is to detect early breast cancer. Specifically, we have made further progress in the reconstruction algorithms (MP Aug. 2002 and IEEE-TBE 2003), in the mechanism of spatial resolution (PR 2003), in the understanding of heterogeneity (IEEE-UFFC 2003), and in extending the technology to other

electromagnetic sources (MP Dec. 2002). We went beyond the original planned task by imaging mastectomy specimens at M.D. Anderson Cancer Center.

Appendices (58 pages)

1.   **[9 pages]** M. Xu and L.-H. Wang, "Pulsed-microwave-induced thermoacoustic tomography: Filtered backprojection in a circular measurement configuration," Medical Physics 29 (8), 1661–1669 (August 2002).

2.   **[7 pages]** X. Wang, Y. Xu, M. Xu, S. Yokoo, E. S. Fry, and L.-H. Wang "Photoacoustic tomography of biological tissues with high cross-section resolution: Reconstruction and experiment," Medical Physics 29 (12), 2799–2805 (December 2002).

3.   **[15 pages]** M. Xu and L.-H. Wang, "Analytic explanation of spatial resolution related to bandwidth and detector aperture size in thermoacoustic or photoacoustic reconstruction," Physical Review E 67 (5), 056605, 1–15 (May 2003).

4.   **[14 pages]** M. Xu, Y. Xu, and L.-H. Wang, "Time-domain reconstruction algorithms and numerical simulations for thermoacoustic tomography in various geometries," IEEE Transactions on Biomedical Engineering 50 (9): 1086–1099 (September 2003).

5.   **[13 pages]** Y. Xu and L.-H. Wang, "Effects of acoustic heterogeneity on thermoacoustic tomography in the breast," IEEE Transactions on Ultrasonics Ferroelectrics and Frequency Control 50 (9), 1134–1146 (September 2003).

Pulsed-microwave-induced thermoacoustic tomography: Filtered backprojection in a circular measurement configuration

Minghua Xu and Lihong V. Wang[a]
Optical Imaging Laboratory, Biomedical Engineering Program, Texas A&M University,
3120 TAMU, College Station, Texas 77843-3120

Our study on pulsed-microwave-induced thermoacoustic tomography in biological tissues is presented. A filtered backprojection algorithm based on rigorous theory is used to reconstruct the cross-sectional image from a thermoacoustic measurement in a circular configuration that encloses the sample under study. Specific details describing the measurement of thermoacoustic waves and the implementation of the reconstruction algorithm are discussed. A two-dimensional (2D) phantom sample with 2 mm features can be imaged faithfully. Through numerical simulation, the full width half-maximum (FWHM) of the point-spread function (PSF) is calculated to estimate the spatial resolution. The results demonstrate that the circular measurement configuration combined with the filtered backprojection method is a promising technique for detecting small tumors buried in biological tissues by utilizing microwave absorption contrast and ultrasound spatial resolution ($\sim$mm). © *2002 American Association of Physicists in Medicine.* [DOI: 10.1118/1.1493778]

I. INTRODUCTION

Pulsed microwave-induced thermoacoustic tomography combines the advantages of both ultrasound spatial resolution and microwave absorption contrast.[1–4] The basic idea of this technique is that a very short microwave pulse (<1 μs) heats a sample; the sample then absorbs the microwave energy and simultaneously generates temporal thermoacoustic waves, which are strongly related to the locally absorbed microwave energy. The microwave pulse is so short that the heat diffusion's effect on the thermoacoustic wave can be ignored. The thermoacoustic signals have a wide frequency range up to MHz and carry the information of the microwave absorption distribution with millimeter spatial resolution. In practice, microwaves at 300 MHz–3 GHz with 0.1–1 μs pulse are often adopted, which offer penetration depths of several centimeters in biological tissues. For example, the penetration depths for fat and muscle tissues at 3 GHz microwaves are 9 and 1.2 cm, respectively.[3] Most other soft tissues have penetration depths in between those for muscle and fat tissues. The wide range of values among various tissues makes it possible to achieve high image contrast. In addition, the long penetration depth allows this technique to detect interior tumors.

In our initial studies, we used focused transducers with big apertures to detect thermoacoustic signals with both the linear scan[2,3] and the circular scan methods.[4] The big aperture gives us a good signal-to-noise ratio (SNR), because the SNR is inversely proportional to the square root of the aperture area. Each scan line is converted into a one-dimensional image along the axis of the transducer, and then cross-sectional images can be obtained by straightforward calculations. The axial resolution is obtained by measuring the temporal profiles of the thermoacoustic signals. However, the lateral resolution is mainly determined by the focal diameter of the transducer.[2,5] The image view is also limited by the focal length of the transducer.

An alternative method is to use unfocused transducers with small apertures to record the thermoacoustic signals and then reconstruct the microwave absorption distribution from the measured data. The different measurement configuration may, however, result in a different reconstruction algorithm. Under certain practical conditions, on a rigorous base, we theoretically reported a modified backprojection method for the planar, cylindrical, and spherical recording configurations.[6,7] These were computed through temporal spatial backprojection and coherent summation over spherical surfaces with spatial weighting factors. This method is something like synthetic aperture. Therefore, the SNR can be greatly improved through coherent summation, although the SNR of each detected temporal signal may be reduced due to the small aperture of the unfocused transducer as compared to focused transducers with big apertures.

In this paper, we present our study on pulsed-microwave-induced thermoacoustic tomography in biological tissues under a circular measurement configuration. A wide beam ($\sim$22 cm^2) of short-pulse (0.5 μs) microwave energy is used to illuminate a sample from the bottom. The sample absorbs the microwave energy and generates temporal thermoacoustic waves simultaneously. An unfocused ultrasonic transducer with a small aperture (6 mm) is used to record the thermoacoustic signals. A filtered backprojection (FBP) method based on rigorous theory is used to reconstruct the cross-sectional image from the measured data. Specific details describing the measurement of thermoacoustic waves and the implementation of the reconstruction algorithm are discussed. A phantom sample is investigated. The reconstructed image agrees with the original sample very well. Through
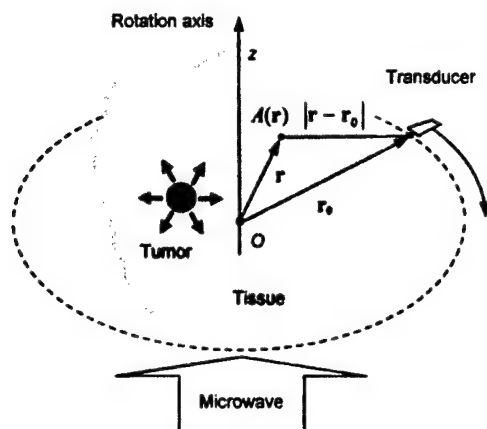
FIG. 1. Scheme of thermoacoustic circular measurement. Microwave pulses are transmitted to the sample from the bottom. The tumor inside absorbs the energy and generates thermoacoustic waves. An ultrasonic transducer at position r_0 records the thermoacoustic signals.

FIG. 2. Experimental setup.

numerical calculation of the point-spread function, the spatial resolution is estimated to reach ~mm.

II. METHOD OF MEASUREMENT

There are three typical measurement geometries: linear or planar configuration, circular or cylindrical configuration, and spherical configuration. The choice of measurement geometry depends on the practical need. For the purposes of investigating external organs, the second two choices are preferred. In practice, at least two restraints should be considered. One is that the space for delivering microwaves to the sample is physically limited. Ideally, the sample should be homogeneously illuminated as much as possible. Otherwise, the thermoacoustic signal will reflect not only the absorption differentiation, but also inhomogeneous illumination, which will result in reconstruction artifacts. The other restraint is that it is physically impossible to collect measurements over a 4π solid angular range. The developed reconstruction algorithm requires that the detectors receive outgoing thermoacoustic waves from all possible angular directions.[6,7] But, in reality, a limited angular range has to be tolerated, and the incomplete data also results in some reconstruction artifacts.

In this study, we chose a circular measurement configuration, as shown in Fig. 1. Tissue, such as breast tissue, is hard to compress but easy to deform. A slight force can make the external tissue nearly cylindrical in shape. Then, the microwave can be delivered to the tissue from its larger bottom and the detector can measure the outgoing thermoacoustic waves in a circular geometry around the tissue. The wavelength of microwaves below 3 GHz is relatively long, e.g., at 3 GHz, 10 cm in air, and 3 cm in soft tissue, compared to the typical size of tissue investigated in several centimeters diameter. That helps to illuminate the tissue homogeneously. However, because of attenuation, microwaves along the z axis decay exponentially and the generated thermoacoustic signal along the z axis decays exponentially, too, even in a
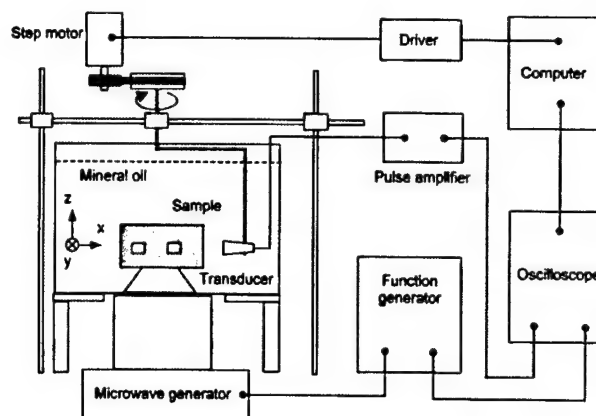
homogenous sample. But the circular detection plane, i.e., the horizontal xy plane, is parallel with the incident plane of microwave pulses. Besides, due to the bounded water and salt in cancer cells,[8,9] the tumor will absorb more microwave energy and generate more intense thermoacoustic waves than the surrounding tissue. Therefore, the thermoacoustic signals from the circular plane have a significantly reduced dynamic range compared with those in any other planes. This improves the accuracy of both data acquisition and data reconstruction tremendously. As shown below, reasonable reconstruction images are achieved in the experiment.

Figure 2 shows the experimental setup we used for the circular measurement configuration. A Plexiglas container is filled with mineral oil. An unfocused transducer is immersed inside it and fixed on a rotation device. A step motor drives the rotation device and then moves the transducer scan around the sample on a horizontal x-y plane, where the transducer horizontally points to the rotation center. A sample is immersed inside the container and placed on a holder: it is made of a thin plastic material, which is transparent to microwaves. The transducer (V323, Panametrics) has a central frequency of 2.25 MHz and a diameter of 6 mm.

The microwave pulses transmitted from a 3 GHz microwave generator have a pulse energy of 10 mJ and a pulse width of 0.5 μs. A function generator (Protek, B-180) is used to trigger the microwave generator, control its pulse repetition frequency, and synchronize the oscilloscope sampling. In our experiments, the pulse repetition frequency is 50 Hz and the oscilloscope sampling frequency is 20 MHz. Microwave energy is delivered to the sample by a rectangular waveguide with a cross section of 72 mm×34 mm. A personal computer is used to control the steps. The signal from the transducer is first amplified through a pulse amplifier, then recorded and averaged 500 times by an oscilloscope (TDS640A, Tektronix), and finally transferred to a personal computer for imaging.

This system is within the IEEE standard for safety levels with respect to human exposure to radio frequency electromagnetic fields (see the Appendix). The waveguide is filled with air and has a mode of $TE_{1,0}$. The wavelength of the

emitted microwave is 10 cm in air. The microwave irradiates from the waveguide and then propagates through a thin layer of air into the container and the tissue sample. Due to the relatively long wavelength of microwave in tissue (~3 cm at 3 GHz), the diffraction causes only smooth variations on a scale comparable to 3 cm. As discussed later, in signal processing, we removed the low-frequency component below 50 KHz, which corresponds to an acoustic wavelength of ~3 cm. Therefore, the effect of mode structure of microwave irradiation on thermoacoustic imaging is minor.

III. METHOD OF RECONSTRUCTION

We assume a tissue with inhomogeneous microwave absorption but a relatively homogeneous acoustic property. When the microwave pulse duration is <1 μs, the heat diffusion's effect on the thermoacoustic wave in the tissue can be ignored. The speed of sound in most soft tissue is relatively constant at ~1.5 mm/μs. Therefore, the pressure $p(\mathbf{r},t)$ produced by the heat source $H(\mathbf{r},t)$ obeys the following equation:[10]

$$c^2 \nabla^2 p(\mathbf{r},t) - \frac{\partial^2}{\partial t^2} p(\mathbf{r},t) = -\Gamma(\mathbf{r}) \frac{\partial H(\mathbf{r},t)}{\partial t}, \quad (1)$$

where the Grüneisen parameter $\Gamma(\mathbf{r}) = \beta c^2/C_p$, c is the speed of sound; β is the isobaric volume expansion coefficient; C_p is the heat capacity; and $H(\mathbf{r},t)$ is the heating function defined as the thermal energy per unit time and unit volume deposited by the energy source. Basically, the heating function can be written as the product of a spatial absorption function and a temporal illumination function:

$$H(\mathbf{r},t) = A(\mathbf{r})I(t). \quad (2)$$

Suppose a delta illuminating function $\delta(t)$, the detected acoustic pressure $p(\mathbf{r}_0,t)$ on the circular surface $\mathbf{r} = \mathbf{r}_0 = (\rho_0, \varphi_0, z_0)$, and time t can be written as[6]

$$p(\mathbf{r}_0,t) = \frac{1}{c} \frac{\partial}{\partial t} \int \int \int d^3 r \, D(\mathbf{r}) \frac{\delta(ct - |\mathbf{r}_0 - \mathbf{r}|)}{4\pi |\mathbf{r}_0 - \mathbf{r}|}, \quad (3)$$

where $D(\mathbf{r}) = A(\mathbf{r})\Gamma(\mathbf{r})$. The inverse problem is to reconstruct the spatial distribution $D(\mathbf{r})$ from a set of data $p(\mathbf{r}_0,t)$ measured at a different position $\mathbf{r}_0$.

Due to the finite bandwidths of the transducer, the preamplifier and the microwave pulse, only a portion of the information about the absorption structure can be restored. The high-frequency component of the thermoacoustic signal primarily reflects the small size structure while the low-frequency component primarily reflects the large size structure. If challenged to detect small size tumors, we can safely remove the low-frequency component. Besides, the wavelengths of the high-frequency thermoacoustic waves are much smaller than the detecting distance between the thermoacoustic source and the transducer. Under the above conditions, i.e., $\rho_0 k \gg 1$ or $k|\mathbf{r} - \mathbf{r}_0| \gg 1$, where k is the wave number, we have shown theoretically that the distribution $D(\mathbf{r})$ can be calculated by the following 2D surface integral in the cylindrical configuration:[7]

$$D(\rho,\varphi,z) = -\frac{1}{2\pi c^2} \int \int_{S_0} dS_0 [\mathbf{n} \cdot \mathbf{n}_0] \frac{1}{t} \frac{\partial p(\mathbf{r}_0,t)}{\partial t} \bigg|_{t = |\mathbf{r} - \mathbf{r}_0|/c}, \quad (4)$$

where

$$\mathbf{n} \cdot \mathbf{n}_0 = \frac{|\boldsymbol{\rho} - \boldsymbol{\rho}_0|}{|\mathbf{r} - \mathbf{r}_0|} = \sqrt{\frac{\rho^2 + \rho_0^2 - 2\rho\rho_0 \cos(\varphi_0 - \varphi)}{|\mathbf{r} - \mathbf{r}_0|^2}}$$

$$= \sqrt{1 - \frac{(z_0 - z)^2}{|\mathbf{r} - \mathbf{r}_0|^2}}, \quad (5)$$

$dS_0 = \rho_0 d\varphi_0 \, dz_0$, $\boldsymbol{\rho}$ and $\boldsymbol{\rho}_0$ are the projections of $\mathbf{r}$ and $\mathbf{r}_0$ on the z plane, respectively, and $\mathbf{n}$ and $\mathbf{n}_0$ are unit vectors pointing along the line joining $\boldsymbol{\rho}$ and $\boldsymbol{\rho}_0$ and along the line joining $\mathbf{r}$ and $\mathbf{r}_0$, respectively. This is a modified backprojection formula of quantity $-(1/t)[\partial p(\mathbf{r}_0,t)/\partial t]$. The weighting factor $[\mathbf{n} \cdot \mathbf{n}_0]$ is less than 1, except if $z = z_0$, $[\mathbf{n} \cdot \mathbf{n}_0] = 1$. That indicates that the cross-sectional image of any z_0 plane is mainly determined by the data measured on the circle of the same z_0 plane. In other words, if some small absorption sources are located on a z_0 plane, a set of circular measurement data on the same plane would be sufficient to yield a good cross-sectional image.

The quantity $\partial p(\mathbf{r}_0,t)/\partial t$ can be calculated through the Fourier transform,

$$\frac{\partial p(\mathbf{r}_0,t)}{\partial t} = \text{FFT}^{-1}\{-i\omega p(\mathbf{r}_0,\omega)W_\Omega(\omega)\}, \quad (6)$$

where FFT^{-1} denotes the fast inverse Fourier transform; ω is angular frequency and equal to $2\pi f$; $W_\Omega(\omega)$ is a window function; and the Fourier transform defines

$$\bullet(\omega) = \int_{-\infty}^{+\infty} \bullet(t)\exp(i\omega t)dt. \quad (7)$$

We want to point out that the factor ω in Eq. (6) actually represents a pure ramp filter, which will significantly depress the low-frequency signal. That is helpful to guarantee the validity of the reconstruction, Eq. (4). The ramp filter can also amplify the high-frequency noise in such a way that the reconstructed image is not acceptable from the physical point of view. In order to avoid this effect, it is necessary to introduce a relative low-pass filter $W_\Omega(\omega)$ characterized by a cutoff angular frequency $\Omega = 2\pi f_\Omega$. A Hanning window is our choice in this case:

$$W_\Omega(\omega) = \begin{cases} 0.5 + 0.5 \cos\left(\pi \frac{\omega}{\Omega}\right), & \text{if } |\omega| < \Omega, \\ 0, & \text{otherwise.} \end{cases} \quad (8)$$

Thus, the reconstruction algorithm can also be termed a filtered backprojection (FBP) with the modified ramp filter $\omega W_\Omega(\omega)$. Unlike the FBP algorithm used in x-ray tomography,[11] which uses surface integration over intersecting planes, the method in our problem is calculated through temporal backprojection and coherent summation over spherical surfaces with a certain spatial weighting factor.

IV. EXPERIMENT

The experimental conditions necessitate special care. The reconstruction theory requires point detectors, and the real transducer must never be a point. But, we can ignore its size if we put it at a distance from the sample that is greater than the size of the transducer aperture. In addition, we must shield both the transducer and the electrical transmission cables from microwave illumination. Otherwise, the microwave pumping will cause harmful electrical signals via electromagnetic induction. If well shielded, the induced signal decays very rapidly. A time gate can cut out the induced signal before the arrival of the thermoacoustic signal. Suppose $p(\mathbf{r}_0,t)$ is the thermoacoustic signal with delta-pulse microwave pumping, then the measured thermoacoustic signal can be written as a convolution with the measurement system response $H(t)$:

$$S(\mathbf{r}_0,t)=p(\mathbf{r}_0,t)*H(t). \tag{9}$$

Considering the temporal response $M(t)$ of the amplifier, the impulse response $R(t)$ of the transducer and the temporal profile $I(t)$ of the microwave pulse, $H(t)$ can also be written as a convolution,

$$H(t)=M(t)*I(t)*R(t). \tag{10}$$

In the frequency domain, Eq. (9) can be written as

$$S(\mathbf{r}_0,\omega)=p(\mathbf{r}_0,\omega)H(\omega). \tag{11}$$

Basically, we cannot recover all of the available information because of the limited bandwidth of the detection system. The information we can acquire depends on the system response $H(\omega)$. In practice, $M(\omega)$ is very wide and ~ 1; $I(\omega)$ determines the bandwidth of the generated thermoacoustic signal, which is approximately inversely proportional to the width of its temporal profile; $R(\omega)$ is a wide-band transducer with a central frequency ω_c. If $H(\omega)$ is known, an appropriate deconvolution algorithm can be used to figure out $p(\mathbf{r}_0,\omega)$.

In our experiments, the illumination $I(t)$ is approximately a rectangular function with duration $\tau=0.5~\mu s$, and its temporal profile is shown as the short dashed line in Fig. 3(a), which determines the frequency of the generated thermoacoustic signal below 2 MHz. The transducer that we used is of the videoscan type with a central frequency of $f_c = 2.25$ MHz, and its temporal profile is shown as the solid line in Fig. 3(a). In the frequency range below 2 MHz, the response of the transducer approximates a ramp filter. As shown in Fig. 3(b), the calculated $H(f)$ (solid line) was compared with a pure ramp filter f (short dashed line). In this special case for our measurement system, the filtered $\partial p(\mathbf{r}_0,t)/\partial t$ can be approximately calculated by an inverse Fourier transformation as

$$\frac{\partial p(\mathbf{r}_0,t)}{\partial t}\approx \text{FFT}^{-1}\{S(\mathbf{r}_0,\omega)W_\Omega(\omega)\}. \tag{12}$$

Next, we imaged a phantom sample with a complex absorption structure using the following procedure. First, we used screwdrivers to carve a structure: the word "OIL" (ab-
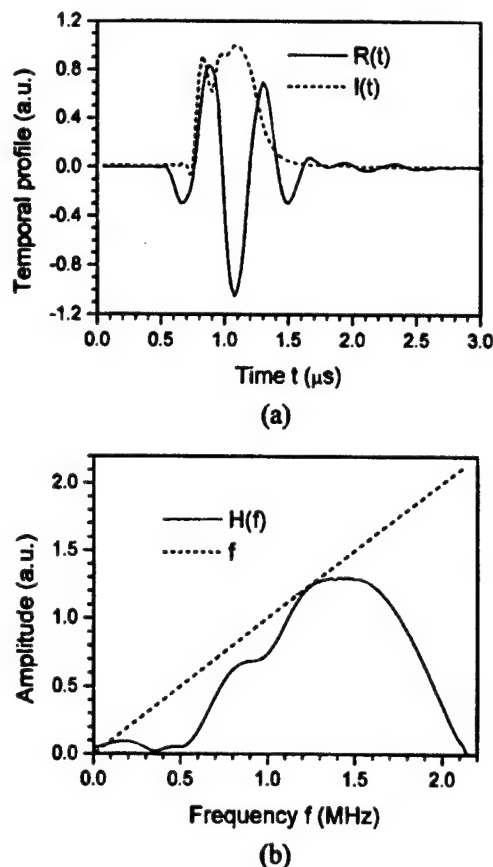

FIG. 3. (a) The impulse response of the transducer $R(t)$ and the temporal profile of the microwave pulse $I(t)$; (b) the system response $H(f)$ and the pure ramp filter f.

breviation for Optical Imaging Lab) in a large fat base. The diameter of the dent was about 2 mm. In the meantime, we prepared a hot solution with 5% gelatin, 1% salt, and a drop of dark ink to improve the photographic properties. Then we used an injector to inject several drops of the hot solution into the dents and subsequently blew out the air to assure good coupling between the gelatin solution and the fat tissue. The gelatin word was cooled at room temperature until solidified. The photograph of the sample at this stage is shown in Fig. 4(a). Finally, we added a piece of fat both on the top and on the bottom of the sample so that the gelatin word was buried inside the fat tissue. The diagram of the structure in side view is shown in Fig. 4(b).

The transducer rotationally scanned the sample from 0°–360° with step size 2.25° in the plane, including the word "OIL." The distance between the transducer and the rotation center was 8 cm. The sampling frequency of the oscilloscope was 20 MHz. We chose the cutoff frequency $f_\Omega = 4$ MHz in the filter W_Ω. The filtered temporal thermoacoustic signals are shown in Fig. 4(c). Because of some time delay in the oscilloscope, the rotation origin is at time $t=36.8~\mu s$. Unlike X-ray tomography,[11] these data have no symmetric property in a 2π period. The reconstructed image produced by our filtered backprojection method, which agrees with the original sample very well, is shown in Fig. 4(d). However, when
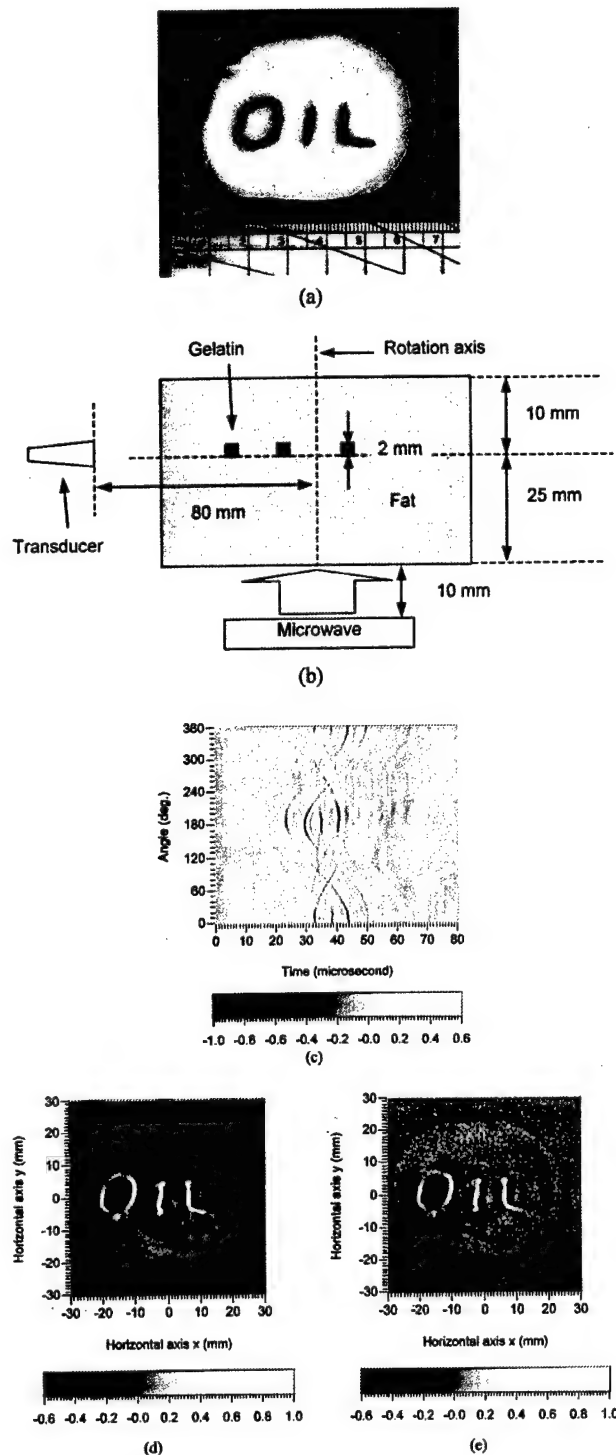
(a)

(b)

(c)

(d)

(e)

FIG. 4. (a) Cross-sectional photograph of the sample; (b) the diagram of the measurement in side view; (c) the filtered thermoacoustic temporal signals detected at different angular positions from 0°–360°; (d) the reconstructed image with filtering; (e) the reconstructed image without filtering.

the filter W_Ω was not used to depress the high-frequency noise, the reconstructed image displayed certain randomly distributed spots, as shown in Fig. 4(e), which degrade the image quality a lot.

In signal processing, we removed only the low-frequency component below 50 KHz. As shown in Fig. 4(d), the boundary and location of the large fat base with a 5 cm diameter was also faithfully imaged. Therefore, we conclude that the removal of low frequencies in signal processing will not have much effect on the detection of relatively large structures. The location and boundary of the microwave absorption structures are primarily determined by the relatively high-frequency component of the thermoacoustic signals.

V. NUMERICAL SIMULATION

The full width half-maximum (FWHM) of the point-spread-function (PSF) profile can be used to represent the spatial resolution.[12] Through numerical simulation, we can calculate the PSF profiles and then estimate the spatial resolution.

The limit band of the detection system is a primary factor in limiting the spatial resolution. Consider a point source at axis $x = x_p$, which can be written in the circular polar coordinates as

$$D(\mathbf{r}_p) = \frac{\delta(\rho - x_p)\delta(\varphi)\delta(z)}{\rho}. \tag{13}$$

Substituting it into Eq. (3), and taking the Fourier transform, it is easy to obtain the generated thermoacoustic wave in the frequency domain,

$$p(\mathbf{r}_0, \omega) = \frac{-i\omega}{4\pi c^2} \frac{\exp(ikd)}{d}, \tag{14}$$

where d is the distance between the point source and the detector,

$$d = \sqrt{\rho_0^2 + x_p^2 - 2\rho_0 x_p \cos\varphi_0 + z_0^2}. \tag{15}$$

For simplicity, we only consider a circular measurement in the plane $z_0 = 0$. We assume the sampling frequency is 20 MHz and use the Hanning window to simulate the limit band of the detection system. Figure 5(a) shows three examples of ramp filters modified by Hanning windows with cutoff frequencies at 4, 2, and 1 MHz, respectively. We use Eq. (6) to calculate derivatives of the temporal thermoacoustic signals. Finally, the FBP, Eq. (4), is employed to reconstruct images from the simulated data.

The numerical calculations demonstrate that the PSF is radially symmetric only when the point source is located at the origin. Such examples of PSF radial profiles with different cutoff frequencies are shown in Fig. 5(b). When a point source is off center, the PSF is not radially symmetric. Figure 5(c) shows some examples of PSF radial profiles when the point source is at $x_p = 30$ mm. The farther the point is off the origin, the more distortion the PSF has. But the distortion is not significant and the PSF does not expand in either the lateral or axial direction by very much. Therefore, the PSF and FWHM can be regarded as nearly space invariant. Of course, if the detector system has a lower cutoff frequency, the width of the PSF profile has more extension and the spatial resolution becomes lower. Only a wide band signal at
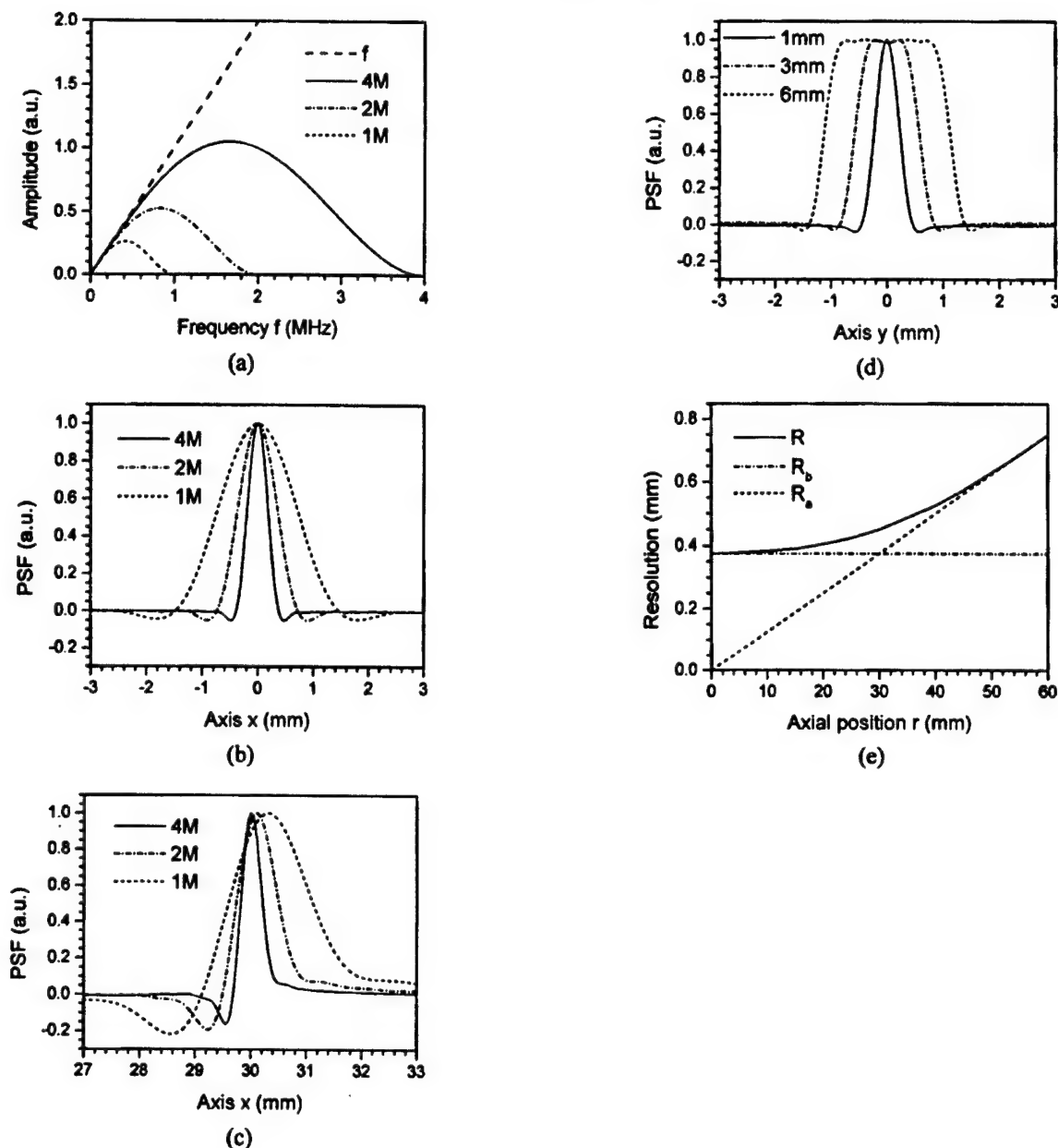
FIG. 5. (a) The pure ramp filter f (dashed line) and the modified filters by Hanning windows with different cutoff frequencies: 4 MHz (solid line), 2 MHz (short dash dotted line) and 1 MHz (short dashed line); Examples of PSF radial profiles with Hanning windows at cutoff frequencies: 4 MHz (solid line), 2 MHz (short dash dotted line) and 1 MHz (short dashed line), when the point source at (b) the origin and (c) the axis $x=30$ mm; (d) examples of PSF profiles in lateral view with different detector aperture size $\delta=1$ mm (solid line), 3 mm (short dash dotted line), and 6 mm (short dashed line), respectively; (e) an example of a comparison with R_a, R_b, and R, where $\delta=1$ mm.

a sufficiently high frequency can restore good spatial resolution and accurate position orientation. Actually, the distortion of the PSF results from the approximation of the FBP algorithm.

For the PSF profiles in Fig. 5(b), the FWHM were measured to be 0.4, 0.9, and 1.5 mm for the cutoff frequencies 4, 2, and 1 MHz, respectively. These values are equivalent to the corresponding half-wavelengths of the central or dominative frequencies of the modified ramp filters: 1.7, 0.8, and 0.4 MHz, respectively. Therefore, the spatial resolution re-

sulting from the bandwidth of the detection system can be estimated by

$$R_b \approx \frac{\lambda_c}{2}, \tag{16}$$

where λ_c is the wavelength of the central or dominative high frequency of the detection system.

In addition to the limitations resulting from the bandwidth of the detection system, the size of the detector aperture is
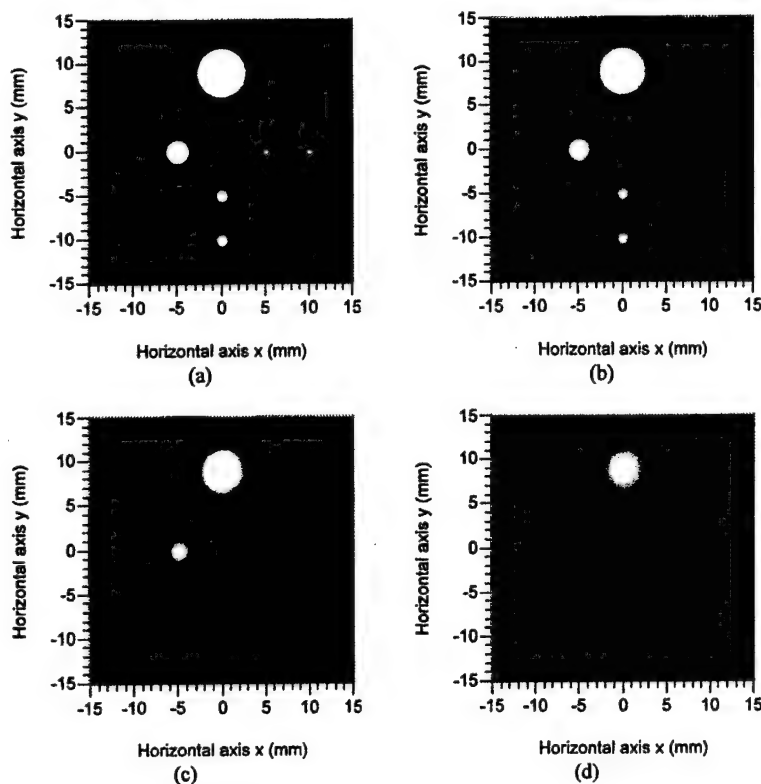
FIG. 6. Examples of reconstructed images with Hanning windows at different cutoff frequencies: (a) 4 MHz, (b) 2 MHz, (c) 1 MHz, and (d) 0.5 MHz respectively.

another factor, which limits spatial resolution. We also chose to investigate its effect through numerical simulation. The received signal in the detector can be simulated by a surface integral divided by its aperture. Then the PSF can be calculated through the FBP, Eq. (4). We assume that the detector has a flat surface with diameter δ.

The simulation demonstrates that the PSF gradually extends along the lateral side but changes very little along the axial direction. Figure 5(d) shows examples of lateral profiles for $\delta=1$, 3, and 6 mm, respectively, where the point source at $x_p=30$ mm and $f_\Omega=4$ MHz. It is expected that a big detector aperture will greatly blur the lateral resolution. For convenience, this kind of spatial resolution can be termed R_a, which can be estimated by

$$R_a \approx \frac{r}{r_0} \delta, \qquad (17)$$

where r_0 is the radius of the measurement geometry and r is the distance of the point source and the origin. Figure 5(e) shows an example of a comparison with R_a, R_b, and the lateral resolution R, where $\delta=1$ mm; $r_0=80$ mm and $f_\Omega=4$ MHz. Near the origin, $R_a<R_b$, the lateral resolution R is still dominated by R_b. Beyond that where $R_a>R_b$, the lateral resolution R is greatly degraded by the aperture size δ and finally equals R_a. The result also indicates that either a large detector radius r_0 or a small detector aperture δ can improve the lateral resolution in the central region of the detection system. But R_b, i.e., the band limit of the detection system, determines the highest resolution we can obtain.

Let us review the experiment in the previous section. The detector aperture has a 6 mm diameter, and the image region is 30 mm in diameter. Therefore, the worst spatial resolution at $r=30$ mm still has ~ 2 mm. The dominative high frequency of the detection system is about 1.6 MHz, as shown in Fig. 3(b). Thus, the highest resolution is about 0.5 mm. That explains why the word "OIL" in 2 mm diameter can be clearly imaged.

Next, we conduct some numerical experiments. We consider a set of uniform spherical absorbers surrounded by a nonabsorbing background medium. For convenience, we use the centers of the absorbers to denote their positions. We also assume that the pulse duration is very short and can be regarded as a delta function, and, consequently, that the thermoacoustic signal received by the transducer can be calculated by Eq. (3). We employ the circular measurement configuration, as shown in Fig. 1(a). Suppose the circular ultrasonic array consists of 160 elements. The detection radius is 80 mm. There are six spherical absorbers in the $z=0$ plane: a pair of tiny absorbers in diameter 0.75 mm at the positive x axis, a pair of small absorbers in diameter 1.5 mm at the negative y axis, a moderate absorber in diameter 3 mm at the negative x axis, and a big absorber in diameter 6 mm at the positive y axis. Equation (6) is used to compute the filtered thermoacoustic signals with Hanning windows. Figure 6 shows the reconstructed images with different cutoff frequencies: (a) 4 MHz, (b) 2 MHz, (c) 1 MHz, and (d) 0.5 MHz, respectively. As expected, all of the absorbers are clearly imaged, as shown in Fig. 6(a), when the frequency

band is sufficiently wide. However, in the absence of a high-frequency signal, the small size structure is lost. For example, if the cutoff frequency is 1 MHz, the tiny absorbers disappear. For the even lower cutoff frequency of 0.5 MHz, not only do the small absorbers disappear, but also the originally sharp borders of the big absorbers are greatly degraded.

The above numerical simulations gives us clear directions for designing a good image system with ~mm spatial resolution. The duration of the microwave pulse should be less than 1 μs, which allows a thermoacoustic signal up to ~MHz frequency to be generated. The measurement detectors and the preamplifier should have sufficiently wide bands, and the central frequency of the detection system should reach 1–2 MHz. The transducer with a small aperture, such as 1 mm in diameter, is preferred. The small aperture will have less effect on the lateral resolution, and it will reduce the SNR as well. Alternatively, a big detection radius 10–15 cm can be adopted with the sacrifice of signal amplitude because of the acoustic wave propagation attenuation. A wide microwave frequency range from 300 MHz to 3 GHz can be used as the irradiation source. A lower-frequency microwave might be better to image relatively large size samples because it can penetrate deeper.

Finally, we must point out that incomplete measurement data will result in reconstruction artifacts and will degrade the spatial resolution. This topic will be addressed more completely in future work.

VI. CONCLUSION

We have presented our study on pulsed-microwave-induced thermoacoustic tomography in biological tissues by a circular measurement configuration. A filtered backprojection algorithm is used to reconstruct the cross-sectional images. The reconstructed image of a phantom sample agrees with the original values very well. Through numerical simulation, the point-spread function is calculated to estimate the spatial resolution. The results demonstrate that the circular measurement configuration combined with the filtered back-projection method is a promising technique for using microwave absorption contrast and ultrasound spatial resolution (~mm) to detect small tumors buried in biological tissues.

ACKNOWLEDGMENTS

APPENDIX

According to the IEEE standard for safety levels with respect to human exposure to radio frequency electromagnetic fields 3 KHz to 300 GHz (IEEE Std C95.1, 1999 edition), the peak power of maximum permissible exposure (Peak MPE) for a controlled environment in the frequency range f (300–3000 MHz) can be computed by

$$\text{Peak MPE} = \frac{0.24}{N} \times \frac{f}{\text{Pulse width}} \quad (\text{mW/cm}^2),$$

where N is the pulse number per second ($N > 5$) and the pulse width (< 100 ms) is in seconds. In other words, the permissible pulse energy with illumination area S (cm^2) can be estimated by

$$\text{Pulse Energy} = \text{Peak MPE} \times \text{Pulse width} \times S$$

$$= \frac{0.24 S f}{N} \quad (\text{mJ}).$$

In our system, $N = 50$, pulse width$= 0.5$ ms, and the area of the waveguide $S = 7.2 \times 3.4 \text{ cm}^2 \approx 22 \text{ cm}^2$. Therefore, the permissible pulse energy$= 0.24 \times 22 \times 3000/50 \approx 300$ mJ. But the pulse energy that we used is only 10 mJ, which is much less than the above permissible value.

Actually, the pulse width is so short that only tiny energy is delivered to the sample. The microwave is not focused and the illumination area is so big that the energy density in the tissue is very low. Suppose the penetration depth of microwave is 1 cm, the energy density E_a due to a pulse microwave excitation can be estimated by

$$E_a = \text{Pulse energy}/(\text{Illumination area } S \times 1 \text{ cm})$$

$$= 10 \text{ mJ}/22 \text{ cm}^3 \approx 0.45 \text{ mJ/cm}^3.$$

Then, we can estimate the pressure and temperature rise excited by a pulse microwave in tissue. The muscle contains about 75% water. We take it as an example. In muscle, the volume expansion coefficient is $\beta \approx 3.8 \times 10^{-4} \text{ K}^{-1}$, the heat capacity is $C_p \approx 3.7 \text{ mJ/(g mK)}$, and the mass density is $\rho \approx 1$ g/cm^3. Therefore, the Grüneisen parameter$= \beta c^2/C_p \approx 0.23$, and the generated pressure rise,

$$p = 0.23 \times 0.45 \text{ mJ/cm}^3 \approx 0.1 \text{ mJ/cm}^3 = 1 \text{ mbar},$$

and the temperature rise,

$$\delta T = E_a/(C_p \rho) = 0.45/3.7 \approx 0.1 \text{ mK}.$$

As discussed in the paper, the penetration depth in tissue for a microwave below 3 GHz is several centimeters. The Grüneisen parameter in other soft tissue should be close to the value 0.23 in muscle. Therefore, we can conclude that a microwave pulse only causes pressure rise with several millibars and temperature rise with millidegrees. Such tiny values are far beyond causing tissue damage.

[a]Author to whom all correspondence should be addressed. Telephone: 979-847-9040; fax: 979-845-4450; electronic mail: LWang@tamu.edu; URL: http://oilab.tamu.edu.

[1] R. A. Kruger, K. K. Kopecky, A. M. Aisen, D. R. Reinecke, G. A. Kruger, and W. L. Kiser, "Thermoacoustic CT with radio waves: A medical imaging paradigm," Radiology **211**, 275–278 (1999).

[2] G. Ku and L.-H. V. Wang, "Scanning thermoacoustic tomography in biological tissues," Med. Phys. **27**, 1195–1202 (2000).

[3] G. Ku and L.-H. V. Wang, "Scanning microwave-induced thermoacoustic tomography: Signal, resolution, and contrast," Med. Phys. **28**, 4–10 (2001).

[4] M.-H. Xu, G. Ku, and L.-H. V. Wang, "Microwave-induced thermoacoustic tomography using multi-sector scanning," Med. Phys. **28**, 1958–1963 (2001).

[5] R. A. Kruger and P. Liu, "Photoacoustic ultrasound: Pulse production and detection in 0.5% Liposyn," Med. Phys. **21**, 1179–1184 (1994).

[6] M.-H. Xu and L.-H. V. Wang, "Time-domain reconstruction for thermoacoustic tomography in a spherical geometry," IEEE Trans. Med. Imaging (in press). Update: 21, 814-822, (2002).

[7] M.-H. Xu, Y. Xu, and L.-H. V. Wang, "Thermoacoustic imaging in biological tissues: Time–domain reconstruction algorithms," IEEE Biomed. Eng. (submitted).

[8] S. Chaudhary, R. Mishra, A. Swarup, and J. Thomas, "Dielectric properties of normal human breast tissues at radiowave and microwave frequencies," Indian J. Biochem. Biophys. **21**, 76–79 (1984).

Ref. 7 Update: Accepted.
New title: Time-domain reconstruction algorithms and numerical simulations for thermoacoustic tomography in various geometries

[9] W. Joines, Y. Zhang, C. Li, and R. Jirtle, "The measured electrical properties of normal and malignant human tissues from 50–900 MHz," Med. Phys. **21**, 547–550 (1994).

[10] A. C. Tam, "Application of photoacoustic sensing techniques," Rev. Math. Phys. **58**, 381–431 (1986).

[11] M. Bertero and P. Boccacci, *Introduction to Inverse Problems in Imaging* (Institute of Physics Publishing, London, 1998).

[12] R. A. Kruger, W. L. Kiser, K. D. Miller, H. E. Reynolds, D. R. Reinecke, G. A. Kruger, and P. J. Hofacker, "Thermoacoustic CT: Imaging principles," Proc. SPIE **3916**, 150–159 (2000).

Effects of Acoustic Heterogeneity in Breast Thermoacoustic Tomography

Yuan Xu and Lihong V. Wang[*]
Optical Imaging Laboratory, Department of Biomedical Engineering
Texas A&M University, 3120 TAMU, College Station, Texas 77843-3120

[*] Author to whom all correspondence should be addressed. Tel: 979-847-9040; fax: 979-845-4450; electronic mail: LWang@tamu.edu; URL: http://oilab.tamu.edu.

ABSTRACT

The effects of wavefront distortions induced by acoustic heterogeneities in breast thermoacoustic tomography (TAT) are studied. First, amplitude distortions are shown to be insignificant for different scales of acoustic heterogeneities. Next, the effects of phase distortions (errors in time-of-flight) in our numerical studies are investigated, and the spreads of point sources and boundaries caused by the phase distortions are studied. After that, a demonstration showing that the blurring of images can be compensated for by using the distribution of acoustic velocity in the tissues in the reconstructions is presented. Last, the differences in the effects of acoustic heterogeneity and the generation of speckles in breast TAT and breast ultrasound imaging are discussed.

Keywords: thermoacoustic tomography, acoustic heterogeneity, wavefront distortion.

1. INTRODUCTION

When an electromagnetic pulse is absorbed by biological tissue, the heating and subsequent expansion causes the emission of acoustic signals. This phenomenon is called the thermoacoustic effect. In thermoacoustic tomography (TAT), the thermoacoustic signals from a tissue sample are collected to map the distribution of the radiation absorption within the sample. Radiation absorption is closely related to the physiological and pathological status of the tissue. For example, the microwave absorption rate of cancerous breast tissue is 2-5 times greater than that of the surrounding normal breast tissue. This difference has been attributed to an increase in the amount of bound water and sodium within malignant cells.[1-3.] TAT combines good imaging resolution with high imaging contrast. There are a variety of reconstruction algorithms for TAT.[4-9] An important assumption in these reconstruction algorithms is that the tissue is acoustically homogeneous. For many medical imaging applications, including imaging of the female breast, this assumption is an approximation. For example, the speed of sound in the breast can vary from 1400 m/s to 1550 m/s. Errors due to the assumption of a constant acoustic speed, which has never been studied in TAT, can potentially have a pronounced effect on image quality. In breast ultrasound tomography (UT), however, wavefront distortion has been studied extensively[10-13]. Amplitude distortion caused by refraction dominates the phase distortion induced by acoustic speed variation in the breast UT[11]. Refraction occurs where there is a speed mismatch across a tissue interface. Because of refraction, rays from a single source can reach the same receiver by different paths, as shown in Fig. 1. The interference between these rays causes strong amplitude distortion in breast UT. Different deaberration methods have been proposed to compensate for phase distortion in UT.[14,15] However, they have so far been inadequate to correct the strong amplitude distortion caused by refraction. [16]

The effects of acoustic heterogeneity on breast TAT are estimated to be weaker than those in breast UT for the following reasons. First, the signals in breast TAT are primarily in a lower frequency range (usually below 1.5 MHz [17]) than those in UT. Ultrasound scattering in this frequency range is weak. Secondly, in TAT, the acoustic source is induced by electromagnetic absorption; therefore, only one-way distortion on reception wave propagation occurs. As shown in Fig. 2, an acoustic ray, for example SB_1D, needs to pass through interface Σ only once. In contrast, in pure ultrasound imaging, either in the pulse-echo mode or in the transmission mode, ultrasound distortion includes two parts-- distortion during transmission and during reception wave propagation. Therefore, the acoustic wave has to pass through the interface at least twice, as shown in SB_2B_1D in Fig. 1. Third, if the detection distance from the objects are properly chosen, the effects of amplitude distortion can be minimized in breast TAT, as will be explained in Section 3.
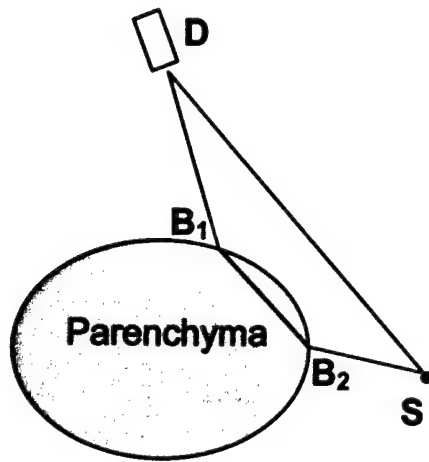
Fig. 1 Illustration of the multipath interference caused by refraction at boundary points B_1 and B_2 in breast ultrasound imaging in transmission mode. S is a point source and D is a detector.
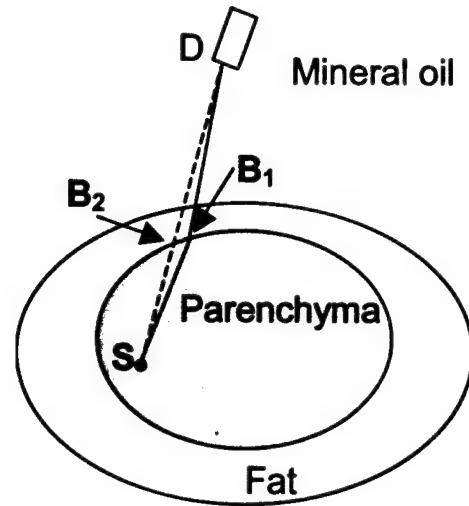
Fig. 2 Illustration of a ray refraction at the parenchyma wall with breast TAT.

In our work, we analyze the effects of amplitude distortion and numerically simulate the effects of phase distortion with the truncated conjugate gradient [18] (TCG) method. In Section 2, we derive equations for the forward problem in an acoustically homogeneous model, which yields acoustic pressure from a known distribution of microwave absorption. In Section 3, we investigate the effects of refraction on wavefront amplitude and phase in breast TAT. The inversion algorithm of TCG, and the model and parameters used in the numerical simulations, are presented in Section 4. In Section 5, the effects of phase distortion are studied numerically.

2. THE FORWARD PROBLEM IN A HOMOGENEOUS MODEL

We begin by deriving a formula for the forward problem for an acoustically homogeneous model, and then modify it, at the end of Section 3, to consider velocity heterogeneity. In the case of thermal confinement, the acoustic wave at point $\mathbf{r}$ and time t, $p_1(\mathbf{r},t)$ can be expressed as follows[19]:

$$p_1(\mathbf{r},t) = \frac{v_{s0}\beta I_0}{4\pi C}\frac{\partial}{\partial t}\iint_{t=t_f(\mathbf{r}',\mathbf{r})}\frac{\varphi(\mathbf{r}')}{|\mathbf{r}-\mathbf{r}'|}d\mathbf{r}',$$

(1)

where

$$t_f(\mathbf{r}',\mathbf{r}) = |\mathbf{r}-\mathbf{r}'|/v_{s0}$$

(2)

is the time-of-flight (TOF) from $\mathbf{r}'$ to $\mathbf{r}$ v_{s0} is the acoustic speed; C is the specific heat; β is the coefficient of the volume thermal expansion; I_0 is a scaling factor proportional to the incident radiation intensity; and $\varphi(\mathbf{r}')$ describes the to-be-reconstructed microwave absorption properties of the medium at $\mathbf{r}'$. The physical meaning of this equation is that, in an acoustically homogenous medium, the pressure p_1, at a spatial point $\mathbf{r}$ and time t, is proportional to the first-order temporal derivative of the integration of the absorbed microwave energy over a spherical surface [a circle in the two-dimensional (2-D) case]. The spherical surface is centered at $\mathbf{r}$ and has a radius of tv_{s0}.

3. THE EFFECT OF ACOUSTIC HETEROGENEITY IN TAT

A TAT model is shown in Fig. 2. In our imaging system, mineral oil is chosen as the coupling medium for both microwaves and ultrasonic waves. The acoustic speed of light in mineral oil is 1437 m/s [20], which is very close to that in fat. [23] Therefore, there should be negligible refraction at the boundary between the breast and the mineral oil, and, consequently, we will consider only the effects of acoustical heterogeneity within the breast. More details on our TAT experimental setup can be found in our previous work[8].

3.1 Amplitude distortion caused by refraction

Fig. 1 shows the multipath interference in breast ultrasound imaging in transmission mode. The acoustic ray from source S can travel to detector D by two different paths, SD and SB_2B_1D, due to refraction at the interfaces between different tissues. The interference between the two rays can cause amplitude distortion, [11] but it is not severe in breast TAT[19]. Basically, the phenomenon can be explained as follows. For wavelength-scale or smaller heterogeneities, amplitude distortion of the wavefronts is minor due to diffraction when the detectors are placed in the far field of the irregular boundary segment. When the size of the concave segment is larger, or the boundary segment is convex, according to the imaging formula of concave boundaries, only imaginary images exist after the wavefronts from real objects pass through the concave boundary. Equivalently, no two rays from a point source will intersect with each other after passing through the concave boundary segment and no strong amplitude distortion occurs.

3.2 Phase distortion caused by refraction and speed variation

If the background is acoustically homogeneous, an acoustic ray from source S in Fig. 2 goes along the straight line SD to reach detector D. When there is acoustic heterogeneity, an acoustic ray goes along line SB_1D because of refraction at the interface. Assume there is no change in the shape of the acoustic pulse caused by acoustic heterogeneity. The TOF from source S to detector D in the acoustically heterogeneous model is

$$t_{SB_1D} = \int_{SB_1D} dl / v_s(\mathbf{r}''), \tag{3}$$

where $v_s(\mathbf{r}'')$ is the local acoustic speed, and $\mathbf{r}''$ is a point within line SB_1D. Now, we will show that t_{SB_1D} can be approximated to the second order of a small value $\varepsilon = (v_s(\mathbf{r}'') - v_{s0})/v_{s0}$ by $t_{SD} = \int_{SD} dl / v_s(\mathbf{r}'')$, where v_{s0} is the velocity used in the acoustically homogeneous model. According to Fermat's principle, an acoustic ray travels on the fastest path. In another words, SB_1D is a local minimum of TOF. Now assume B_1 is displaced to B' by a small distance $q = |BB'|$,

$$\frac{q}{l_{SD}} = o(\varepsilon). \tag{4}$$

After expanding $t_{SB'D}$ around t_{SB_1D} with respect to q, we have

$$t_{SB'D} = t_{SB_1D} + q \frac{\partial t_{SB'D}}{\partial q}\bigg|_{q=0} + o(\varepsilon^2). \tag{5}$$

Recalling that SB_1D is a local minimum, we have $\dfrac{\partial t_{SB_1'D}}{\partial q}\bigg|_{q=0} = 0$. Substituting it into Eq. (5) and assuming

$l_{B_2B_1}/l_{SD} = o(\varepsilon)$, due to the weak acoustic heterogeneity in breast tissue, we have

$$t_{SD} = \int_{SD} dl / v_s(\mathbf{r}'') = t_{SB_1D} + o(\varepsilon^2). \tag{6}$$

The above result can be understood in the following way. Although the path length of SB_1D in Fig. 2 is longer than that of SD and $(l_{SB_1} + l_{DB_1} - l_{SD})/l_{SD} = o(\varepsilon)$, path SD has a longer part within the slow-speed area than path SB_1D. The combination of the two opposite effects leads to the cancellation of the first-order term of ε in Eq. (6).

Next we will show that the approximation of t_{SB_1D} by t_{SD} includes most of the flight-time variation induced by acoustic heterogeneity. The TOF from source S to detector D in an acoustically homogeneous and heterogeneous model is l_{SD}/v_{s0} and t_{SB_1D}, respectively. The difference between them is

$$\delta t = \left| t_{SB_1D} - l_{SD}/v_{s0} \right| = \left| t_{SB_1D} - t_{SD} + t_{SD} - l_{SD}/v_{s0} \right| \approx \left| o(\varepsilon^2) + t_{SD} - l_{SD}/v_{s0} \right| \approx o(\varepsilon), \tag{7}$$

where we used Eq. (6). Combining δt with Eq. (6), we have

$$\frac{\left| t_{SD} - t_{SB_1D} \right|}{\delta t} = o(\varepsilon). \tag{8}$$

Therefore, the error in the approximation of t_{SB_1D} by t_{SD} is not important. At last, it should be pointed out that our analysis of TOF can be applied to both 2-D and 3-D TAT.

3.3 Forward formula in an acoustically heterogeneous model

In our analysis of TOF, we consider only a single interface. The results can be extended to the case involving several interfaces. In general, the TOF from $\mathbf{r}$ to $\mathbf{r}'$ can be expressed as

$$t_f(\mathbf{r}', \mathbf{r}) = \int_{L(\mathbf{r}', \mathbf{r})} dl/v_s(\mathbf{r}'') + o(\varepsilon^2), \tag{9}$$

where $L(\mathbf{r}', \mathbf{r})$ is the straight line from $\mathbf{r}'$ to $\mathbf{r}$, and $\mathbf{r}''$ lies within the line L. Combining Eq. (9) and Eq. (1), we obtain the forward formula for acoustically heterogeneous TAT.

Our analysis of TOF is in agreement with the results from a more rigid model [21]. It has been reported that the variation in travel time caused directly by acoustic speed heterogeneity is a first-order perturbation and that the effect of ray bending on travel time is a second-order one. For breast tissue, which is weakly acoustically heterogeneous, it is enough to consider the first-order perturbation by computing the integral of the slowness perturbation along straight lines, as shown in Eq. (9).

4. IMPLEMENTATION AND MODELING OF NUMERICAL SIMULATIONS

Fig. 3 (a) and (b) illustrate the acoustic and RF absorption models of the breast, respectively. The acoustic model of the breast in our simulations is based on experimental results of the distribution of acoustic speed in the breast [22-23]. The mean velocity in the subcutaneous zone v_f and the breast parenchyma v_p are set to be 1437 m/s [23] and 1546 m/s, respectively. A random component, which is a normal distribution with a mean of zero and a variance of 33 m/s, is added to the velocity distribution to simulate the velocity fluctuations in the subcutaneous zone[22] and the breast parenchyma. The speed distribution in Fig. 3 was normalized to 1437 m/s. The RF absorption model of the breast is shown in Fig. 3(b). The RF absorption coefficients in the fat, tumors, and coupling oil are set to be 0.1, 3, and 0 after being normalized to that in the parenchyma. The tumors, shown in 3(b) as dark spots, are placed evenly along the horizontal direction to study the dependence of the distortions in the images based on the tumor locations. We set the radii of the four tumors to about 1.2 mm to simulate approximately the point-source spread caused by acoustic heterogeneity.

The parameters in our simulations are chosen as follows unless stated otherwise. Noise is added to the generated signals so that the frequency range with a signal-to-noise ratio (SNR) larger than unity is from 0 to 1.5 MHz, which approximates our experimental results[17]. The radius of the circle of detection is set to be 125 mm; the angle range of detection is 2π with 200 steps. An insufficient number of scanning steps can cause radial aliases in the reconstructed image[9]. Thermoacoustic signals are sampled for 108 µs at a sampling rate of about 7 MHz, which is sufficient to meet the Nyquist criteria. The 100 mm by 100 mm imaging field is mapped with a 128 by 128 mesh. In our simulations, the

thermoacoustic signals are generated in an acoustically inhomogeneous model, while the reconstruction is implemented for two cases--with and without the consideration of acoustic heterogeneity.
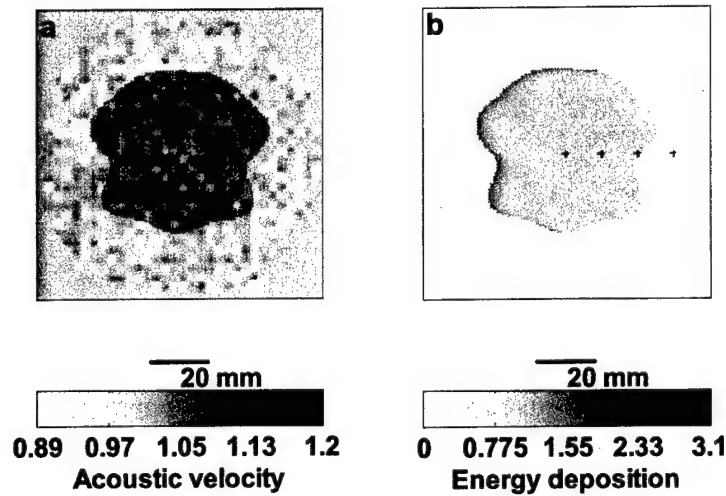

20 mm

0.89 0.97 1.05 1.13 1.2
Acoustic velocity

20 mm

0 0.775 1.55 2.33 3.1
Energy deposition

Fig. 3(a) Distribution of acoustic velocity normalized to v_{s0} for a breast model. The breast surface is represented by the outer circle; the wall between the breast parenchyma and the subcutaneous fat is represented by the inner irregular boundary. (b) The microwave absorption distribution in our model. The four small spots represent the assumed tumors.

5. NUMERICAL RESULTS

We first study the effect of acoustic heterogeneity on imaging when acoustic heterogeneity is considered in the forward problem but not in the reconstruction. In the reconstruction, $v_s(\mathbf{r})$ in Eq. (9) is set to be v_{s0}. We then show how to improve image resolution after considering acoustic heterogeneity in the reconstructions. Lastly, the effects of measurement errors in v_f, v_p and Σ on the improvement are investigated.

20 mm

-0.25 0.4 1.1 1.7 2.4
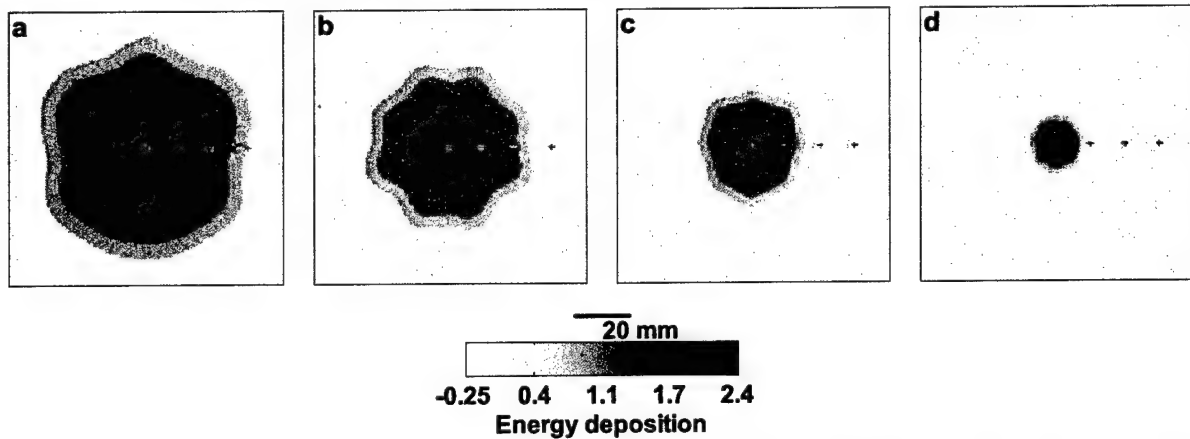**Energy deposition**

Fig. 4 (a)-(d) Images when acoustic heterogeneity is not considered in the reconstructions. The mean radii of the parenchyma wall are set to be 0.8, 0.6, 0.4 and 0.2 of the breast radius, respectively. The point-spread width and the boundary-spread width increase linearly with the size of the parenchyma tissue. Note that the spread of points outside the parenchyma tissue is much smaller than the spread inside.

5.1 Reconstruction without considering heterogeneity

Fig. 4(a)-(d) shows the results when acoustic heterogeneity is not considered in the reconstructions. In the four simulations, the mean radii of the parenchyma wall r_p are set to be 0.8, 0.6, 0.4 and 0.2 of the breast radius. The wall is distorted randomly in the simulations, and the distortion amplitude is 0.1. We measure the point-spread width (PSW), which is the width of the image of a point source along a specific direction minus its real size, 2.4 mm, and the boundary spread width (BSW), which is the width of the blurred parenchyma wall Σ in an image. It is clear from Fig. 4 that PSW and BSW increase with the radius of the parenchyma wall. It is found that the two widths can be estimated by the following equation:

$$w = l_p \alpha, \tag{10}$$

where l_p is $2r_p$ in the case of BSW; in the case of PSW, l_p is the length of a ray within the parenchyma tissue along a specific direction. The PSW is anisotropic because l_p depends on direction. This anisotropy of PSW can be verified by the observation that the three tumors within the parenchyma tissue in Fig. 4(a) and (b) have the same spread along the horizontal direction, while their spreads along the vertical direction decrease when the tumors are located away from the center.

Another interesting point in Fig. 4 is that the PSW of the objects outside the parenchyma tissue are little affected by acoustic heterogeneity. Only minor artifacts are observed near them. This is because in TAT, a π - or wider view can provide complete data for reconstruction[24]. In this case, a view means the angle subtended by the detection curve when observed from the to-be-imaged object. If an object is outside the parenchyma tissue, it has at least a π - view detection range in which the medium between the object and the detectors is acoustically homogeneous. Therefore, a perfect image can be reconstructed from this part of the data. On the other hand, the image reconstructed from the part of the signals that experience the heterogeneous medium is weak in amplitude because the flight-time errors compromise the build-up strength of the signals.

In addition to the blurring of the images, acoustic heterogeneity increases the background noise level and decreases the values of the reconstructed tumors, which consequently reduces the contrast of the tumors in the images and the detectability of small tumors. A comprehensive quantitative study of this issue will depend on the SNR of the hardware of the imaging system, the parameters of the imaging system and the reconstruction algorithms, and the contrast of the to-be-imaged objects. Meaningful conclusions should be made based on relevant experimental data which we leave for a future study.

5.2 Reconstruction with the consideration of heterogeneity

Fig. 5 and Fig. 6 show the reconstructed images with consideration of heterogeneity and the corresponding close-up images around the central tumor in Fig. 5. The exact distribution of acoustic velocity is included in the model in Fig. 5(a). Although the result is good, it is not practical, because it is not feasible to obtain the exact distribution of velocity in the breast with current technology. A much more practical situation is when the mean velocities, v_f, v_p, and boundary profile Σ are approximately known while the velocity fluctuation within each area is unknown. Here, we will show the effectiveness of our compensation method. Fig. 5 (b)-(f) shows the images reconstructed from the same data as in Fig. 5 (a), but the reconstruction algorithm used only v_f, v_p and Σ to study the effects of the measurement errors in v_f, v_p and Σ on the improvement. In Fig. 5 (b)-(f), the random component of the acoustic-velocity distribution is ignored. In addition, v_p is decreased by 1% and 3% in Fig. 5 (c) and (d), respectively; Σ is scaled down by 10% in Fig. 5 (e), and a 20% random error is introduced to Σ in Fig. 5 (f). Fig. 6(a)-(f) are the corresponding close-up images around the central tumor in Fig. 5. r_p in these simulations is 0.6 of the breast radius, and the distortion amplitude of the parenchyma wall is 0.2.

20 mm

-0.29 0.65 1.6 2.5 3.5
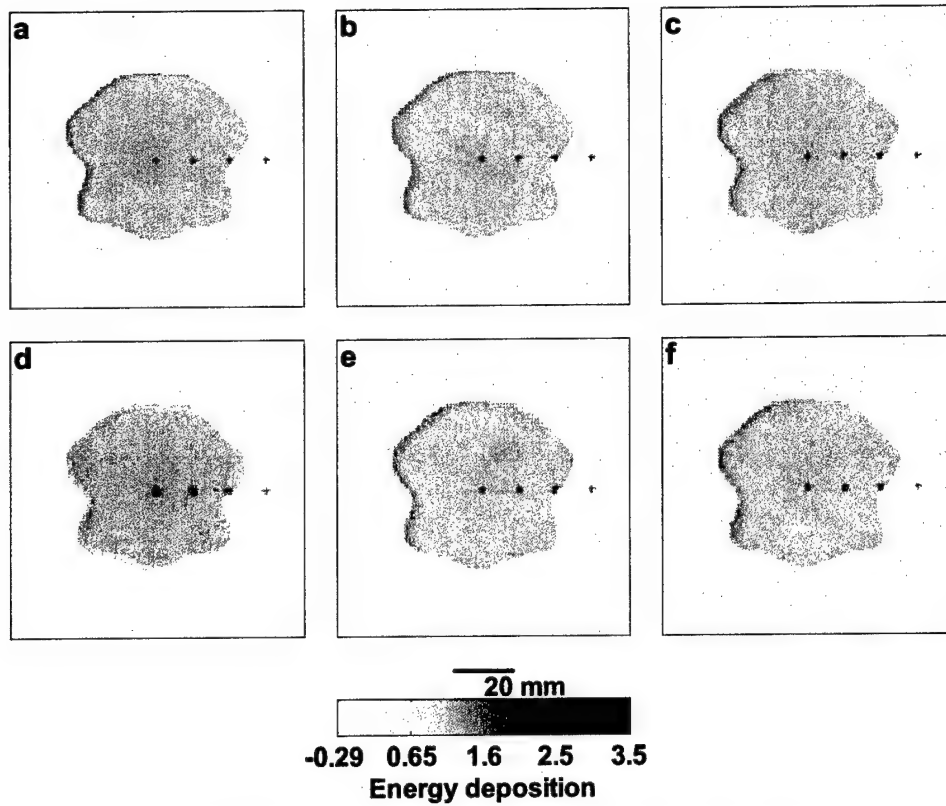**Energy deposition**

Fig. 5. (a) Compensation for the degradation in images when complete acoustic heterogeneity information is included in the reconstructions. (b) Only exact v_p, v_f, and Σ are included to show the insensitivity of improvement to a random component of the acoustic-velocity distribution. (c) and (d) Images when there are 1% and 3% errors in v_p, respectively. (e) Images when Σ is scaled down by 10%. (f) Images when 20% random error is introduced in Σ. The above results show the stability of the improvement to the errors in v_p, v_f, and Σ.

5.2.1 Effect of errors in velocities

There is little difference between the resolution of the reconstructed images when we consider [Fig. 6 (a)] and do not consider [Fig. 6 (b)], the random component of velocity distribution, although the artifacts in the background in Fig. 6 (b) are a little stronger than those in Fig. 6 (a).

Comparing Fig. 6 (c)–(d) with Fig. 6 (b), it should be noted that a 1% error in v_p does not degrade the imaging quality much, while a 3% error in v_p greatly deteriorates the imaging resolution and contrast. This is because in our model, the difference between v_f and v_p is about 7% of their speeds, and a 3% error in v_p actually accounts for 42% of the difference between v_f and v_p. Therefore, we conclude that an accuracy of 1% in the determination of v_p is sufficient for significant improvement in imaging resolution.
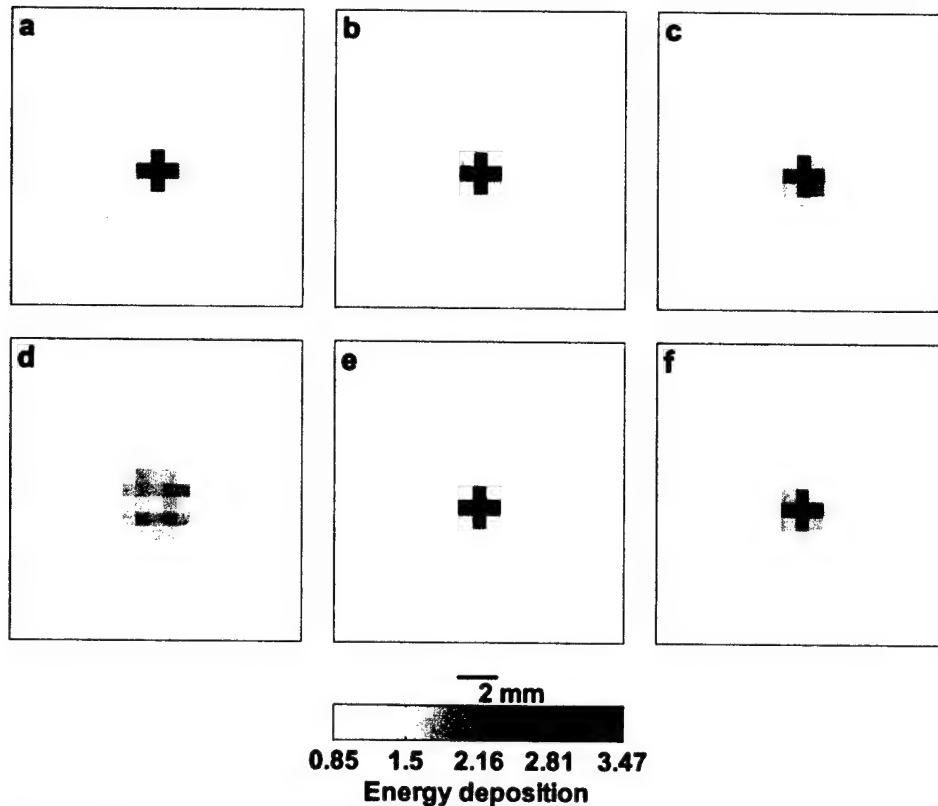
Fig. 6(a)-(f) Close-up images around the central tumor in Fig. 5 (a)-(f), respectively.

5.2.2 Effects of errors in determining Σ

In the model in Fig. 6 (e), the boundary Σ is scaled down by 10%. In Fig. 6 (f), a random component is added to the real boundary, which is implemented by multiplying the real radii of a boundary with uniform random numbers within [0.8,1.2]. After comparing Fig. 6 (e) and (f) with other figures in Fig. 6, it is found that compensation is less sensitive to error in determining Σ as v_p. This is because a 10% error, which is about 6 mm in the diameter of the parenchyma wall, adds at most 0.42 mm to the PSW and BSW according to Eq. (10).

6. DISCUSSION

The studies we presented in Section 3 show that there should be no severe amplitude distortion in breast TAT although severe amplitude distortion caused by refraction has been observed in both narrowband and broadband breast UT[11]. The difference between the effects of acoustic heterogeneity on TAT and UT can be explained by the different central frequencies. In UT, the central frequency is above 3 MHz, while in TAT, the central frequency is below 1 MHz. The higher frequency in UT results in stronger wavefront distortion for the following reasons. First, the scattering effect increases rapidly with frequency; and secondly, the minimum detection distance for avoiding strong amplitude distortion caused by an acoustic lens, which can be a boundary segment or a small inclusion, extends farther with increasing frequency. We notice that the transducer or array was placed closer than the required distance to the breast[11, 12]. Therefore, it is not surprising to observe the strong interference effect in UT.

Another important difference between TAT and UT is that there is no speckle in our TAT images[7]. Speckle is an important factor limiting the quality of pure ultrasonic imaging. In our technology, the detected signals are primary acoustic waves, rather than reflective or scattered waves as in UT. Further, the temporal frequency of the acoustic signals lies in a range from 0 to 1.5 MHz, which is only weakly scattered in the tissues. However, the issue of image speckle in more realistic medical imaging applications is a topic for future consideration.

7. CONCLUSIONS

The effects of acoustic heterogeneity on TAT in the breast are studied. Our analysis shows that the amplitude distortion in breast TAT is minor. The amplitude distortion is not severe in breast TAT, because the TAT signals are broadband, have low central frequency, and experience only one-way transmission through the parenchyma wall. Therefore, we consider only phase distortion in our numerical studies. The numerical results on the spread of point sources and boundaries caused by the phase distortion are in good agreement with the predictions of the proposed formula. It is shown that phase distortion can be compensated for when complete or partial information on the distribution of acoustic velocity in the breast is included in the reconstruction. It is discovered that improvement in the results is more sensitive to measurement error in v_f, v_p than in Σ. The differences between breast TAT and breast ultrasound imaging in relation to the effects of acoustic heterogeneity and speckles are accounted for by differences between them in their central ultrasound frequencies and detection configurations.

ACKNOWLEDGMENTS

REFERENCES

1   W. Joines, R. Jirtle, M. Rafal, and D. Schaeffer, "Microwave power absorption differences between normal and malignant tissue," Radiation Oncology-Biology-Physics vol. 6, pp. 681–687, 1980.
2   S. Chaudhary, R. Mishra, A. Swarup, and J. Thomas, "Dielectric properties of normal human the breast tissues at radiowave and microwave frequencies," Indian Journal of Biochemistry and Biophysics vol. 21, pp. 76–79, 1984.
3   W. Joines, Y. Zhang, C. Li, and R. Jirtle, "The measured electrical properties of normal and malignant human tissues from 50–900 MHz," Medical Physics vol. 21, pp. 547–550, 1994.
4   R. A. Kruger, P. Liu, Y. R. Fang, and C. R. Appledorn, "Photoacoustic ultrasound (PAUS)—reconstruction tomography," Med. Phys. vol. 22, pp. 1605–1609, 1995.
5   C. G. A. Hoelen, F. F. M. Demul, R. Pongers, and A. Dekker, "Three-dimensional photoacoustic imaging of blood vessels in tissue," Opt. Lett. vol. 23, pp. 648–650, 1998.
6   G. Ku and L.-H. V. Wang, "Scanning thermoacoustic tomography in biological tissue," Med. Phys. vol. 27, pp. 1195–1202, 2000.
7   Y. Xu, D. Feng, L.-H. V. Wang, "Exact frequency-domain reconstruction for thermoacoustic tomography: I. Planar geometry," IEEE Trans. Med. Imag., vol. 21, pp. 823 – 828, 2002.
8   M. Xu and L.-H. V. Wang, "Time-domain reconstruction for thermoacoustic tomography in a spherical geometry," IEEE Trans. Med. Imag., vol. 21, pp. 814 – 822, 2002.
9   Y. Xu, M. Xu, L. -H V. Wang, "Exact frequency-domain reconstruction for thermoacoustic tomography: II. Cylindrical geometry," IEEE Trans. Med. Imag., vol. 21, pp. 829 – 833, 2002.
10   M. Moshfeghi and R. C. Waag, "In vivo and in vitro ultrasound beam distortion measurements of a large aperture and a conventional aperture focused transducer," Ultrsound Med. Bio., vol. 5, pp. 415–428, 1988.
11   Q. Zhu and B. D. Steinberg, "Large-transducer measurements of wavefront distortion in female the breast," Ultrasonic imag. Vol. 14, pp. 276–299, 1992.
12   C. W. Manry and S. L. Broschat, "FDTD simulations for ultrasound propagation in a 2-D breast model," Ultra. Imag. Vol. 18, pp. 25–34, 1996.
13   P. D. Freiburger, D. C. Sullivan, B. H. Leblanc, S. W. Smith, and G. E. Trahey, "Two dimensional ultrasonic beam distortion in the breast: in vivo measurements and effects," Ultra. Imag. Vol. 14, pp. 398–414, 1992.
14   S. W. Flax and M. O'Donnell, "Phase aberration correction using signals from point reflectors and diffuse scatters: basic principles," IEEE Trans. Ultrason. Ferroelec. Freq. Contr., vol. 35, pp. 758–767, 1988.

[15] G. E. Trahey, D. Zhao, J. A. Miglin and S. W. Smith, "Experimental results with a real-time adaptive ultrasonic imagining system for viewing through distorting media, IEEE Trans. Ultrason. Ferroelec. Freq. Contr., vol. 37, pp. 418–427, 1990.

[16] Q. Zhu and B. D. Steinberg, "Deaberration of incoherent wavefront distortion: an approach toward inverse filtering," IEEE Trans. Ultrason. Ferroelec. Freq. Contr., vol. 44, pp. 575–589, 1997.

[17] Y. Xu and L.-H. V. Wang, "Signal processing in scanning thermoacoustic tomography in biological tissues," Medical Physics, vol. 28, pp. 1519–1524, 2001.

[18] Hansen P. C., "Rank-Deficient and Discrete Ill-Posed Problems", Philadelphia, PA: SIAM Press, 1998.

[19] Y. Xu and L.-H. V. Wang, "Effects of acoustic heterogeneity in breast thermoacoustic tomography," IEEE Trans. Ultrason. Ferroelec. Freq. Contr., in print, 2003.

[20] A. R. Selfridge, "Approxiamte properties in isotropic materials," IEEE Trans. On Sonics and Ultra., SU-32, pp. 381–394, 1985.

[21] R. Sneider, D. F. Aldridge, "Perturbation theory for travel times," J. Acoust. Soc. Am., vol. 98, pp. 1565–1569, 1995.

[22] J. F. Greenleaf, R. C. Bahn, "Clinical imaging with transmissive ultrasonic computerized tomography", IEEE Trans. Biom, Engineering, Vol. BME-28, N0. 2, 177–185, 1981.

[23] F. S. Foster, M. Strban, and G. Austin, "The ultrasound microscope: initial studies of the breast tissue," Ultra. Imag. Vol. 6, pp. 243–261, 1984.

[24] Y. Xu and L.-H. V. Wang, "Limited-view thermoacoustic tomography and reconstruction by truncated-conjugate gradient," IEEE Trans. Med. Imag., in revision, 2002.

Photoacoustic tomography of biological tissues with high cross-section resolution: Reconstruction and experiment

Xueding Wang, Yuan Xu, and Minghua Xu
Optical Imaging Laboratory, Biomedical Engineering Program, Texas A&M University, 3120 TAMU, College Station, Texas 77843-3120

Seiichirou Yokoo and Edward S. Fry
Department of Physics, Texas A&M University, 4242 TAMU, College Station, Texas 77843-4242

Lihong V. Wang[a)]
Optical Imaging Laboratory, Biomedical Engineering Program, Texas A&M University, 3120 TAMU, College Station, Texas 77843-3120

A modified back-projection approach deduced from an exact reconstruction solution was applied to our photoacoustic tomography of the optical absorption in biological tissues. Pulses from a Ti:sapphire laser (4.7 ns FWHM at 789.2 nm) were employed to generate a distribution of photoacoustic sources in a sample. The sources were detected by a wide-band nonfocused ultrasonic transducer at different positions around the imaging cross section perpendicular to the axis of the laser irradiation. Reconstructed images of phantoms made from chicken breast tissue agreed well with the structures of the samples. The resolution in the imaging cross section was experimentally demonstrated to be better than 60 μm when a 10 MHz transducer (140% bandwidth at -60 dB) was employed, which was nearly diffraction limited by the detectable photoacoustic waves of the highest frequency. © *2002 American Association of Physicists in Medicine.*
[DOI: 10.1118/1.1521720]

I. INTRODUCTION

Recently, there has been considerable interest in photoacoustic tomography, a nonionizing imaging modality based upon differential absorption of electromagnetic waves for different tissue types. It is well known that some tissues, such as malignant tumors, melanin-pigmented lesions, and blood vessels have obviously higher absorption rates compared with surrounding tissues. For example, the absorption contrast between breast tumors and normal breast tissues can be as high as 300% for 1064 nm light;[1] the absorption contrast between the blood and the surrounding medium is around 1000% for 850 nm light.[2] The thermal expansion of an absorption structure in tissue creates acoustic waves according to the thermoelastic mechanism, which can be detected by high sensitive piezoelectric devices outside the sample. Photoacoustic tomography visualizes the high optical contrast between different soft biological tissues instead of the low acoustic contrast while retaining the satisfactory spatial resolution of pure ultrasound imaging.

The photoacoustic method to detect small deeply embedded tumors has been studied by Esenaliev *et al.*[3] and Oraevsky *et al.*[4,1] In an attempt to advance the *in vivo* detection of skin cancer, photoacoustic imaging of layered tissues with optical contrast has been studied by Beenen *et al.*,[5] Oraevsky *et al.*,[6] and Karabutov *et al.*[7] Axial resolution up to 10–20 μm has been achieved. Hoelen *et al.* applied photoacoustic tomography to the detection of blood concentrations.[2] The depth resolution of blood vessel imaging in highly scattering media is about 10 μm. Paltauf *et al.* adopted an optical

method instead of piezoelectric devices for two-dimensional (2D) ultrasonic detection and achieved a spatial resolution around 10 μm.[8]

All of the above photoacoustic tomography systems can be categorized into two detection modes: (1) the forward mode, with the laser irradiation and ultrasound detection on opposite surfaces of the sample, and (2) the backward mode, with the laser irradiation and ultrasound detection on the same surface of the sample. Although high resolution along the axis of the laser irradiation can be easily achieved, the basic problem with these two modes is the poor lateral resolution, which is limited mainly by the scanning range of the detector.

When lateral resolution is the concern or the imaging purpose is to obtain a 2D image of a cross section of the sample perpendicular to the axis of the laser irradiation, a proper scheme is to arrange the receiver around the laser axis to detect the acoustic signals from the side of the sample. A focused ultrasonic transducer can be adopted to perform the linear, or sector, scan, and then the measured data is used to construct an image directly,[9] which is similar to the method used in early pulse-echo ultrasonography. An alternative method is to use a wide-band point detector to receive the acoustic signals and then reconstruct the absorption distribution based on a certain algorithm.[10,11]

On the other hand, when employing the nonfocused ultrasonic transducer for detection, the quality of the photoacoustic imaging is highly dependent on the reconstruction algorithm. Examples of approximate reconstruction algorithms

include the weighted delay-and-sum method,[12] the optimal statistical approach,[13] and the Radon transform in far-field approximation.[10,14,15] Exact reconstruction algorithms were recently derived for various detection geometries.[16-19]

In this paper, a modified back-projection method based on the circular-scan geometry was applied to the photoacoustic tomography of optical absorption in biological tissues. The modified back-projection algorithm was deduced from an exact reconstruction solution in the time domain, which will be briefly introduced in the second section. In the third section, the experimental method, as well as the imaging results in tissue phantoms, will be shown. In the fourth section, the best resolution in the cross section of our photoacoustic tomography system will be demonstrated by experimental results. The final section will present our conclusions.

II. MODIFIED BACK-PROJECTION

We are interested in tissues with inhomogeneous optical absorption but relatively homogeneous acoustic properties. When the laser pulse is very short, which is the case in our experiments, the time required for thermal diffusion is much greater than the time for the thermoacoustic transition. Consequently, the effect of heat conduction in the thermoacoustic wave equations can be ignored. As has been described previously in the literatures,[20,21] the generation of a photoacoustic wave by deposition of light energy can be expressed as

$$\frac{\partial^2 p(\mathbf{r},t)}{\partial t^2} - v_s^2 \nabla^2 p(\mathbf{r},t) = \frac{v_s^2 \beta}{C_p} \frac{\partial H(\mathbf{r},t)}{\partial t}, \quad (1)$$

where v_s is the acoustic speed; C_p is the specific heat; β is the thermal coefficient of volume expansion; and $H(\mathbf{r},t)$ is the heat-producing radiation deposited in the tissue per unit volume per unit time, which can be expressed as

$$H(\mathbf{r},t) = \varphi(\mathbf{r}) \eta(t), \quad (2)$$

where $\varphi(\mathbf{r})$ describes the optical energy deposition (also called optical absorption) within the tissue at position $\mathbf{r}$; $\eta(t)$ describes the shape of the irradiation pulse, which can be further expressed as $\eta(t) = \delta(t)$ for delta-function laser pulses.

The object of the image reconstruction is to estimate the distribution of the optical absorption $\varphi(\mathbf{r})$ of the tissue from a set of measured acoustic signals $p(\mathbf{r},t)$. For a circular scanning configuration, the exact inverse solution can be derived based on the spherical harmonic function,

$$\varphi(\mathbf{r}) = \frac{1}{4\pi^2 \lambda v_s r_0^2} \int \int_{S_0} dS_0 \int_{-\infty}^{+\infty} dk \, \bar{p}(\mathbf{r}_0,k)$$

$$\times \sum_{m=0}^{\infty} \frac{(2m+1) j_m(kr)}{h_m^{(1)}(kr_0)} P_m(\mathbf{n}\cdot\mathbf{n}_0), \quad (3)$$

where $\lambda = \beta/C_p$; $\mathbf{n} = \mathbf{r}/r$; $\mathbf{n}_0 = \mathbf{r}_0/r_0$; $\mathbf{r}_0$ is the detector position in respect to the imaging center; $k = \omega/v_s$ is the wave number; $\bar{p}(\mathbf{r}_0,k)$ is the Fourier transform of the pressure function $p(\mathbf{r}_0,t)$; S_0 is the measurement surface including

the object under investigation; $j_l(\cdot)$ and $h_l^{(1)}(\cdot)$ are the spherical Bessel and Hankel functions, respectively; and $P_l(\ )$ represents the Legendre polynomial. The detailed derivation of this exact inverse solution can be found elsewhere.

This inverse solution involves a summation of a series that is computationally time consuming. Therefore, it is desirable to simplify the solution. In the experiments, the detection radius r_0 is much larger than the wavelengths of the photoacoustic waves that are used for imaging. Therefore, we can assume $|k|r_0 \gg 1$ and use the asymptotic form of the Hankel function to simplify the above exact inverse solution Eq. (3). The approximate inverse solution has the form of

$$\varphi(\mathbf{r}) = -\frac{1}{2\pi v_s^4 \lambda} \int \int_{S_0} dS_0 \frac{1}{t} \frac{\partial p(\mathbf{r}_0,t)}{\partial t}\bigg|_{t=|\mathbf{r}_0-\mathbf{r}|/v_s}. \quad (4)$$

Actually, two compensation factors are implicit in this solution. Firstly, we introduce a weighting factor "t," which compensates for the $1/t$ attenuation of a spherical pressure wave as it propagates through a homogeneous medium. At the same time, we consider that in this type of reconstruction geometry, the contribution to a certain point P from an element of receiving area S is proportional to the subtended solid angle of this element S when viewed from the point P. The solid angle is inversely proportional to the square of the distance between the receiving element S and the point P, which leads to a compensation factor of "$1/t^2$." Combining the above two factors, we obtain a compensation factor of "$1/t$" as shown in Eq. (4).

Reference 15 gave an approximate solution of $\varphi(\mathbf{r})$ based on a three-dimensional inverse Radon transformation with the assumption that the size of an absorption object is much less than the distance between the source and the detector. In that case, the spherical surface over which the surface integral is computed approximates a plane. Actually, with the above assumption, t is nearly a constant compared to the size of the absorption object. However, in most cases, for example, the situation in our experiments, the size of an absorption object can be comparable to the distance between the source and the detector. Under this condition, the solution given by Ref. 15 is not appropriate, while our solution shown in Eq. (4) still holds and therefore is more general.

Although the modified back-projection reconstruction shown in Eq. (4) is valid for three-dimensional distributions of photoacoustic sources, we here consider only the imaging of thin slices of absorption objects in turbid media to evaluate our imaging system. The slices of absorption objects lie in the imaging plane perpendicular to the axis of laser irradiation. The photoacoustic signals from turbid media outside the imaging plane are regarded as background that will not provide information for the imaging of absorption objects. In this case, the detection of acoustic pressures over the 2π angle in the imaging plane is sufficient to achieve high resolution in the imaged cross section. For 2D imaging, the approximate inverse solution for the circular-scan geometry can be represented by
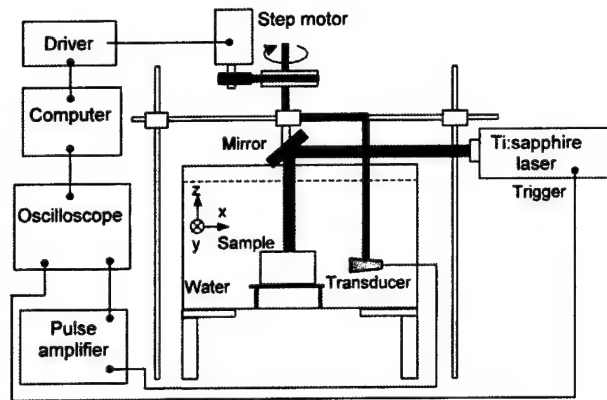
FIG. 1. Experimental setup.

$$\varphi(\mathbf{r}) = -\frac{r_0^2}{2\pi\lambda\, v_s^4} \int_{\theta_0} d\theta_0 \frac{1}{t} \left.\frac{\partial p(\mathbf{r}_0, t)}{\partial t}\right|_{t=|\mathbf{r}_0-\mathbf{r}|/v_s}, \quad (5)$$

which is an integral over θ_0 around the thin slice of the object. From Eqs. (4) and (5), we see that the reconstruction of the absorption distribution can be fulfilled by back-projection of the quantity

$$-\frac{1}{t}\left.\frac{\partial p(r_0,t)}{\partial t}\right|_{t=|r_0-r|/v_s}$$

instead of the acoustic pressure $p(\mathbf{r}_0,t)$.

If $R(t)$ is the impulse response of the detector and $P(t)$ is the pulse duration of the laser, in the time domain, we have

$$T(\mathbf{r}_0,t) = p(\mathbf{r}_0,t) * R(t) * P(t), \quad (6)$$

where $T(\mathbf{r}_0,t)$ is the piezoelectric signal detected by the transducer, and $*$ represents convolution. Then, $\partial p(\mathbf{r}_0,t)/\partial t$ in Eq. (5) can be calculated by an inverse Fourier transformation,

$$\frac{\partial p(\mathbf{r}_0,t)}{\partial t} = \mathrm{FFT}^{-1}\left[\frac{-i\omega T(\mathbf{r}_0,\omega)W(\omega)}{P(\omega)R(\omega)}\right]$$

$$= \frac{1}{2\pi}\int_{-\infty}^{+\infty}\frac{-i\omega T(\mathbf{r}_0,\omega)W(\omega)}{P(\omega)R(\omega)}\exp(-i\omega t)dt, \quad (7)$$

where $W(\omega)$ is a band-pass window function that suppresses the frequency component outside the detectable spectrum of the transducer.

III. TOMOGRAPHY IN BIOLOGICAL TISSUES

A. Experimental method

A schematic diagram of our experimental setup for photoacoustic tomography is shown in Fig. 1, where a laboratory coordinate system $[x,y,z]$ is also depicted. A flash-lamp-pumped Ti:sapphire laser operating at a wavelength of 789.2 nm with a pulse energy of approximately 30 mJ, a pulse duration of 4.7 ns FWHM, and a repetition rate of 10 Hz, was used as the light source. The laser is expanded to a 1.5 cm diameter beam when heating the sample surface from above along the laser axis; this provides an incident power density within the limit of safety for human skin (100 mJ/cm^2) according to the ANSI standard.[22] In our experiments, the area in a cross section of the sample that is imaged is defined by the size of the laser beam. The wave form and the frequency spectrum of the laser pulse are demonstrated in Figs. 2(a) and 2(b), respectively, where the curve in (b) shows the component of $R(\omega)$ in Eq. (7).
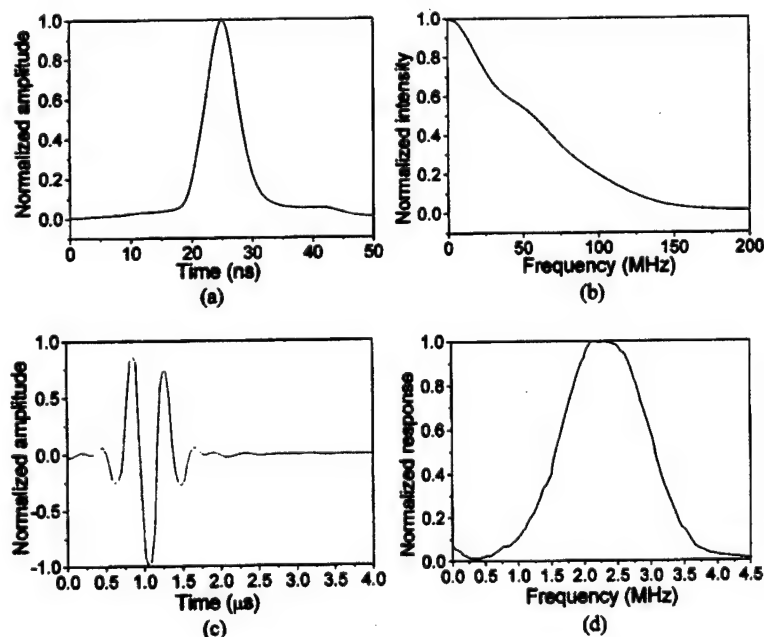

FIG. 2. (a) Wave form and (b) frequency spectrum of the 4.7 ns laser pulse. (c) Impulse response and (d) frequency response of the 2.25 MHz transducer.
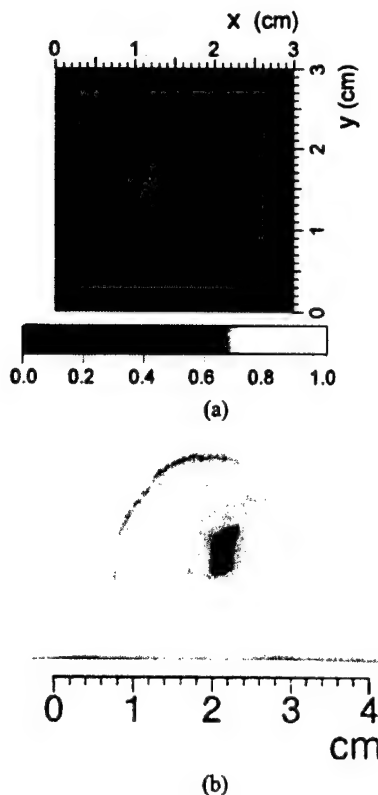
FIG. 3. Photoacoustic tomography of a slice of chicken gizzard that was buried 0.5 cm deep in the chicken breast slab. (a) Reconstructed image; (b) picture of the imaged cross-section of the sample.
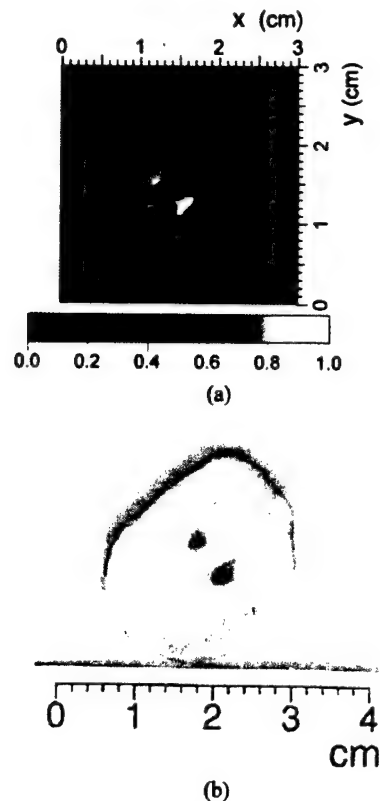

FIG. 4. Photoacoustic tomography of two slices of chicken gizzard that were buried 0.5 cm deep in the chicken breast slab. (a) Reconstructed image; (b) picture of the imaged cross-section of the sample.

The wide-band nonfocused transducer (V323, Panametrics) has a 2.25 MHz central frequency and a 6 mm diameter of the active element. The impulse response and the frequency response of the transducer are demonstrated in Figs. 2(c) and 2(d), respectively, where the curve in Fig. 2(d) shows the component of $P(\omega)$ in Eq. (7). Because the frequency bandwidth of the laser pulse is much broader than that of the transducer, $P(\omega)$ is constant and Eq. (7) can be simplified as

$$\frac{\partial p(\mathbf{r}_0,t)}{\partial t} \propto \frac{1}{2\pi} \int_{-\infty}^{+\infty} \frac{-i\omega T(\mathbf{r}_0,\omega) W(\omega)}{R(\omega)} \exp(-i\omega t) dt. \quad (8)$$

The transducer was mounted on a rotation stage that was driven by a computer-controlled step motor. The transducer scanned around the sample with a rotational step size of 1.125° and a rotational radius of 5 cm. The transducer and the sample were immersed in water. A low-noise pulse pre-amplifier (500 PR, Panametrics) amplified the acoustic signals received by the transducer and sent signals to an oscilloscope (TDS-640A, Tektronix). Then, 30 times averaged digital signals were transferred to a computer for imaging.

The experiments were performed with thin slices of gizzard tissues or red rubber pieces placed 0.5 cm deep in fresh chicken breast muscle slabs. For 789.2 nm light the reduced scattering coefficient μ_s' and the absorption coefficient μ_a for chicken breast tissue are about 1.9 cm^{-1} and 0.1 cm^{-1}, respectively.[23] Under this condition, the effective optical at-

tenuation coefficient μ_{eff} is 0.77 cm^{-1}. The blood concentration in the chicken gizzard tissue is much higher than that in the chicken breast muscle. According to our measurements, the absorption contrast between them is greater than 200%. In the experiments, the sizes of the chicken breast slabs were larger than the size of the laser beam. Therefore, the imaged area is only a part of a cross section of the sample.

B. Imaging results

Image reconstruction utilized the 2D modified back-projection algorithm described in Eq. (5). We used 1.5 mm/μs as the estimated sound velocity ν_s in soft tissues. When a detected sample has nearly homogeneous acoustic properties, the small difference between the actual sound velocity and the estimated value will not cause any distortion in the relative location of the absorption distribution in the sample. In other words, the absolute locations and sizes of the detected targets inside the sample may be changed; however, their relative positions will not be altered.

Figure 3(a) shows the reconstructed image of a thin slice of gizzard tissue buried 0.5 cm deep in a chicken breast slab. The gizzard tissue has a nearly rectangular shape (3 mm×6 mm) in the imaging plane and a thickness of about 1 mm. The picture of the cross section of this sample is shown in Fig. 3(b) for comparison. In the second sample, two slices of
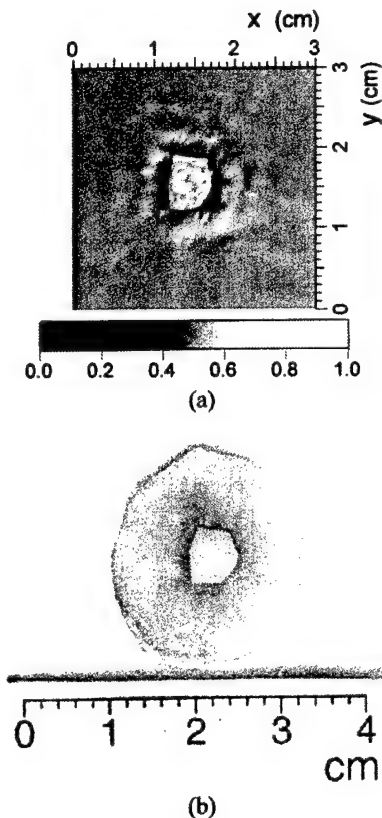
FIG. 5. Photoacoustic tomography of a slice of rubber that was buried 0.5 cm deep in the chicken breast slab. (a) Reconstructed image; (b) picture of the imaged cross-section of the sample.
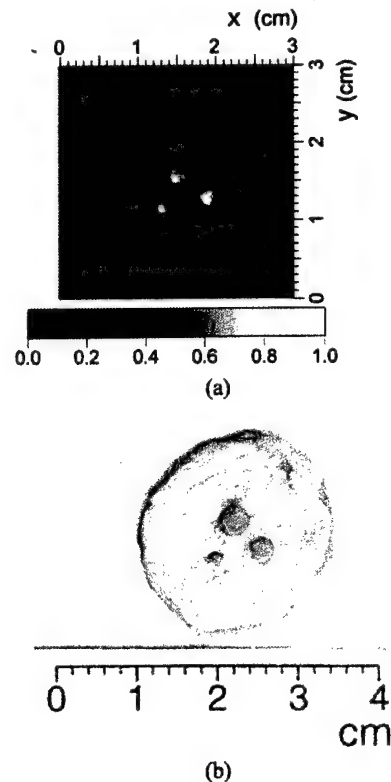

FIG. 6. Photoacoustic tomography of three slices of rubber circles that were buried 0.5 cm deep in the chicken breast slab. The radii of the three circles are 0.4 cm, 0.3 cm, and 0.1 cm, respectively. (a) Reconstructed image; (b) picture of the imaged cross-section of the sample.

gizzard tissues are placed 0.5 cm deep in a chicken breast slab, where the sizes of the two gizzard pieces are different. The reconstructed imaging is shown in Fig. 4(a) for comparison with the picture of the sample in Fig. 4(b).

Based on our experimental system as well as the reconstruction algorithm, the results of the 2D photoacoustic tomography are satisfying. The highly absorbing objects in turbid media with comparatively low absorption were localized well. The boundaries between the gizzards and the chicken breast are clearly imaged.

Because both the gizzards and the chicken breast muscles are soft biological tissues, it is difficult to avoid deformation when the samples were photographed. For this reason, the shapes of the gizzard slices in the reconstructed imaging have minor discrepancies with those appearing in the photographs. To overcome this problem, slices of red rubber pieces were used as absorption objects in some of our experiments. Figure 5(a) shows the reconstructed image of a slice of rubber (with a 1 mm thickness) that was buried 0.5 cm deep in a chicken breast slab; it fits perfectly with the picture of the sample shown in Fig. 5(b). In another sample, three circles of rubber slices with a 1 mm thickness, where the radii of the three circles are about 4 mm, 3 mm, and 1 mm, respectively, were adopted as absorption objects. In Figure 6(a), the shapes and sizes as well as the localizations of the three rubber slices are all imaged well compared with the picture

in Fig. 6(b). In the reconstructed images in Figs. 3–6, we can see some intensity fluctuations around the absorption objects, which come mainly from the photoacoustic signals generated in the background chicken breast tissues.

IV. TESTING FOR RESOLUTION

In order to quantify the actual resolution of our detection system as well as the reconstruction algorithm, well-controlled samples with high absorption contrast in transparent media were measured for imaging. Usually, the expected highest spatial resolution is estimated to be the half wavelength at the center frequency of the transducer. However, when the frequencies of the detected photoacoustic signals determining the spatial resolution are higher than the center frequency, the achievable spatial resolution is better than the estimated resolution at the center frequency. Therefore, we estimate the possible best resolution to be the half wavelength at the highest detectable photoacoustic frequency.

Pairs of parallel lines printed on transparencies were adopted as ideal testing samples, as shown in Fig. 7(a). The length and width of the dark lines was 8 mm and 0.3 mm, respectively. The gap d between the two lines was set to be 0.1 mm, 0.2 mm, and 0.3 mm, respectively. Each piece of transparency with a pair of dark lines was placed in the imaging plane. The 2.25 MHz nonfocused transducer scanned-
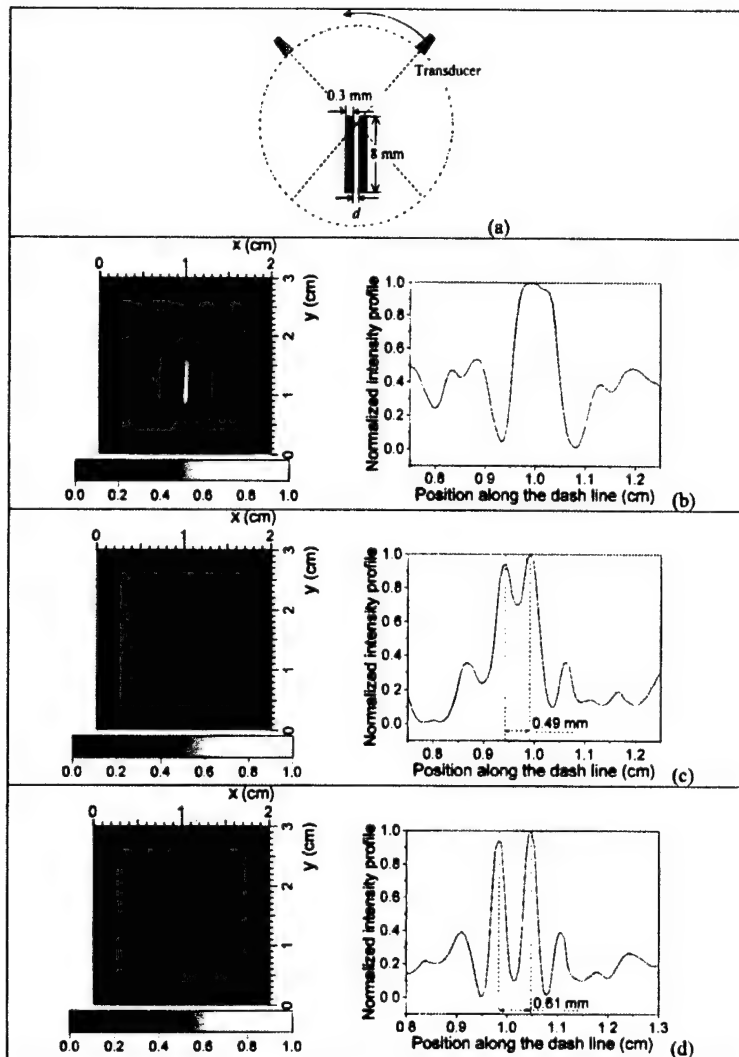
FIG. 7. (a) Schematic of a pair of parallel lines printed on transparency. The length of the two lines is 8 mm; the width of the two lines is 0.3 mm; and the gap between the two lines was *d*. The radius of the circular-scan is 50 mm. (b), (c), and (d) are the reconstructed images of the pairs of parallel lines with a gap *d* of 0.1 mm, 0.2 mm, and 0.3 mm, respectively. The profiles of reconstructed absorption intensities along the dash lines in 2D images are demonstrated as the right pictures in (b), (c), and (d), respectively.

around the transparency with a radius of 5 cm. The detectable frequency band of the transducer is from 0 to 4.5 MHz. Therefore, the estimated highest spatial resolution is 0.17 mm. The reconstructed 2D images of these pairs of lines are
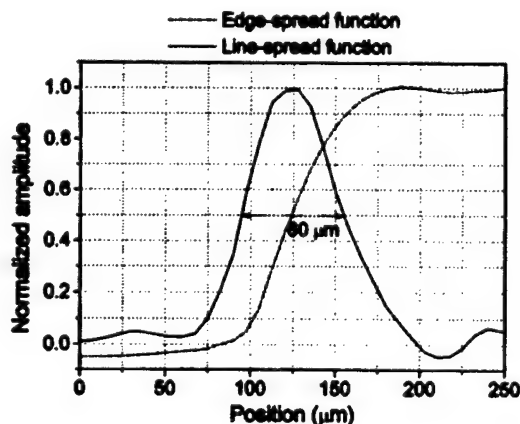

FIG. 8. Edge-spread function and line-spread function of our photoacoustic imaging system with a 10 MHz transducer.

shown in Figs. 7(b), 7(c), and 7(d) for *d* equals 0.1 mm, 0.2 mm, and 0.3 mm, respectively. The intensity profiles along the dashed lines (*y*=1.5 cm) in the 2D images are also presented. When *d* equals 0.2 mm or 0.3 mm, the two parallel lines can be recognized with an obvious gap between them. However, when *d* equals 0.1 mm, we can see only one line in the reconstructed image. In each image, there are some weak intensity fluctuations around the pair of lines, which come mainly from acoustic reflection at the edge of the transparency piece. The results in Fig. 7 show that with the circular-scan method and the modified back-projection algorithm, we can achieve a spatial resolution of ~0.2 mm.

The center of the circular scan in the experiments is taken at the center of each reconstructed image. We can see that in these 2D images, the spatial resolution at a position near the imaging center is higher than that at a longer distance from the imaging center. This kind of blur in the reconstructed image is mainly caused by the physical size of the transducer. The blur is greater when the physical size of the transducer is larger, or the distance from the imaging center is larger.

We quantified the spatial resolution of our imaging system with a 10 MHz wide-band (140% at −60 dB) cylindrically focused transducer (V312, Panametrics). The transducer has a 6 mm diameter active element and is nonfocused in the imaging plane. The estimated highest spatial resolution of our imaging system with this transducer is about 45 μm. A well-controlled phantom made from red rubber with a high optical absorption contrast and a sharp edge has been imaged to obtain the edge-spread function. A line-spread function was obtained through differentiating the profile of the edge-spread function. Both the two profiles are shown in Fig. 8. The line-spread function shows a full width at half maximum of about 60 μm, which shows that the spatial resolution of our photoacoustic imaging system is near the diffraction limit of the detected photoacoustic signals.

V. CONCLUSION

Pulsed-laser induced photoacoustic tomography of absorption in biological tissues has been studied. A modified back-projection algorithm derived from an exact inverse solution was used to reconstruct the signals received by a wideband nonfocused transducer that scanned circularly around the sample under detection. Reconstructed images of gizzard slices and rubber slices buried in chicken breast tissues agree well with the pictures of samples. Experiments also quantified the highest 2D resolution that can be achieved by this imaging system: using a detection of 2π view, the spatial resolution is nearly diffraction limited by the detected photoacoustic waves.

Our photoacoustic detection system with the modified back-projection reconstruction algorithm is proved to be an effective method for biological tissue imaging with high contrast and high spatial resolution. If a high resolution along the laser axis is required at the same time, scanning of acoustic signals along the axis will be necessary.

a)Author to whom correspondence should be addressed. Electronic mail: lwang@tamu.edu (URL: http//oilab.tamu.edu).

[1] A. A. Oraevsky, V. A. Andreev, A. A. Karabutov, D. R. Fleming, Z. Gatalica, H. Singh, and R. O. Esenaliev, "Laser opto-acoustic imaging of the breast: detection of cancer angiogenesis," Proc. SPIE **3597**, 352–363 (1999).

[2] C. G. A. Hoelen, F. F. M. de Mul, R. Pongers, and A. Dekker, "Three-dimensional photoacoustic imaging of blood vessels in tissue," Opt. Lett. **23**, 648–650 (1998).

[3] R. O. Esenaliev, A. A. Karabutov, and A. A. Oraevsky, "Sensitivity of laser opto-acoustic imaging in detection of small deeply embedded tumors," IEEE J. Sel. Top. Quantum Electron. **5**, 981–988 (1999).

[4] R. O. Esenaliev, F. K. Tittel, S. L. Thomsen, B. Fornage, C. Stelling, A. A. Karabutov, and A. A. Oraevsky, "Laser optoacoustic imaging for breast cancer diagnostics: Limit of detection and comparison with x-ray and ultrasound imaging," Proc. SPIE **2979**, 71–82 (1997).

[5] A. Beenen, G. Spanner, and R. Niessner, "Photoacoustic depth-resolved analysis of tissue models," Appl. Spectrosc. **51**, 51–57 (1997).

[6] A. A. Oraevsky, R. O. Esenaliev, and A. Karabutov, "Laser optoacoustic tomography of layered tissues: Signal processing," Proc. SPIE **2979**, 59–70 (1997).

[7] A. A. Karabutov, E. V. Savateeva, and A. A. Oraevsky, "Imaging of layered structures in biological tissues with opto-acoustic front surface transducer," Proc. SPIE **3601**, 284–295 (1999).

[8] G. Paltauf and H. Schmidt-Kloiber, "Optical method for two-dimensional ultrasonic detection," Appl. Phys. Lett. **75**, 1048–1050 (1999).

[9] M. H. Xu, G. Ku, and L. V. Wang, "Microwave-induced thermoacoustic tomography using multi-sector scanning," Med. Phys. **28**, 1958–1963 (2001).

[10] R. A. Kruger, P. Liu, Y. R. Fang, and C. R. Appledorn, "Photoacoustic ultrasound (PAUS)–Reconstruction tomography," Med. Phys. **22**, 1605–1609 (1995).

[11] A. M. Reyman, I. V. Yahovlev, A. G. Kirillov, and V. V. Lozhkarev, "Deep tomography of biological tissues by optoacoustic method," Proc. SPIE **4256**, 159–166 (2001).

[12] C. G. A. Hoelen and de F. F. M. Mul, "Image reconstruction for photoacoustic scanning of tissue structures," Appl. Opt. **39**, 5872–5883 (2000).

[13] Y. V. Zhulina, "Optimal statistical approach to optoacoustic image reconstruction," Appl. Opt. **39**, 5971–5977 (2000).

[14] R. A. Kruger, D. R. Reinecke, and G. A. Kruger, "Thermoacoustic computed tomography–technical considerations," Med. Phys. **26**, 1832–1837 (1999).

[15] R. A. Kruger, W. L. Kiser, K. D. Miller, H. E. Reynolds, D. R. Reinecke, G. A. Kruger, and P. J. Hofacker, "Thermoacoustic CT: imaging principles," Proc. SPIE **3916**, 150–159 (2000).

[16] K. Kostli, M. Frenz, H. Bebie, and H. Weber, "Temporal backward projection of optoacoustic pressure transients using Fourier transform methods," Phys. Med. Biol. **46**, 1863–1872 (2001).

[17] M. Xu and L. V. Wang, "Time-domain reconstruction for thermoacoustic tomography in a spherical geometry," IEEE Trans. Med. Imaging **21**, 814–822 (2002).

[18] Y. Xu, D. Feng, and L. V. Wang, "Exact frequency-domain reconstruction for thermoacoustic tomography: I. Planar geometry," IEEE Trans. Med. Imaging **21**, 823–828 (2002).

[19] Y. Xu, M. Xu, and L. V. Wang, "Exact frequency-domain reconstruction for thermoacoustic tomography: II. Cylindrical geometry," IEEE Trans. Med. Imaging **21**, 829–833 (2002).

[20] G. J. Diebold, T. Sun, and M. I. Khan, "Photoacoustic waveforms generated by fluid bodies," in *Photoacoustic and Photothermal Phenomena III*, edited by D. Bicanic (Springer-Verlag, Berlin, Heidelberg, 1992), pp. 263–269.

[21] V. E. Gusev and A. A. Karabutov, *Laser Optoacoustics* (American Institute of Physics, New York, 1993).

[22] American National Standards Institute, American national standard for the safe use of lasers. Standard Z136.1-2000 (ANSI, Inc., New York, NY, 2000).

[23] G. Marquez, L. V. Wang, S. P. Lin, J. A. Schwartz, and S. L. Thomsen, "Anisotropy in the absorption and scattering spectra of chicken breast tissue," Appl. Opt. **37**, 798–804 (1998).

Analytic explanation of spatial resolution related to bandwidth and detector aperture size in thermoacoustic or photoacoustic reconstruction

Minghua Xu and Lihong V. Wang*

*Optical Imaging Laboratory, Department of Biomedical Engineering, Texas A&M University, 3120 TAMU,
College Station, Texas 77843-3120*

An analytic explanation of the spatial resolution in thermoacoustic or photoacoustic reconstruction is presented. Three types of specific recording geometries, including spherical, planar, and cylindrical surface, as well as other general cases, are investigated. Analytic expressions of the point-spread functions (PSF's), as a function of the bandwidth of the measurement system and the finite size of the detector aperture, are derived based on rigorous reconstruction formulas. The analyses clearly reveal that the dependence of the PSF's on the bandwidth of all recording geometries shares the same space-invariant expression while the dependence on the aperture size of the detector differs. The bandwidth affects both axial and lateral resolutions; in contrast, the detector aperture blurs the lateral resolution greatly but the axial resolution only slightly.

I. INTRODUCTION

In the last decade, thermoacoustic or photoacoustic tomography of soft tissue utilizing excitation from a pulsed electromagnetic (EM) energy source, such as radio frequency or laser, has attracted considerable attention [1–12]. With this technique, it is assumed that, following a short pulse of EM illumination, a spatial distribution of acoustic pressure inside the tissue is simultaneously excited by thermoelastic expansion, which acts as a source for acoustic response. The intensity of the acoustic pressure is strongly related to the locally absorbed EM energy. A wide range of EM absorption coefficients in soft tissue contributes to a good contrast between different types of tissues. The effect of thermal diffusion on thermoacoustic or photoacoustic waves in tissue is always ignored, since the EM pulse duration is often so short that the thermal conduction time is far greater than the acoustic transit time through the heterogeneities of the EM energy depositions. The acoustic waves from the initial acoustic source propagate toward the surface of the tissues with various time delays. Ultrasound detectors are placed around the tissue to record the outgoing acoustic waves, referred to as the thermoacoustic or photoacoustic signals, which carry information about EM absorption as well as about the acoustic properties of the tissue. For medical imaging and diagnostics, an appropriate reconstruction algorithm is required to map the initial acoustic sources, or EM absorption distribution.

To detect thermoacoustic signals, one approach is to use focused ultrasound transducers, in which the lateral resolution is determined by the focal diameter of the transducer and the axial resolution by the bandwidth [5,6]. Another approach is to use small-aperture unfocused detectors—ideally, point detectors—that can receive ultrasound from a large

angle of acceptance. Thus far, rigorous reconstruction algorithms have been reported with point-detector measurements from idealized recording configurations, including the fully enclosing spherical recording surface [7], the planar recording surface of an infinite extent [3,8], and the cylindrical recording surface of an infinite length [9]. In these algorithms, the acoustic property of the tissue is often assumed to be homogenous as the speed of sound in soft tissue is relatively constant at ~ 1.5 mm/μs. Details can be found in Ref. [7] of the reconstruction formulas for spherical geometry and in Refs. [8,9,11] for the planar and cylindrical geometries.

Spatial resolution is one of the most important parameters in thermoacoustic reconstruction. Acoustic inhomogeneity blurs the reconstructed image, but in some cases, the blurring can be corrected. A limited view also affects spatial resolution due to lack of sufficient data; in this case, the reconstruction is incomplete and reconstruction artifacts occur [12]. These two topics will not be addressed in this paper. There are two other main factors that limit spatial resolution—the finite bandwidth of the detection system and the size of the detector aperture. Past research work has only estimated the spatial resolution in thermoacoustic tomography based on measurements or numerical simulations. No theoretical analysis has been reported.

In this paper, a complete theoretical explanation of the degree of spatial resolution that results from varying the bandwidth as well as the detector aperture will be presented. Analytic expressions of point-spread functions (PSF's) on the spherical, planar, and cylindrical recording surfaces will be explicitly derived. The paper is organized as follows. In Sec. II, the inverse problem and the reconstruction formulas for thermoacoustic tomography will be briefly reviewed. Detailed derivations of bandwidth-limited PSF's in the above three measurement geometries as well as more general cases will be presented in Secs. III A, III B, III C, and III D, respectively; and resolution will be discussed in Sec. III E. In Sec. IV, detailed derivations of PSF's as a function of detector aperture size will be shown in Secs. IV A, IV B, and IV C. Section V will provide discussion and conclusions.

---

*Author to whom all correspondence should be addressed. FAX: 979-845-4450; electronic address: LWang@tamu.edu; URL: http://oilab.tamu.edu

II. RECONSTRUCTION FORMULAS

We will first briefly review the inverse problem and the rigorous reconstruction formulas for thermoacoustic tomography. It is well known that, in response to a heat source, the pressure $p(\mathbf{r},t)$ at position $\mathbf{r}$ and time t in an acoustically homogeneous medium obeys the following equation [13]:

$$\nabla^2 p(\mathbf{r},t) - \frac{1}{c^2}\frac{\partial^2}{\partial t^2}p(\mathbf{r},t) = -\frac{\beta}{C_p}\frac{\partial}{\partial t}H(\mathbf{r},t), \quad (1)$$

where C_p is the specific heat, $H(\mathbf{r},t)$ is the heating function defined as the thermal energy deposited by the EM radiation per time and volume, β is the isobaric volume expansion coefficient, and c is the speed of sound. The heating function can be written as the product of a spatial absorption function and a temporal illumination function:

$$H(\mathbf{r},t) = A(\mathbf{r})I(t). \quad (2)$$

Assuming that the illumination is a Dirac δ function such as $I(t) = \delta(t)$, and taking the following Fourier transform on variable $\bar{t} = ct$,

$$\tilde{p}(\mathbf{r},k) = \int_{-\infty}^{+\infty} p(\mathbf{r},\bar{t})\exp(ik\bar{t})d\bar{t}, \quad (3)$$

the solution of Eq. (1) becomes the integral

$$\tilde{p}(\mathbf{r}_0,k) = -ikc^2\eta \int\int\int_V d^3r\, A(\mathbf{r})\tilde{G}_k(\mathbf{r},\mathbf{r}_0), \quad (4)$$

where $\eta = \beta/C_p$ and $\tilde{G}_k(\mathbf{r},\mathbf{r}_0)$ is the Green's function satisfying the following equation:

$$(\nabla^2 + k^2)\tilde{G}_k(\mathbf{r},\mathbf{r}_0) = -\delta(\mathbf{r}-\mathbf{r}_0). \quad (5)$$

In general, the Green's function in three-dimensional free space can be written as [14]

$$\tilde{G}_k(\mathbf{r},\mathbf{r}_0) = \frac{\exp(ik|\mathbf{r}-\mathbf{r}_0|)}{4\pi|\mathbf{r}-\mathbf{r}_0|}. \quad (6)$$

Actually, the initial thermoacoustic pressure excited by the $\delta(t)$ EM illumination is equal to $p_0(\mathbf{r}) = \Gamma(\mathbf{r})A(\mathbf{r})$, where the Grüneisen parameter $\Gamma(\mathbf{r}) = \eta(\mathbf{r})c^2$ may be inhomogeneous. Then, Eq. (4) can be expressed by the following form:

$$\tilde{p}(\mathbf{r}_0,k) = -ik \int\int\int_V d^3r\, \tilde{G}_k(\mathbf{r},\mathbf{r}_0)p_0(\mathbf{r}). \quad (7)$$

The inverse problem is to reconstruct the absorption distribution $A(\mathbf{r})$ or the initial thermoacoustic pressure distribution $p_0(\mathbf{r})$ from a set of data $p(\mathbf{r}_0,t)$ or $\tilde{p}(\mathbf{r}_0,k)$ measured at position $\mathbf{r}_0$. In general, the Green's function can be expanded in terms of some appropriate functions for the corre-

sponding recording geometries. Then, based on the orthogonality of the appropriate functions, reconstruction formulas can be derived.

In spherical recording geometry, it is assumed that the recording surface is a spherical surface $\mathbf{r}_0 = (r_0,\theta_0,\varphi_0)$ in the spherical polar coordinates $\mathbf{r} = (r,\theta,\varphi)$, where θ is the polar angle from the z axis and φ is the azimuthal angle in the x-y plane from the x axis. The sample under study lies inside the sphere, i.e., $A(\mathbf{r}) = A(r,\theta,\varphi)$ where $r < r_0$ and $A(\mathbf{r}) = 0$ when $r > r_0$. The rigorous reconstruction formula for $A(\mathbf{r})$ can be written as [7]

$$A(\mathbf{r}) = \frac{1}{2\pi^2 c^2 \eta}\int\int_{\Omega_0}d\Omega_0\int_0^{+\infty}dk\,\tilde{p}(\mathbf{r}_0,k)$$
$$\times \sum_{m=0}^{\infty}\frac{(2m+1)j_m(kr)}{h_m^{(1)}(kr_0)}P_m(\mathbf{n}_0\cdot\mathbf{n}), \quad (8)$$

where $d\Omega_0 = \sin\theta_0 d\theta_0 d\varphi_0$; $\mathbf{n} = \mathbf{r}/r$ and $\mathbf{n}_0 = \mathbf{r}_0/r$ are unit vectors; $j_m(\cdot)$, $h_m^{(1)}(\cdot)$, and $P_m(\cdot)$ are the spherical Bessel function of the first kind, the spherical Hankel function of the first kind, and the Legendre polynomial function, respectively. In addition, the integral range over variable k in Eq. (8) can extend to from $-\infty$ to 0 by simply taking the complex conjugate and using the following properties: $\tilde{p}^*(\mathbf{r}_0,k) = \tilde{p}(\mathbf{r}_0,-k)$, $[j_n(z)]^* = j_n(z)$, and $[h_n^{(1)}(z)]^* = h_n^{(2)}(z)$ when z is real and positive, where "$*$" stands for the complex conjugate.

In planar recording geometry, it is assumed that the measurement surface is the $z = 0$ plane, i.e., $\mathbf{r}_0 = (x_0,y_0,0)$ in the Cartesian coordinates $\mathbf{r} = (x,y,z)$. The sample lies above the plane, i.e., $A(\mathbf{r}) = A(x,y,z)$ where $z > 0$ and $A(\mathbf{r}) = 0$ when $z < 0$. The rigorous reconstruction formula for $A(\mathbf{r})$ can be written as [8,11]

$$A(x,y,z) = \frac{1}{4\pi^3 c^2 \eta}\int\int_{-\infty}^{+\infty}dx_0 dy_0\int_{-\infty}^{+\infty}dk\,\tilde{p}(\mathbf{r}_0,k)$$
$$\times \int\int_{\rho=0}^{\rho=|k|}du\,dv$$
$$\times \exp[-iz\,\mathrm{sgn}(k)\sqrt{k^2-\rho^2}]\exp[iu(x_0-x)$$
$$+iv(y_0-y)], \quad (9)$$

where $\rho = \sqrt{u^2+v^2}$, $\mathrm{sgn}(k) = 1$ when $k > 0$, and $\mathrm{sgn}(k) = -1$ when $k < 0$.

In cylindrical recording geometry, it is assumed that the measurement surface is a circular cylindrical surface $\mathbf{r}_0 = (\rho_0,\varphi_0,z_0)$ in the circular cylindrical coordinates $\mathbf{r} = (\rho,\varphi,z)$. The sample lies in the cylinder, i.e., $A(\mathbf{r}) = A(\rho,\varphi,z)$ when $\rho < \rho_0$, and $A(\mathbf{r}) = 0$ when $\rho > \rho_0$. The rigorous reconstruction formula for $A(\mathbf{r})$ can be written as [9,11]
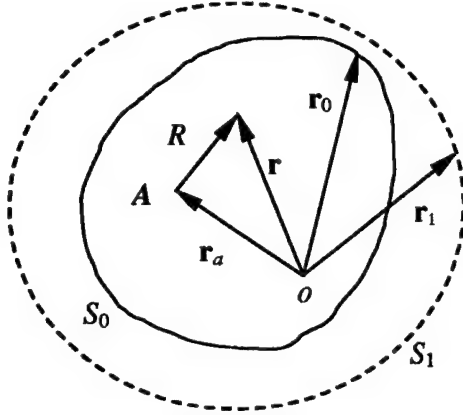
FIG. 1. Diagram of the recording geometry: a recording surface S_1 completely encloses another recording surface S_0; there is a point source A at $\mathbf{r}_a$ inside S_0; R is the distance between an arbitrary point at $\mathbf{r}$ and the point source A; $\mathbf{r}_0$ and $\mathbf{r}_1$ point to a detection element on the surfaces S_0 and S_1, respectively.

$$A(\rho,\varphi,z) = \frac{1}{2\pi^3 c^2 \eta} \int_0^{2\pi} d\varphi_0 \int_{-\infty}^{+\infty} dz_0 \int_0^{+\infty} dk \tilde{p}(\mathbf{r}_0,k)$$

$$\times \int_{-k}^{+k} d\gamma \exp[i\gamma(z_0 - z)]$$

$$\times \sum_{n=-\infty}^{+\infty} \exp[in(\varphi_0 - \varphi)] \frac{J_n(\rho\sqrt{k^2 - \gamma^2})}{H_n^{(1)}(\rho_0\sqrt{k^2 - \gamma^2})}, \tag{10}$$

where $J_n(\cdot)$ and $H_n^{(1)}(\cdot)$ are the Bessel function of the first kind and the Hankel function of the first kind, respectively. In addition, the integral range over variable k in Eq. (10) can extend to from $-\infty$ to 0, by simply taking the complex conjugate and using the following properties: $\tilde{p}^*(\mathbf{r}_0,k) = \tilde{p}(\mathbf{r}_0, -k)$, $[J_n(z)]^* = J_n(z)$, and $[H_n^{(1)}(z)]^* = H_n^{(2)}(z)$ when z is real and positive.

III. BANDWIDTH-LIMITED PSF

As shown in Fig. 1, assuming a point source $A(\mathbf{r}) = \delta(\mathbf{r} - \mathbf{r}_a)$ at $\mathbf{r}_a$, the pressure at the recording point $\mathbf{r}_0$ can be expressed as

$$\tilde{p}(\mathbf{r}_0,k) = -ikc^2 \eta \tilde{G}_k(\mathbf{r}_a,\mathbf{r}_0). \tag{11}$$

Suppose the detection system is bandlimited in the temporal-frequency domain and characterized by a low-pass function $\tilde{H}(k)$. The amplitude of the acoustic wave vector $k = \omega/c$, where ω is the acoustic angular frequency. The detected signal at the recording surface $\mathbf{r}_0$ becomes $\tilde{p}'(\mathbf{r}_0,k) = \tilde{H}(k)\tilde{p}(\mathbf{r}_0,k)$ instead of $\tilde{p}(\mathbf{r}_0,k)$. But the reconstruction formulas, Eqs. (8)–(10), for point-detector measurements in the spherical, planar, and cylindrical recording geometries, respectively, remain the same. Replacing $\tilde{p}(\mathbf{r}_0,k)$ by $\tilde{p}'(\mathbf{r}_0,k)$ in these reconstruction formulas will give us the

bandwidth-limited analytic expressions of the PSF's to be derived below for the different geometries.

A. Spherical geometry

The point source at $\mathbf{r}_a = (r_a, \theta_a, \varphi_a)$ in the spherical coordinates can be written as

$$A(\mathbf{r}) = \frac{1}{r^2} \delta(r - r_a) \delta(\varphi - \varphi_a) \delta(\cos\theta - \cos\theta_a). \tag{12}$$

The Green's function can be expanded according to the following identity $(r_0 > r_a, k > 0)$ [14]:

$$\tilde{G}_k(\mathbf{r}_a,\mathbf{r}_0) = \frac{ik}{4\pi} \sum_{l=0}^{\infty} (2l+1)j_l(kr_a)h_l^{(1)}(kr_0)P_l(\mathbf{n}_a \cdot \mathbf{n}_0), \tag{13}$$

where $\mathbf{n}_a = \mathbf{r}_a / r_a$.

Replacing $\tilde{p}(\mathbf{r}_0,k)$ by $\tilde{p}'(\mathbf{r}_0,k)$ in Eq. (8) and considering the following identity [14]:

$$\int\int_{\Omega_0} d\Omega_0 P_l(\mathbf{n}_a \cdot \mathbf{n}_0)P_m(\mathbf{n}_0 \cdot \mathbf{n}) = \frac{4\pi}{2l+1}\delta_{lm}P_l(\mathbf{n}_a \cdot \mathbf{n}), \tag{14}$$

the resulting reconstruction for $A(\mathbf{r})$ is

$$A_b(\mathbf{r}) = \frac{1}{2\pi^2} \int_0^{+\infty} \tilde{H}(k)k^2 dk \sum_{m=0}^{\infty} (2m+1)$$

$$\times P_m(\mathbf{n}_a \cdot \mathbf{n})j_m(kr_a)j_m(kr). \tag{15}$$

Further, taking into account the following identity [15]:

$$\sum_{m=0}^{\infty} (2m+1)P_m(\mathbf{n}_a \cdot \mathbf{n})j_m(kr_a)j_m(kr) = \frac{\sin(kR)}{kR} = j_0(kR), \tag{16}$$

where $R = \sqrt{r_a^2 + r^2 - 2r_a r \cos(\mathbf{n}_a \cdot \mathbf{n})}$, one can obtain

$$A_b(\mathbf{r}) = \frac{1}{2\pi^2} \int_0^{+\infty} \tilde{H}(k)j_0(kR)k^2 dk. \tag{17}$$

Particularly, if $\tilde{H}(k) \equiv 1$ for $k = 0 \to \infty$, considering the following identities [14]:

$$\int_0^{+\infty} j_m(kr)j_m(kr_a)k^2 dk = \frac{\pi}{2r^2}\delta(r - r_a), \tag{18}$$

$$\sum_{m=0}^{\infty} (2m+1)P_m(\mathbf{n}_a \cdot \mathbf{n}) = 4\pi\delta(\varphi - \varphi_a)\delta(\cos\theta - \cos\theta_a), \tag{19}$$

Eq. (15) reduces to a point source the same as the expression in Eq. (12), which actually verifies the reconstruction Eq. (8).

B. Planar geometry

The point source at $\mathbf{r}_a = (x_a, y_a, z_a)$ in the Cartesian coordinates can be written as

$$A(x,y,z) = \delta(x-x_a)\delta(y-y_a)\delta(z-z_a). \quad (20)$$

The Green's function can be expanded as [14]

$$\tilde{G}_k(\mathbf{r}_a, \mathbf{r}_0) = \frac{1}{(2\pi)^3} \int\int\int_{-\infty}^{+\infty} d^3K \frac{\exp[i\mathbf{K}\cdot(\mathbf{r}_0 - \mathbf{r}_a)]}{K^2 - k^2}, \quad (21)$$

where $\mathbf{K} = (K_x, K_y, K_z)$.

Using the detected signal at the recording surface $\mathbf{r}_0$, $\tilde{p}'(\mathbf{r}_0,k) = \tilde{H}(k)\tilde{p}(\mathbf{r}_0,k)$, to replace $\tilde{p}(\mathbf{r}_0,k)$ in the reconstruction Eq. (9), and considering the following identities:

$$\int_{-\infty}^{+\infty} \exp[i(u+K_x)x_0]dx_0 = 2\pi\delta(K_x + u), \quad (22)$$

$$\int_{-\infty}^{+\infty} \exp[i(v+K_y)y_0]dy_0 = 2\pi\delta(K_y + v), \quad (23)$$

$$\int_{-\infty}^{+\infty} dK_z \frac{\exp(-iK_z z_a)}{K_z^2 + \rho^2 - k^2}$$
$$= i\pi \operatorname{sgn}(k) \frac{\exp[iz_a \operatorname{sgn}(k)\sqrt{k^2-\rho^2}]}{\sqrt{k^2-\rho^2}}, \quad |k| > \rho, \quad (24)$$

the resulting reconstruction for $A(\mathbf{r})$ is

$$A_b(x,y,z) = \frac{1}{(2\pi)^3} \int_{-\infty}^{+\infty} k\,dk\,\tilde{H}(k) \int\int_{\rho=0}^{\rho=|k|} du\,dv$$
$$\times \exp(-iu\Delta x - iv\Delta y)$$
$$\times \operatorname{sgn}(k) \frac{\exp[-i\operatorname{sgn}(k)\Delta z\sqrt{k^2-\rho^2}]}{\sqrt{k^2-\rho^2}}, \quad (25)$$

where $\Delta x = x - x_a$, $\Delta y = y - y_a$, and $\Delta z = z - z_a$.

In the evaluation of the integral in Eq. (24), we replaced k with $k+i\gamma$ as suggested in Ref. [14], where γ is a small positive real number. Since there will be some damping of the wave in a physical system, we then complete a contour integral in the complex plane and let γ approach zero.

Changing the integration order of $du\,dv$ and dk, and further letting $w = \operatorname{sgn}(k)\sqrt{k^2-\rho^2}$, Eq. (25) reduces to

$$A_b(x,y,z) = \frac{1}{(2\pi)^3} \int\int\int_{-\infty}^{+\infty} du\,dv\,dw$$
$$\times \exp(-iu\Delta x - iv\Delta y - iw\Delta z)\tilde{H}(k), \quad (26)$$

where $k^2 = u^2 + v^2 + w^2$.

Particularly, if $\tilde{H}(k) \equiv 1$ for $-\infty < k < \infty$, Eq. (26) becomes a point source as the original one in Eq. (20).

In general, by changing the integral from the Cartesian coordinates into the spherical coordinates,

$$(u,v,w) \rightarrow \mathbf{k} = (k,\theta,\varphi),$$

$$(\Delta x, \Delta y, \Delta z) \rightarrow \mathbf{R} = (R,\alpha,\beta),$$

where $R^2 = (\Delta x)^2 + (\Delta y)^2 + (\Delta z)^2$, one can rewrite Eq. (26) as

$$A_b(x,y,z) = \frac{1}{(2\pi)^3} \int\int\int \exp(-i\mathbf{k}\cdot\mathbf{R})\tilde{H}(k)d^3\mathbf{k}. \quad (27)$$

The integration of Eq. (27) can be further simplified to

$$A_b(x,y,z) = \frac{1}{(2\pi)^3} \int_0^{+\infty} \tilde{H}(k)k^2\,dk$$
$$\times \int_0^\pi \exp(-ikR\cos\gamma)\sin\gamma\,d\gamma 2\pi, \quad (28)$$

where γ is the angle between $\mathbf{k}$ and $\mathbf{R}$, i.e.,

$$A_b(x,y,z) = \frac{1}{2\pi^2} \int_0^{+\infty} \tilde{H}(k)j_0(kR)k^2\,dk. \quad (29)$$

C. Cylindrical geometry

The point source at $\mathbf{r}_a = (\rho_a, \varphi_a, z_a)$ in the cylindrical coordinates can be written as

$$A(\rho,\varphi,z) = \frac{1}{\rho}\delta(\rho-\rho_a)\delta(\varphi-\varphi_a)\delta(z-z_a)$$
$$= \frac{1}{\rho}\delta(\rho-\rho_a)\frac{1}{2\pi}\sum_{m=-\infty}^{+\infty}\exp[im(\varphi-\varphi_a)]$$
$$\times \frac{1}{2\pi}\int_{-\infty}^{+\infty}\exp[ik_z(z-z_a)]dk_z. \quad (30)$$

The Green's function can be expanded as $(k>0)$ [11,14,17]

$$\tilde{G}_k(\mathbf{r}_a, \mathbf{r}_0) = \frac{i}{8\pi}\sum_{m=-\infty}^{+\infty}\exp[im(\varphi_a - \varphi_0)]$$
$$\times \int_{-\infty}^{+\infty}dk_z \exp[ik_z(z_a - z_0)]$$
$$\times J_m(\mu\rho_a)H_m^{(1)}(\mu\rho_0), \quad (31)$$

where $\mu = \sqrt{k^2 - k_z^2}$ when $k_z^2 < k^2$, and $\mu = i\sqrt{k_z^2 - k^2}$ when $k_z^2 > k^2$.

Using the detected signal at the recording surface $\mathbf{r}_0$, $\tilde{p}'(\mathbf{r}_0,k) = \tilde{H}(k)\tilde{p}(\mathbf{r}_0,k)$ to replace $\tilde{p}(\mathbf{r}_0,k)$ in the reconstruction Eq. (10), and considering the following identities:

$$\int_0^{2\pi} d\varphi_0 \exp[i\varphi_0(n-m)] = 2\pi\delta_{nm}, \qquad (32)$$

$$\int_{-\infty}^{+\infty} dz_0 \exp[iz_0(\gamma - k_z)] = 2\pi\delta(\gamma - k_z), \qquad (33)$$

the resulting reconstruction for $A(\mathbf{r})$ is

$$A_b(\rho,\varphi,z) = \frac{1}{4\pi^2} \int_0^{+\infty} k\, dk\, \tilde{H}(k) \int_{-k}^{+k} dk_z \exp[ik_z(z_a - z)]$$

$$\times \sum_{m=-\infty}^{+\infty} \exp[im(\varphi_a - \varphi)] J_m(\mu\rho_a) J_m(\mu\rho). \qquad (34)$$

Changing the integration order of variables k and k_z and taking into account the following identity [15]:

$$\sum_{m=-\infty}^{+\infty} \exp[im(\varphi_a - \varphi)] J_m(\mu\rho_a) J_m(\mu\rho) = J_0(\mu D), \qquad (35)$$

where $D = \sqrt{\rho_a^2 + \rho^2 - 2\rho_a\rho\cos(\varphi_a - \varphi)}$, one can simplify Eq. (34) to

$$A_b(\rho,\varphi,z) = \frac{1}{4\pi^2} \int_{-\infty}^{+\infty} dk_z \exp[ik_z(z_a - z)]$$

$$\times \int_{|k_z|}^{+\infty} k\tilde{H}(k) dk\, J_0(\mu D). \qquad (36)$$

By changing the integral variable k with $\mu = \sqrt{k^2 - k_z^2}$, one can get

$$A_b(\rho,\varphi,z) = \frac{1}{4\pi^2} \int_{-\infty}^{+\infty} dk_z \exp[-ik_z\Delta z]$$

$$\times \int_0^{+\infty} \tilde{H}(k)\mu\, d\mu\, J_0(\mu D), \qquad (37)$$

where $k^2 = k_z^2 + \mu^2$, $\Delta z = z - z_a$.

Then, one can denote $\Delta x = x - x_a = D\cos\beta$ and $\Delta y = y - y_a = D\sin\beta$, and introduce $k_x = \mu\cos\alpha$ and $k_y = \mu\sin\alpha$, where $D = \sqrt{(\Delta x)^2 + (\Delta y)^2}$ and $\mu = \sqrt{k_x^2 + k_y^2}$, and rewrite the far right integral in Eq. (37) as

$$\int_0^{+\infty} \mu\, d\mu\, H(k) J_0(\mu D) = \frac{1}{2\pi} \int\int_{-\infty}^{+\infty} dk_x dk_y$$

$$\times \exp(-ik_x\Delta x - ik_x\Delta y)\tilde{H}(k), \qquad (38)$$

where $k^2 = k_z^2 + \mu^2 = k_x^2 + k_y^2 + k_z^2$.

Therefore, Eq. (37) can be rewritten as

$$A_b(\rho,\varphi,z) = \frac{1}{(2\pi)^3} \int\int\int_{-\infty}^{+\infty} dk_z dz_x dk_y \tilde{H}(k)$$

$$\times \exp(-ik_x\Delta x - ik_z\Delta y - ik_z\Delta z), \qquad (39)$$

which is the same as Eq. (26). Thus, $A_b(\rho,\varphi,z)$ takes the same form as Eq. (29),

$$A_b(\rho,\varphi,z) = \frac{1}{2\pi^2} \int_0^{+\infty} \tilde{H}(k) j_0(kR) k^2 dk, \qquad (40)$$

where

$$R = \sqrt{(\Delta x)^2 + (\Delta y)^2 + (\Delta z)^2}$$
$$= \sqrt{\rho_a^2 + \rho^2 - 2\rho_a\rho\cos(\varphi_a - \varphi) + (\Delta z)^2}.$$

Particularly, if $\tilde{H}(k) \equiv 1$ for $k = 0 \to \infty$, Eq. (39) reduces to a point source the same as the original one.

D. General geometry

We have proved that the bandwidth-limited PSF's in the three different geometries share the same expression as shown in Eqs. (17), (29), and (40). As described in these equations, the PSF is independent of the position of the point source but dependent on the distance R from the point source. Therefore, the PSF due to bandwidth is space invariant.

Actually, the space invariance of PSF due to bandwidth can be extended to more general recording geometries. As mentioned in Ref. [11], the reconstruction for $A(\mathbf{r})$ can be expressed by a linear integral:

$$A(\mathbf{r}) = \int\int_{S_0} dS_0 \int_k dk\, \tilde{K}_k(\mathbf{r}_0,\mathbf{r})\tilde{p}(\mathbf{r}_0,k), \qquad (41)$$

where S_0 is the recording surface, which covers the object under study.

The inverse problem for thermoacoustic reconstruction is to seek such an integral kernel $\tilde{K}_k(\mathbf{r}_0,\mathbf{r})$ for a particular recording surface. For the spherical, planar, and cylindrical recording geometries, the integral kernel $\tilde{K}_k(\mathbf{r}_0,\mathbf{r})$ can be explicitly given as shown in Eqs. (8), (9), and (10), respectively. For other recording geometries, the integral kernel $\tilde{K}_k(\mathbf{r}_0,\mathbf{r})$ is more complicated or even nonexistent analytically.

As shown in Fig. 1, suppose another recording surface S_1, which could be a spherical, planar, or cylindrical recording surface, can completely enclose surface S_0. Then, based on Green's theorem [17], the pressure $\tilde{p}(\mathbf{r}_1,k)$ at S_1 can be computed by the pressure $\tilde{p}(\mathbf{r}_0,k)$ on surface S_0,

$$\tilde{p}(\mathbf{r}_1,k) = \int\int_{S_0} dS_0 \Bigg(\tilde{p}(\mathbf{r}_0,k) \frac{\partial \tilde{G}_k(\mathbf{r}_1,\mathbf{r}_0)}{\partial n_0^s}$$

$$- \tilde{G}_k(\mathbf{r}_1,\mathbf{r}_0) \frac{\partial \tilde{p}(\mathbf{r}_0,k)}{\partial n_0^s} \Bigg), \qquad (42)$$

where $\partial/\partial n_0^s$ is the normal component of the gradient on surface S_0 and points outward away from the acoustic source; and $\mathbf{r}_0$ and $\mathbf{r}_1$ represent detection positions on surfaces S_0 and S_1, respectively. Since the reconstruction based on Eq. (41) from the measurement on surface S_0 is exact, the pressure $\bar{p}(\mathbf{r}_1,k)$ on surface S_1 must be identical to the thermoacoustic pressure directly generated by the source $A(\mathbf{r})$:

$$\bar{p}(\mathbf{r}_1,k)=\int\int\int_{V_0}dV_0 A(\mathbf{r})\tilde{G}_k(\mathbf{r}_1,\mathbf{r}), \qquad (43)$$

where V_0 is the volume enclosed by S_0.

Now, considering the bandwidth characterized by $\tilde{H}(k)$, one can rewrite the reconstruction Eq. (41) as

$$A_b(\mathbf{r})=\int\int_{S_0}dS_0\int_{-\infty}^{+\infty}dk\tilde{K}_k(\mathbf{r}_0,\mathbf{r})[\tilde{H}(k)\bar{p}(\mathbf{r}_0,k)]. \qquad (44)$$

In other words, Eq. (44) gives the exact reconstruction of a new and unique source $A_b(\mathbf{r})$ from $\tilde{H}(k)\bar{p}(\mathbf{r}_0,k)$ measured on surface S_0:

$$\tilde{H}(k)\bar{p}(\mathbf{r}_0,k)=\int\int\int_{V_0}dV_0 A_b(\mathbf{r})\tilde{G}_k(\mathbf{r}_0,\mathbf{r}). \qquad (45)$$

Based on Green's theorem, the pressure on surface S_1 can be computed by the pressure $\tilde{H}(k)\bar{p}(\mathbf{r}_0,k)$ on surface S_0, which is found equal to $\tilde{H}(k)\bar{p}(\mathbf{r}_1,k)$ with considering Eq. (42):

$$\int\int_{S_0}dS_0\left([\tilde{H}(k)\bar{p}(\mathbf{r}_0,k)]\frac{\partial\tilde{G}_k(\mathbf{r}_1,\mathbf{r}_0)}{\partial n_0^s}\right.$$
$$\left.-\tilde{G}_k(\mathbf{r}_1,\mathbf{r}_0)\frac{\partial[\tilde{H}(k)\bar{p}(\mathbf{r}_0,k)]}{\partial n_0^s}\right)$$
$$=\tilde{H}(k)\int\int_{S_0}dS_0\left(\bar{p}(\mathbf{r}_0,k)\frac{\partial\tilde{G}_k(\mathbf{r}_1,\mathbf{r}_0)}{\partial n_0^s}\right.$$
$$\left.-\tilde{G}_k(\mathbf{r}_1,\mathbf{r}_0)\frac{\partial\bar{p}(\mathbf{r}_0,k)}{\partial n_0^s}\right)$$
$$=\tilde{H}(k)\bar{p}(\mathbf{r}_1,k). \qquad (46)$$

This pressure must be identical to the thermoacoustic pressure directly generated by the new source $A_b(\mathbf{r})$ in volume V_0,

$$\int\int\int_{V_0}dV_0 A_b(\mathbf{r})\tilde{G}_k(\mathbf{r}_1,\mathbf{r})=\tilde{H}(k)\bar{p}(\mathbf{r}_1,k), \qquad (47)$$

i.e.,

$$\tilde{H}(k)\bar{p}(\mathbf{r}_1,k)=\int\int\int_{V_1}dV_1 A_b(\mathbf{r})\tilde{G}_k(\mathbf{r}_1,\mathbf{r}), \qquad (48)$$

since there is no source in the volume between the surfaces S_0 and S_1.

Equation (48) indicates that the new source $A_b(\mathbf{r})$ could be restored from the value $\tilde{H}(k)\bar{p}(\mathbf{r}_1,k)$ on surface S_1, if an exact reconstruction from data only on surface S_1 does exist. In other words, the reconstruction for $A(\mathbf{r})$ from the measurement with the bandwidth $\tilde{H}(k)$ on surface S_0 is identical to the reconstruction from the measurement with the same bandwidth $\tilde{H}(k)$ on surface S_1 that fully encloses S_0. Fortunately, we have already obtained the exact reconstruction formulas from measurements on such a surface S_1 as the spherical, planar, or cylindrical recording geometries. Therefore, the PSF of the point source at $\mathbf{r}_a$ as a function of bandwidth $\tilde{H}(k)$ from the measurement on surface S_0 is nothing but the same expression as Eqs. (17), (29), and (40) for the above three specific recording geometries, respectively.

E. Resolution

For convenience, we can denote the PSF symbolically as $\mathcal{F}_b^{\mathrm{PSF}}$,

$$\mathcal{F}_b^{\mathrm{PSF}}(R)=\frac{1}{2\pi^2}\int_0^{+\infty}\tilde{H}(k)j_0(kR)k^2 dk, \qquad (49)$$

where the subscript b represents bandwidth, and $R=|\mathbf{r}-\mathbf{r}_a|$. Equation (49) can be rewritten in another form as

$$\mathcal{F}_b^{\mathrm{SPF}}(R)=\frac{-1}{4\pi R}\left[\frac{dH(R)}{dR}+\frac{dH(-R)}{dR}\right], \qquad (50)$$

if we let $H(-\bar{t})=H(\bar{t})$ and define the following Fourier transform:

$$H(\bar{t})=\frac{1}{2\pi}\int_{-\infty}^{+\infty}\tilde{H}(k)\exp(-ik\bar{t})dk, \qquad (51)$$

where $H(\bar{t})$ is the corresponding temporal signal of $\tilde{H}(k)$.

If $\tilde{H}(k)$ has a cutoff frequency k_c, $\tilde{H}(k)=1$ when $k\leqslant k_c$, $\tilde{H}(k)=0$ when $k>k_c$, the integral in Eq. (49) can be carried out,

$$\mathcal{F}_b^{\mathrm{PSF}}(R)=\frac{1}{2\pi^2}\int_0^{k_c}j_0(kR)k^2 dk$$
$$=\frac{k_c}{2\pi^2 R^2}\left(\frac{\sin(k_cR)}{k_cR}-\cos(k_cR)\right), \qquad (52)$$

i.e.,

$$\mathcal{F}_b^{\mathrm{PSF}}(R)=\frac{k_c^3}{2\pi^2}\frac{j_1(k_cR)}{k_cR}=\frac{k_c^3}{6\pi^2}\frac{3j_1(k_cR)}{k_cR}. \qquad (53)$$

By normalizing the PSF of Eq. (53), one can get

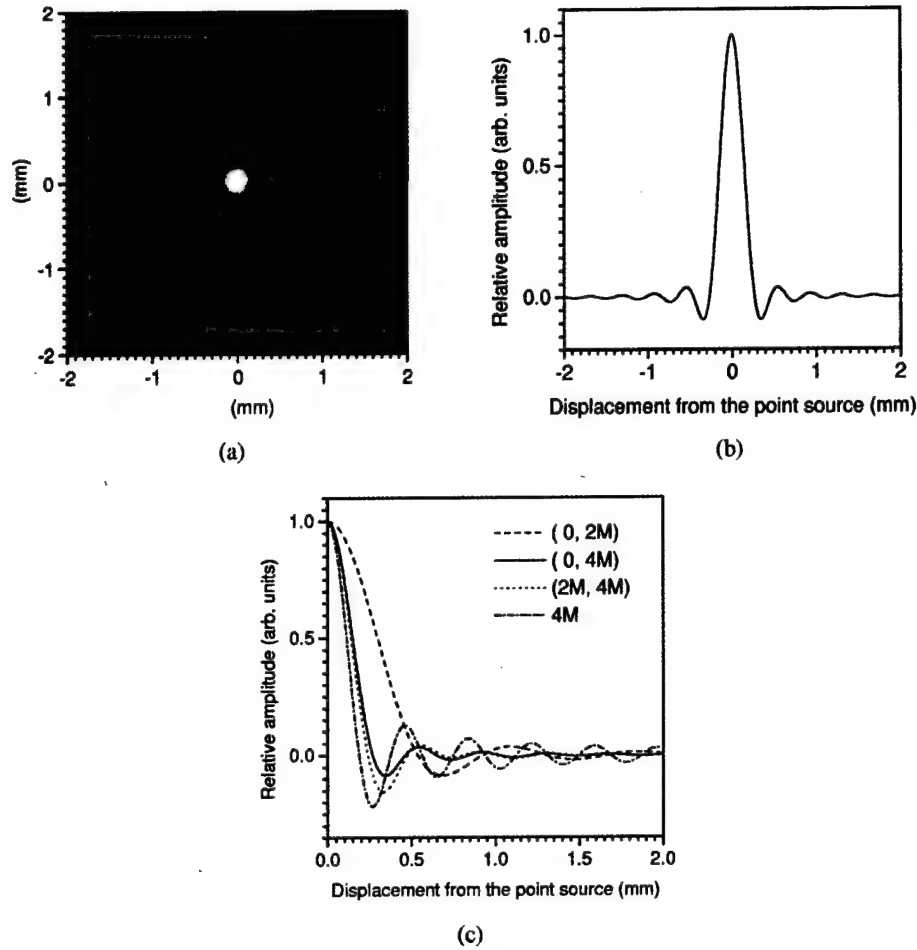$$\mathcal{F}_b^{\mathrm{PSF}}(R)=\frac{3j_1(k_cR)}{k_cR}. \qquad (54)$$

(a)

(b)

(c)

FIG. 2. An example of the PSF as a result of the bandwidth (0, 4 MHz): (a) a gray scale view and (b) a profile through the point source. (c) Comparison of the PSF's with different bandwidths: dashed line, (0, 2 MHz); solid line, (0, 4 MHz); dotted line, (2 MHz, 4 MHz); dot-dashed line, 4 MHz.

The full width at half maximum (FWHM) of the PSF is often used to represent the spatial resolution. It is easy to show $3j_1(x)/x = 0.5$ when $x = 2.4983$. Therefore,

$$W_{\text{FWHM}} = 2 \times \frac{2.4983}{k_c} = 2 \times \frac{2.4983}{2\pi f_c/c} = 0.7952c/f_c \approx 0.8\lambda_c, \tag{55}$$

where λ_c is the wavelength at the cutoff frequency of the bandwidth. For example, if $c = 1.5$ mm/μs, $f_c = 4$ MHz, then $W_{\text{FWHM}} \approx 0.3$ mm. The corresponding $\mathcal{F}_b^{\text{PSF}}(R)$ is plotted in Figs. 2(a) and 2(b).

Sometimes, a detection system has a finite bandwidth characterized by a central frequency f_0 with a low cutoff frequency f_{Lc} and a high cutoff frequency f_{Hc}. For simplicity, suppose $\tilde{H}(k) = 1$ is in the above frequency range, and then the PSF can be expressed by

$$\mathcal{F}_b^{\text{PSF}}(R) = \frac{k_{\text{Hc}}^3}{2\pi^2} \frac{j_1(k_{\text{Hc}}R)}{k_{\text{Hc}}R} - \frac{k_{\text{Lc}}^3}{2\pi^2} \frac{j_1(k_{\text{Lc}}R)}{k_{\text{Lc}}R}, \tag{56}$$

where $k_{\text{Lc}} = 2\pi f_{\text{Lc}}/c$ and $k_{\text{Hc}} = 2\pi f_{\text{Hc}}/c$.

For example, a system is with $f_0 = 3$ MHz, and $f_{\text{Lc}} = 2$ MHz and $f_{\text{Hc}} = 4$ MHz. The corresponding PSF is plotted as the dotted line in Fig. 2(c). As shown in Fig. 2(c), the FWHM of the PSF with a bandwidth of (2 MHz, 4 MHz) is slightly narrower than the FWHM of the PSF with a wider bandwidth of (0, 4 MHz) [solid line in Fig. 2(c)]. In other words, due to the absence of a low frequency component, the high frequency component will cause the FWHM to be narrower. The minimum value of the FWHM can be estimated in the PSF with a single frequency f_c and zero bandwidth. The PSF in this case is nothing but the integral kernel in Eq. (49): the zero-order spherical Bessel function $j_0(k_cR)$. Such an example, with $f_c = 4$ MHz, is plotted as the dash-dot line in Fig. 2(c). Since $j_0(1.895) \approx 0.5$, the minimum $W_{\text{FWHM}} \approx 0.6\lambda_c$, where λ_c is the wavelength at the cutoff frequency f_c. But, as shown in Fig. 2(c), a PSF that lacks a low frequency component does not concentrate in the center beam anymore, and the side beams of the PSF slowly attenuate as the position gets farther away from the point source, thereby introducing significant artifacts in the investigation of large objects.
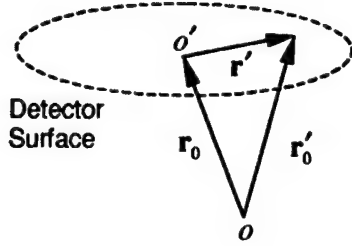
FIG. 3. Diagram of the detector surface $\mathbf{r}'$ with origin o'. The vector $\mathbf{r}_0$ represents the center of detector o' in the recording geometry with origin o. The vector $\mathbf{r}_0'$ points to an element of the detector aperture.

In conclusion, the obtainable spatial resolution approximates to a value between $0.6\lambda_c$ and $0.8\lambda_c$, where λ_c is the wavelength at the high cutoff frequency f_c. If the bandwidth is too narrow, the reconstruction based on the wide bandwidth measurement becomes inappropriate and the FWHM of the reconstructed PSF does not properly describe the real spatial resolution.

IV. EFFECT OF DETECTOR APERTURE

Next, let us derive the analytic expressions of the PSF's related to detector aperture size. As shown in Fig. 3, the real signal detected at position $\mathbf{r}_0$ can be expressed as a surface integral over the detector aperture

$$\tilde{p}'(\mathbf{r}_0,k) = \int \int \tilde{p}(\mathbf{r}_0',k)W(\mathbf{r}_0')d^2\mathbf{r}_0', \qquad (57)$$

where $W(\mathbf{r}_0')$ is a weighting factor, which represents the contribution from different elements of the detector surface to the total signal of the detector.

Since $\mathbf{r}_0' = \mathbf{r}_0 + \mathbf{r}'$, Eq. (57) can be rewritten as

$$\tilde{p}'(\mathbf{r}_0,k) = \int \int \tilde{p}(\mathbf{r}_0 + \mathbf{r}',k)W(\mathbf{r}')d^2\mathbf{r}'. \qquad (58)$$

One can assume a point source at $\mathbf{r}_a$ and then get the detected signal at position $\mathbf{r}_0$ using Eq. (57) or (58). If the signal is not bandlimited, by substituting $\tilde{p}'(\mathbf{r}_0,k)$ for $p(\mathbf{r}_0,k)$ in the rigorous reconstruction formulas such as Eqs. (8)–(10), one can get analytic expressions of the PSF's for the spherical, planar, and cylindrical geometries, respectively. In general, the analytic expressions cannot be thoroughly simplified for arbitrary detector apertures. In order to explicitly demonstrate the effects of the detector apertures on spatial resolution, we will make some assumptions about the detector apertures.

A. Spherical geometry

As shown in Fig. 4(a), $\mathbf{r}_0$ represents the center of detector o' in the global spherical coordinates (r,θ,φ) with the origin at the recording geometry center o. A local spherical coordinate system aligned with $\mathbf{r}_0$ is used as well. Assume that the detector is circularly symmetric about its center o'; in this case, the weighting factor depends only on θ', $W(\mathbf{r}')$
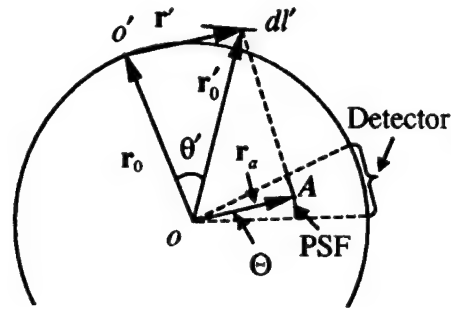
(a)

(b)

FIG. 4. (a) Diagram of the spherical recording geometry: θ' is the angle between $\mathbf{r}_0$ and $\mathbf{r}_0'$; dl' is an integral element on the detector surface; Θ is the angle of the radius of the detector aperture to the recording geometry origin o; the extension of the PSF at point A is indicated; other denotations of the symbols are the same as in Figs. 1 and 3. (b) Perspective view of the lateral extension of the PSF's of all the point sources along a radial axis in the spherical recording geometry.

$= W(\theta')$, where the angle θ' between $\mathbf{r}_0'$ and $\mathbf{r}_0$—the polar angle of $\mathbf{r}_0'$ in the local coordinate system—varies from 0 to Θ depending on the size of the detector. The azimuthal angle φ' of $\mathbf{r}_0'$ in the local coordinate system varies from 0 to 2π. The normal of the detector surface at point o' is assumed to point to the center of the recording geometry o. The surface integral in Eq. (58) can be transformed into an integral over a curve radiating from the center o' on the surface l' and the azimuthal angle φ':

$$\tilde{p}'(\mathbf{r}_0,k) = \int \int \tilde{p}(\mathbf{r}_0+\mathbf{r}',k)W(\theta')r'\sqrt{1-(\mathbf{n}_0\cdot\mathbf{n}')^2}d\varphi'dl'$$

$$= \int_{l'} W(\theta')\sqrt{1-(\mathbf{n}_0\cdot\mathbf{n}')^2}r'dl'$$

$$\times \int_0^{2\pi} \tilde{p}(\mathbf{r}_0+\mathbf{r}',k)d\varphi', \qquad (59)$$

where $\mathbf{n}'=\mathbf{r}'/r'$ and

$$\tilde{p}(\mathbf{r}_0+\mathbf{r}',k)=-ikc^2\eta\frac{\exp(ik|\mathbf{r}_a-\mathbf{r}_0-\mathbf{r}'|)}{4\pi|\mathbf{r}_a-\mathbf{r}_0-\mathbf{r}'|}. \quad (60)$$

Considering the expansion in the local spherical coordinates, and denoting $\mathbf{n}'_0=\mathbf{r}'_0/r'_0$, $\mathbf{n}'_0=(\theta',\varphi')$, and $\mathbf{n}_a=(\theta'_a,\varphi'_a)$, one obtains

$$\frac{\exp(ik|\mathbf{r}_a-\mathbf{r}'_0|)}{4\pi|\mathbf{r}_a-\mathbf{r}'_0|}=\frac{ik}{4\pi}\sum_{l=0}^{\infty}(2l+1)j_l(kr_a)$$

$$\times h_l^{(1)}(kr'_0)P_l(\mathbf{n}_a\cdot\mathbf{n}'_0), \quad (61)$$

where $P_l(\mathbf{n}_a\cdot\mathbf{n}'_0)$ can be expanded as [14]

$$P_l(\mathbf{n}_a\cdot\mathbf{n}'_0)=P_l(\cos\theta'_a)P_l(\cos\theta')$$

$$+2\sum_{m=1}^{l}\frac{(l-m)!}{(l+m)!}P_l^m(\cos\theta'_a)P_l^m(\cos\theta')$$

$$\times\cos[m(\varphi'_a-\varphi')]. \quad (62)$$

Then, one can evaluate the following integral:

$$\int_0^{2\pi}P_l(\mathbf{n}_a\cdot\mathbf{n}'_0)d\varphi'=2\pi P_l(\cos\theta')P_l(\cos\theta'_a). \quad (63)$$

Actually, θ'_a is the angle between $\mathbf{r}_0$ and $\mathbf{r}_a$, i.e., $\cos\theta'_a=\mathbf{n}_a\cdot\mathbf{n}_0$.

Combining the results of Eqs. (61)–(63), Eq. (59) can be rewritten as

$$\tilde{p}'(\mathbf{r}_0,k)=\frac{k^2c^2\eta}{2}\int_{l'}W(\theta')\sqrt{1-(\mathbf{n}_0\cdot\mathbf{n}')^2}r'dl'$$

$$\times\sum_{l=0}^{\infty}(2l+1)P_l(\cos\theta')P_l(\mathbf{n}_a\cdot\mathbf{n}_0)j_l(kr_a)$$

$$\times h_l^{(1)}(kr'_0). \quad (64)$$

By replacing $p(\mathbf{r}_0,k)$ with $\tilde{p}'(\mathbf{r}_0,k)$ in the reconstruction formula Eq. (8) and considering identity (14), one obtains the reconstruction for $A(\mathbf{r})$:

$$A_a(\mathbf{r})=\frac{1}{\pi}\int_{l'}W(\theta')\sqrt{1-(\mathbf{n}_0\cdot\mathbf{n}')^2}r'dl'$$

$$\times\sum_{m=0}^{\infty}(2m+1)P_m(\mathbf{n}_a\cdot\mathbf{n})P_m(\cos\theta')$$

$$\times\int_0^{+\infty}j_m(kr_a)j_m(kr)\frac{h_m^{(1)}(kr'_0)}{h_m^{(1)}(kr_0)}k^2dk. \quad (65)$$

Letting $\tilde{\theta}$ and $\tilde{\varphi}$ be the polar and azimuthal angles of vector $\mathbf{n}$ with respect to vector $\mathbf{n}_a$, and using an identity similar to the one shown in Eq. (63), one can rewrite Eq. (65) as

$$A_a(\mathbf{r})=\int\int W(\theta')r'\sqrt{1-(\mathbf{n}_0\cdot\mathbf{n}')^2}d\varphi'dl'$$

$$\times\frac{1}{2\pi^2}\sum_{m=0}^{\infty}(2m+1)P_m(\cos\tilde{\gamma})$$

$$\times\int_0^{+\infty}j_m(kr_a)j_m(kr)\frac{h_m^{(1)}(kr'_0)}{h_m^{(1)}(kr_0)}k^2dk, \quad (66)$$

where $\cos\tilde{\gamma}=\cos\tilde{\theta}\cos\theta'+\sin\tilde{\theta}\sin\theta'\cos(\tilde{\varphi}-\varphi')$.

1. Special spherical aperture

For simplicity, assume that the detector is a small section of the spherical measurement surface, i.e., $r'_0=|\mathbf{r}'_0|=|\mathbf{r}_0+\mathbf{r}'|=|\mathbf{r}_0|=r_0$. Therefore, one obtains

$$\sqrt{1-(\mathbf{n}_0\cdot\mathbf{n}')^2}r'dl'=r_0^2\sin\theta'd\theta', \quad (67)$$

and

$$h_m^{(1)}(kr'_0)/h_m^{(1)}(kr_0)=1. \quad (68)$$

Substituting the identity Eq. (18) and the following identity (see the Appendix) into Eq. (65),

$$\sum_{m=0}^{\infty}(2m+1)P_m(\mathbf{n}_a\cdot\mathbf{n})P_m(\cos\theta')=2\delta(\cos\theta'-\mathbf{n}_a\cdot\mathbf{n}),$$

$$(69)$$

one obtains

$$A_a(\mathbf{r})=\frac{r_0^2}{r^2}\delta(r-r_a)\int_0^{\Theta}\sin\theta'W(\theta')d\theta'\,\delta(\cos\theta'-\mathbf{n}_a\cdot\mathbf{n}).$$

$$(70)$$

Letting γ be the angle between $\mathbf{n}_a$ and $\mathbf{n}$, i.e., $\mathbf{n}_a\cdot\mathbf{n}=\cos\gamma$,

$$A_a(\mathbf{r})=\frac{r_0^2}{r^2}\delta(r-r_a)\int_0^{\Theta}\sin\theta'W(\theta')d\theta'\,\delta(\cos\theta'-\cos\gamma)$$

$$=\frac{r_0^2}{r^2}\delta(r-r_a)\int_0^{\Theta}\sin\theta'W(\theta')d\theta'\frac{\delta(\theta'-\gamma)}{\sin\theta'}$$

$$=\frac{r_0^2}{r^2}\delta(r-r_a)\int_0^{\Theta}W(\theta')\delta(\theta'-\gamma)\delta\theta'$$

$$=\frac{r_0^2}{r^2}\delta(r-r_a)W(\gamma). \quad (71)$$

If letting $W(\theta')=1$,

$$A_a(\mathbf{r})=\frac{r_0^2}{r^2}\delta(r-r_a)[U(\gamma)-U(\gamma-\Theta)], \quad (72)$$

where U is the step function, $U(x)=1$ when $x>0$ and $U(x)=0$ when $x<0$.

Equation (72) indicates that, in this special case, the PSF only extends along the lateral direction, which is proportional to the solid angle of the detector aperture to the origin

of the measurement geometry. The perspective view of the lateral extension of all the points in a radial axis looks like a cone as shown in Fig. 4(b). The farther the point source is away from the origin, the more extension the PSF has. Therefore, the lateral resolution is worse when the point is close to the detector. But, a lateral resolution superior to the aperture size can still be achieved if the object under study is close to the center of the geometry.

2. Small flat aperture

Now, let us consider flat apertures. Sometimes, a set of small flat detectors is used to form a spherical recording surface. Suppose the detector aperture is disklike and its radius is P. Since $\mathbf{n}_0 \cdot \mathbf{n}' = 0$ in this case,

$$\sqrt{1 - (\mathbf{n}_0 \cdot \mathbf{n}')^2} \, r' \, dl' = r' \, dr', \tag{73}$$

where $r' = r_0 \tan \theta'$. If the aperture is small relative to the radius of the detection surface, i.e., $r' \leqslant P \ll r_0$, the following approximation holds:

$$r_0' - r_0 = \sqrt{r_0^2 + r'^2} - r_0 \approx \frac{r'^2}{2r_0}. \tag{74}$$

Neglecting the second-order and higher small quantities, one can approximate $h_m^{(1)}(kr_0')/h_m^{(1)}(kr_0) \approx 1$. Then, one can follow the derivation for the special spherical aperture and obtain

$$A_a(\mathbf{r}) = \frac{1}{r^2} \delta(r - r_a) \int_0^P W(r') r' \, dr' \, \delta(\cos \theta' - \mathbf{n}_a \cdot \mathbf{n}). \tag{75}$$

Letting $W(r') = 1$ and approximating $r' = r_0 \tan \theta' \approx r_0 \theta'$ for the small-aperture case, one reaches

$$
\begin{aligned}
A_a(\mathbf{r}) &\approx \frac{r_0^2}{r^2} \delta(r - r_a) \int_0^{P/r_0} \theta' \frac{\delta(\theta' - \gamma)}{\sin \theta'} d\theta' \\
&= \frac{r_0^2}{r^2} \delta(r - r_a) \int_0^{P/r_0} \delta(\theta' - \gamma) \delta\theta' \\
&= \frac{r_0^2}{r^2} \delta(r - r_a)[U(\gamma) - U(\gamma - P/r_0)].
\end{aligned}
\tag{76}
$$

Equation (76) indicates that, for the small flat aperture, the extension of the PSF is primarily along the lateral axis. In fact, if we substitute Θ for P/r_0, Eq. (76) becomes identical to Eq. (72) for the special spherical aperture.

Particularly, at the center of the recording geometry, i.e., $r_a = 0$, we have $j_m(0) = \delta_{m0}$, $P_0(\cdot) = 1$, and $h_0^{(1)}(kr) = -i \exp(ikr)/(kr)$. Assuming $W(r') = 1$, Eq. (65) reduces to

$$
\begin{aligned}
A_a(\mathbf{r}) &= \frac{1}{\pi} \int_0^{+\infty} j_0(kr) \exp(-ikr_0) k^2 dk \\
&\quad \times \int_0^P \frac{r_0}{r_0'} r' \, dr' \exp(ikr_0').
\end{aligned}
\tag{77}
$$

Using the relation $r_0' = \sqrt{r_0^2 + r'^2}$, one can simplify Eq. (77) to

$$A_a(\mathbf{r}) = \frac{1}{\pi} \int_0^{+\infty} j_0(kr) k^2 dk \frac{r_0[\exp(ik\sqrt{P^2 + r_0^2} - ikr_0) - 1]}{ik}. \tag{78}$$

Because $P \ll r_0$, the imaginary part is much less than the real part and hence can be neglected; as a result, one can obtain

$$A_a(\mathbf{r}) \approx \frac{r_0}{\pi} \int_0^{+\infty} j_0(kr) \sin[k(\sqrt{P^2 + r_0^2} - r_0)] k \, dk. \tag{79}$$

Using the following identity [14]:

$$
\begin{aligned}
\int_0^{+\infty} j_0(ka) \sin(kb) k \, dk &= b \int_0^{+\infty} j_0(ka) j_0(kb) k^2 dk \\
&= \frac{\pi}{2b} \delta(b - a),
\end{aligned}
\tag{80}
$$

in the small-aperture case, i.e., $P \ll r_0$, Eq. (79) reduces to

$$A_a(r) = \frac{r_0^2}{P^2} \delta\left(r - \frac{P^2}{2r_0}\right). \tag{81}$$

Equation (79) indicates that the point source at the center becomes a circle with a diameter P^2/r_0.

Next, we want to estimate the lateral extension at an arbitrary point. Taking the asymptotic form of the Hankel function to approximate

$$\frac{h_m^{(1)}(kr_0')}{h_m^{(1)}(kr_0)} \approx \frac{\exp(ikr_0')/(kr_0')}{\exp(ikr_0)/(kr_0)} = \frac{r_0}{r_0'} \exp(ikr_0' - ikr_0), \tag{82}$$

one can rewrite Eq. (65) as

$$
\begin{aligned}
A_a(\mathbf{r}) &= \frac{1}{\pi} \int_0^P W(r') r' \, dr' \int_0^{+\infty} \frac{r_0}{r_0'} \exp(ikr_0' - ikr_0) k^2 dk \\
&\quad \times \sum_{m=0}^{\infty} (2m+1) P_m(\mathbf{n}_a \cdot \mathbf{n}) \\
&\quad \times P_m(\cos \theta') j_m(kr_a) j_m(kr).
\end{aligned}
\tag{83}
$$

The above integral is still complicated. Here, we consider only the spread along $\mathbf{r}_a$ with the assumption of $W(r') = 1$. Substituting $P_m(\mathbf{n}_a \cdot \mathbf{n}) = P_m(1) = 1$ into Eq. (83) and considering identity (16), and further approximating $j_0(k\sqrt{r_a^2 + r^2 - 2r_a r \cos \theta'}) \approx j_0(k|r - r_a|)$ for the small-aperture case $(r' \ll r_0$, i.e., $\theta' \ll 1)$, one obtains

$$
\begin{aligned}
A_a(r\mathbf{n}_a) &= \frac{1}{\pi} \int_0^{+\infty} j_0(k|r - r_a|) \exp(-ikr_0) k^2 dk \\
&\quad \times \int_0^P \frac{r_0}{r_0'} r' \, dr' \exp(ikr_0').
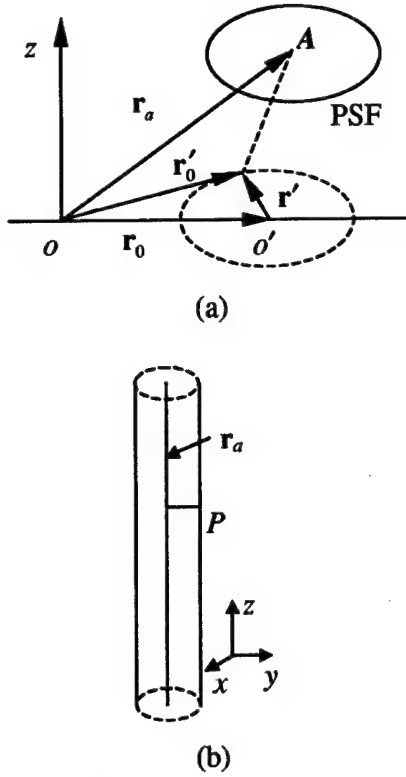\end{aligned}
\tag{84}
$$

(a)

(b)

FIG. 5. (a) Diagram of the planar recording geometry: P is the radius of the detector aperture; the extension of the PSF at point A is indicated; other denotations of the symbols are the same as in Figs. 1 and 3; (b) perspective view of the lateral extension of the PSF's of all the point sources along a line parallel to the z axis in the planar recording geometry.

If we substitute $|r-r_a|$ for r, Eq. (84) becomes identical to Eq. (77). Thus, in the small-aperture case ($P \ll r_0$), Eq. (84) reduces to Eq. (81) with the replacement of r by $|r-r_a|$:

$$A_a(r\mathbf{n}_a) \approx \frac{r_0^2}{P^2} \delta\left(|r-r_a| - \frac{P^2}{2r_0} \right). \quad (85)$$

Equation (85) indicates that the point source at which $\mathbf{r}_a$ extends in the radial direction to a region with diameter P^2/r_0 is the same as the extension of the PSF at the recording geometry center as shown in Eq. (81). But, in most cases, this extension is negligible. For example, when using a transducer with even a 6 mm diameter to image a 10-cm-size breast on a recording geometry surface with a 15 cm diameter, $P^2/r_0 = 3^2/150 = 0.06$ mm. However, the lateral extension at r is on the order of $2rP/r_0$ as shown in Eq. (76). For example, even at $r=1$ cm, $2rP/r_0 = (2)(10)(3)/150 = 0.4$ mm > 0.06 mm.

B. Planar geometry

In this case, we reasonably assume that the detector surface is flat. As shown in Fig. 5(a), $\mathbf{r}_0$ represents the center of the detector o' in the global Cartesian coordinates (x, y, z) with the origin at the recording geometry center o. Let x',

y', and z' be the differences of the coordinates between $\mathbf{r}_0'$ and $\mathbf{r}_0$, respectively. For the following two linear translations:

$$\mathbf{r}_0 \rightarrow \mathbf{r}_0': \quad x_0 \rightarrow x_0 + x' = x_0', \quad y_0 \rightarrow y_0 + y' = y_0', \quad (86)$$

$$\mathbf{r}_a \rightarrow \mathbf{r}_a': \quad x_a \rightarrow x_a - x' = x_a', \quad y_a \rightarrow y_a - y' = y_a', \quad (87)$$

there exist the following translational invariances, $|\mathbf{r}_a - \mathbf{r}_0'| = |\mathbf{r}_a' - \mathbf{r}_0|$.

The detected signal at $\mathbf{r}_0$ can be written as

$$\bar{p}'(\mathbf{r}_0, k) = \int \int W(\mathbf{r}') \bar{p}(\mathbf{r}_0 + \mathbf{r}', k) d^2 \mathbf{r}'$$

$$= \int \int W(x', y') \bar{p}(x_0 + x', y_0 + y', k) dx' dy'. \quad (88)$$

Using $\bar{p}'(\mathbf{r}_0, k)$ to replace $p(\mathbf{r}_0, k)$ in the reconstruction formula Eq. (9), and following the similar derivation shown in Sec. III B, one gets the reconstruction for $A(\mathbf{r})$ as

$$A_a(x, y, z) = \int \int W(x', y') \delta(x - x_a') \delta(y - y_a')$$

$$\times \delta(z - z_a) dx' dy'$$

$$= \int \int W(x', y') \delta(x - x_a + x') \delta(y - y_a + y')$$

$$\times \delta(z - z_a) dx' dy', \quad (89)$$

i.e.,

$$A_a(x, y, z) = W(x - x_a, y - y_a) \delta(z - z_a). \quad (90)$$

Assuming that the detector surface is a disk with radius P, and $W(x', y') = 1$ when $\sqrt{x'^2 + y'^2} < P$, Eq. (90) reduces to

$$A_a(x, y, z) = U(P - D) \delta(\Delta z), \quad (91)$$

where $D = \sqrt{(\Delta x)^2 + (\Delta y)^2}$, and $\Delta x = x - x_a$, etc.

Equation (91) indicates that without considering the bandwidth, the PSF does not extend along the axial direction, but it greatly extends in the lateral direction. Moreover, the lateral extension is proportional to the detector aperture. The perspective view of the lateral extension of all the PSF's in a line parallel with the z axis looks like a cylinder as shown in Fig. 5(b). Therefore, the lateral resolution is totally blurred by the detector aperture, no matter where the point is.

C. Cylindrical geometry

1. Special cylinder aperture

We first assume that the detector surface is a section of the cylindrical measurement surface. As shown in Fig. 6(a), $\mathbf{r}_0$ represents the center of the detector o' in the global cylindrical coordinates (ρ, φ, z) with the origin at the recording geometry center o. Let φ' be the difference between the polar angles of $\mathbf{r}_0$ and $\mathbf{r}_0'$, and ρ' and z' be the projections of
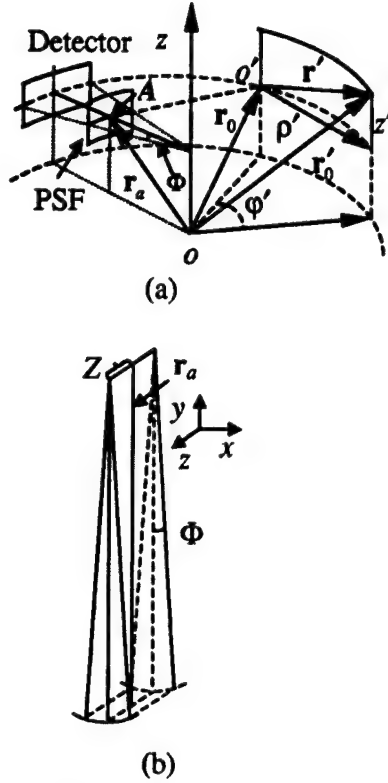
FIG. 6. (a) Diagram of the cylindrical geometry: φ' is the difference between the polar angles of r_0 and r_0'; ρ' and z' are the projections of $\mathbf{r}'$ in the x-y plane and the z axis, respectively; Z is the half width of the detector aperture along the z axis and Φ is the half angle of the width of the detector aperture parallel to the x-y plane to the center of the recording geometry; the extension of the PSF at point A is indicated; other denotations of the symbols are the same as in Figs. 1 and 3. (b) Perspective view of the lateral extension of the PSF's of all the point sources along a radial axis in the cylindrical recording geometry.

$\mathbf{r}'$ in the x-y plane and the z axis, respectively. Two sides of the detector are along the z axis from $-Z$ to Z, and the other two sides are parallel with the x-y plane and the polar angle φ' varies from $-\Phi$ to Φ. For the following two translations:

$$\mathbf{r}_0 \rightarrow \mathbf{r}_0': \quad \varphi_0 \rightarrow \varphi_0 + \varphi' = \varphi_0', \quad z_0 \rightarrow z_0 + z' = z_0', \quad (92)$$

$$\mathbf{r}_a \rightarrow \mathbf{r}_a': \quad \varphi_a \rightarrow \varphi_a - \varphi' = \varphi_a', \quad z_a \rightarrow z_a - z' = z_a', \quad (93)$$

there exist the following translational invariances, $|\mathbf{r}_a - \mathbf{r}_0'| = |\mathbf{r}_a' - \mathbf{r}_0|$.

The detected signal can be written as

$$\tilde{p}_a(\mathbf{r}_0, k) = \int \int \tilde{p}(\mathbf{r}_0 + \mathbf{r}', k) W(\mathbf{r}') d^2 \mathbf{r}'$$

$$= \int \int \tilde{p}(\varphi_0 + \varphi', z_0 + z', k) W(\varphi', z') \rho_0 d\varphi' dz'.$$

$$(94)$$

Replacing $p(\mathbf{r}_0, k)$ by $\tilde{p}'(\mathbf{r}_0, k)$ in the reconstruction formula Eq. (10), and following the derivation shown in Sec. III C, one can get the reconstruction for $A(\mathbf{r})$ as

$$A_a(\rho, \varphi, z) = \int \int \frac{1}{\rho} \delta(\rho - \rho_a) \delta(\varphi - \varphi_a')$$

$$\times \delta(z - z_a') W(\varphi', z') \rho_0 d\varphi' dz'$$

$$= \frac{\rho_0}{\rho} \delta(\rho - \rho_a) \int \int \delta(\varphi - \varphi_a + \varphi')$$

$$\times \delta(z - z_a + z') W(\varphi', z') d\varphi' dz', \quad (95)$$

i.e.,

$$A_a(\rho, \varphi, z) = \frac{\rho_0}{\rho} \delta(\rho - \rho_a) W(\varphi - \varphi_a, z - z_a). \quad (96)$$

If $W(\varphi', z') = 1$, φ' from $-\Phi$ to Φ, and z' from $-Z$ to Z, Eq. (96) can be rewritten as

$$A_a(\rho, \varphi, z) = \frac{\rho_0}{\rho} \delta(\rho - \rho_a) U(\Phi - |\varphi - \varphi_a|) U(Z - |z - z_a|). \quad (97)$$

Equation (97) indicates that the extension of the PSF in the cylindrical geometry combines the properties of the PSF's in the spherical and planar geometries. In this special case, the PSF does not extend along the radial direction. The perspective view of the lateral extension of all the point sources in a radial axis looks like a wedge of pie as shown in Fig. 6(b). In the z-axis direction, the PSF extension is proportional to the detector size along the z axis, just like the planar geometry. While parallel with the x-y plane, the lateral extension is proportional to the angle of the detector width to the z axis, just like in the spherical case. Therefore, a lateral resolution that is better than the aperture size can be obtained parallel to the x-y plane if the object under study is close to the center of the geometry; however, the lateral resolution along the z axis is determined by the detector size.

2. Small rectangle aperture

Sometimes a set of small rectangle detectors is used to form a cylindrical array. The normal of the detector at the center point o' is assumed to point to the center of the recording geometry. Two sides of the detector are along the z axis from $-Z$ to Z, and the other two sides are parallel with the x-y plane and have a length of $2P$. One can follow the similar derivation in Sec. III C, and get the reconstruction for $A(\mathbf{r})$ as

$$A_a(\rho,\varphi,z) = \frac{1}{2\pi} \int_{-Z}^{Z} \delta(z_a - z - z') dz' \int_{-P}^{P} d\rho' \, W(\varphi', z')$$

$$\times \sum_{m=-\infty}^{+\infty} \exp[im(\varphi_a - \varphi - \varphi')]$$

$$\times \int_{0}^{+\infty} \mu \, d\mu$$

$$\times J_m(\mu\rho_a) J_m(\mu\rho) \frac{H_m^{(1)}(\mu\sqrt{\rho_0^2 + \rho'^2})}{H_m^{(1)}(\mu\rho_0)}, \quad (98)$$

where $\rho' = \rho_0 \tan\varphi'$. Let $W(\varphi', z') = 1$.

For the small-aperture case, $\rho' \ll \rho_0$, one can approximate

$$\frac{H_m^{(1)}(\mu\sqrt{\rho_0^2 + \rho'^2})}{H_m^{(1)}(\mu\rho_0)} \approx 1. \quad (99)$$

Further, taking the small-aperture approximation $\rho' = \rho_0 \tan\varphi' \simeq \rho_0\varphi'$, and considering the following identity [14]:

$$\int_{0}^{+\infty} \mu \, d\mu \, J_m(\mu\rho_a) J_m(\mu\rho) = \frac{1}{\rho} \delta(\rho - \rho_a), \quad (100)$$

one can rewrite Eq. (98) as

$$A_a(\rho,\varphi,z) = U(Z - |z - z_a|) \frac{1}{\rho} \delta(\rho - \rho_a)$$

$$\times \int_{-P/\rho_0}^{P/\rho_0} \rho_0 d\varphi' \, \delta(\varphi_a - \varphi - \varphi'), \quad (101)$$

i.e.,

$$A_a(\rho,\varphi,z) = \frac{\rho_0}{\rho} \delta(\rho - \rho_a) U\left(\frac{P}{\rho_0} - |\varphi - \varphi_a|\right) U(Z - |z - z_a|). \quad (102)$$

Equation (102) indicates that, for the small flat aperture, the extension of the PSF is primarily along the lateral axis. In fact, if we substitute Φ for P/ρ_0, Eq. (102) becomes identical to Eq. (97) in the special cylinder aperture case.

Next, we want to estimate the lateral extension of the PSF. One can also take the asymptotic form of the Hankel function to approximate

$$\frac{H_m^{(1)}(\mu\sqrt{\rho_0^2 + \rho'^2})}{H_m^{(1)}(\mu\rho_0)} \approx \exp[i\mu(\sqrt{\rho_0^2 + \rho'^2} - \rho_0)], \quad (103)$$

and then rewrite Eq. (98) as

$$A_a(\rho,\varphi,z) = \frac{1}{2\pi} U(Z - |z - z_a|) \int_{0}^{+\infty} \mu \, d\mu$$

$$\times \int_{-P}^{P} d\rho' \exp[i\mu(\sqrt{\rho_0^2 + \rho'^2} - \rho_0)]$$

$$\times \sum_{m=-\infty}^{+\infty} J_m(\mu\rho_a) J_m(\mu\rho)$$

$$\times \exp[im(\varphi_a - \varphi - \varphi')]. \quad (104)$$

Considering identity (35), Eq. (104) can be rewritten as

$$A_a(\rho,\varphi,z) = \frac{1}{2\pi} U(Z - |z - z_a|) \int_{0}^{+\infty} \mu \, d\mu$$

$$\times \int_{-P}^{P} d\rho' \exp[i\mu(\sqrt{\rho_0^2 + \rho'^2} - \rho_0)]$$

$$\times J_0(\mu\sqrt{\rho_a^2 + \rho^2 - 2\rho_a\rho\cos(\varphi_a - \varphi - \varphi')}). \quad (105)$$

Equation (105) is still complicated. Here, by only considering the points along $\mathbf{r}_a$, i.e., letting $\varphi = \varphi_a$, and then taking the small-aperture approximation ($\varphi' \ll 1$),

$$J_0(u\sqrt{\rho_a^2 + \rho^2 - 2\rho_a\rho\cos(\varphi_a - \varphi - \varphi')}) \approx J_0(\mu|\rho - \rho_a|), \quad (106)$$

and

$$\sqrt{\rho_0^2 + \rho'^2} - \rho_0 \approx \frac{\rho'^2}{2\rho_0}, \quad (107)$$

one can rewrite Eq. (105) as

$$A_a(\rho,\varphi_a,z) = U(Z - |z - z_a|) \int_{-P}^{P} d\rho' \int_{0}^{+\infty} \mu \, d\mu$$

$$\times J_0(\mu|\rho - \rho_a|) \exp(i\mu\rho'^2/2\rho_0). \quad (108)$$

Because $\rho' \ll \rho_0$, the imaginary part is much less than the real part and hence can be neglected,

$$A_a(\rho,\varphi_a,z) = U(Z - |z - z_a|) \int_{-P}^{P} d\rho' \int_{0}^{+\infty} \mu \, d\mu$$

$$\times J_0(\mu|\rho - \rho_a|) \cos(\mu\rho'^2/2\rho_0)$$

$$= U(Z - |z - z_a|) \int_{-P}^{P} d\rho' \left(\frac{\rho_0}{\rho'}\right) \frac{\partial}{\partial\rho'}$$

$$\times \int_{0}^{+\infty} d\mu \, J_0(\mu|\rho - \rho_a|) \sin(\mu\rho'^2/2\rho_0). \quad (109)$$
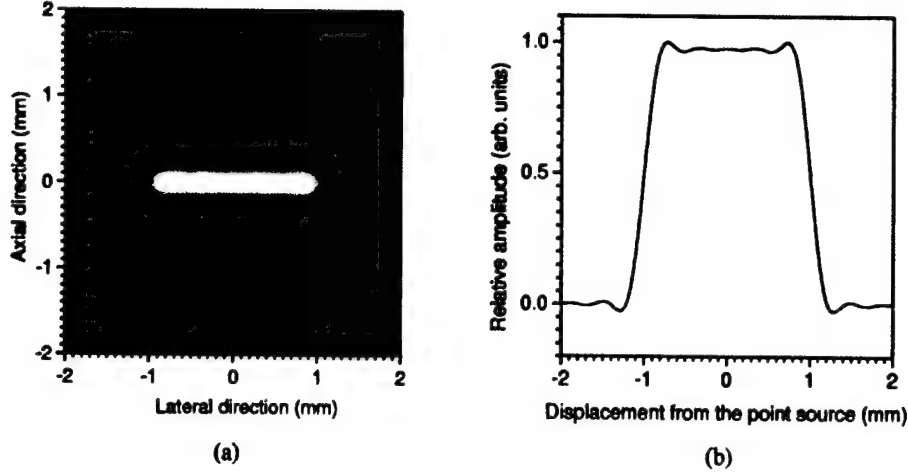
Using the following identity [15]:

FIG. 7. An example of the PSF due to the detector aperture: (a) a gray scale view and (b) a lateral profile through the point source.

$$\int_0^{+\infty} dt\, J_0(ta)\sin(tb) = \begin{cases} \dfrac{1}{\sqrt{b^2-a^2}}, & 0 < a < b \\ 0 & \text{otherwise,} \end{cases}$$

(110)

one can get the integral in Eq. (109),

$$\int_{-P}^{P} d\rho' \left(\frac{\rho_0}{\rho'}\right) \frac{\partial}{\partial \rho'} [\sqrt{(\rho'^2/2\rho_0)^2 - |\rho-\rho_a|^2}]^{-1}$$

$$= \left(\frac{\rho_0}{\rho'}\right) [\sqrt{(\rho'^2/2\rho_0)^2 - |\rho-\rho_a|^2}]^{-1}\big|_{-P}^{P}$$

$$- \int_{-P}^{P} [\sqrt{(\rho'^2/2\rho_0)^2 - |\rho-\rho_a|^2}]^{-1} d\left(\frac{\rho_0}{\rho'}\right).$$

(111)

The integral of Eq. (111) only exists in the range $P^2/2\rho_0 > |\rho-\rho_a|$. Therefore, the PSF extends to a region with a diameter P^2/ρ_0, which is negligible compared to the lateral extension as we discussed in the spherical geometry explanation.

So far, we have derived the analytic PSF's due to the detector apertures for the specific spherical, planar, and cylindrical recording geometries. The explicit expressions can be given when the detector surfaces are assumed to have the same geometric properties as the recording geometries. Otherwise, it appears that explicitly carrying out the analytic derivations is impossible. But, in reality, the detector aperture is very small compared to the recording surface. We have also estimated axial extension in this case and found that it was negligible compared to lateral extension.

V. DISCUSSION AND CONCLUSIONS

In Sec. III, we proved that the PSF as a function of bandwidth is space invariant. In Sec. IV, we demonstrated that the finite aperture of the detector extends the PSF for different recording geometries.

Finally, we attempt to analyze the combined effects of bandwidth and detector size together. Assume that the detected signal is bandlimited, characterized by $\tilde{H}(k)$ with a cutoff frequency k_c, and the detectors have the same geometries as the recording surfaces. One can then follow the derivations in Secs. III and IV and reach the following results.

(1) Spherical geometry:

$$A_{ba}(\mathbf{r}) = \int\int W(\theta')\mathcal{F}_b^{\text{PSF}}(R')r_0^2\sin\theta'\,d\theta'\,d\varphi',$$

(112)

where $R' = \sqrt{r^2+r_a^2-2rr_a\cos\tilde{\gamma}}$, $\cos\tilde{\gamma}=\cos\tilde{\theta}\cos\theta' + \sin\tilde{\theta}\sin\theta'\cos(\tilde{\varphi}-\varphi')$, and $\tilde{\theta}$ and $\tilde{\varphi}$ are the polar and azimuthal angles of vector $\mathbf{n}$ with respect to vector $\mathbf{n}_a$, respectively.

(2) Planar geometry:

$$A_{ba}(x,y,z) = \int\int W(x',y')\mathcal{F}_b^{\text{PSF}}(R')dx'\,dy', \quad (113)$$

where $R' = \sqrt{(x-x_a+x')^2+(y-y_a+y')^2+(z-z_a)^2}$.

(3) Cylindrical geometry:

$$A_{ba}(\rho,\varphi,z) = \int\int W(\varphi',z')\mathcal{F}_b^{\text{PSF}}(R')\rho_0\,d\varphi'\,dz',$$

(114)

where $R' = \sqrt{\rho^2+\rho_a^2-2\rho\rho_a\cos(\varphi-\varphi_a+\varphi')+(z-z_a+z')^2}$.

Equations (112)–(114) clearly reveal that the PSF can be regarded as a convolution of the detector aperture with the space invariant $\mathcal{F}_b^{\text{PSF}}$. However, in the spherical geometry case, the convolution becomes complicated as shown in Eq. (112). Further, we can imagine how complicated the convolution could be with an arbitrary recording geometry using arbitrary-aperture detectors.

Let us take the PSF in the planar geometry case as an example, which is shown in Fig. 7. The detector aperture is assumed to be a disk with a radius of 1 mm and a cutoff frequency $f_c = 4$ MHz. In the axial direction, the extension of the PSF is similar to that shown in Fig. 2(b), which is deter-

mined by the bandwidth. However, as shown Fig. 7(b), the PSF greatly expands in the lateral direction, and its corresponding $\mathcal{W}_{\text{FWHM}} \approx 2$ mm, which is physically limited by the detector size.

In conclusion, spatial resolution as a function of bandwidth is space invariant for any recording geometry when the reconstruction is linear and exact. The bandwidth limits the obtainable spatial resolution. The detector aperture blurs lateral resolution greatly at different levels for different recording geometries but the effect on axial resolution is slight. The results offer clear instruction for designing appropriate thermoacoustic imaging systems with predefined spatial resolutions.

ACKNOWLEDGMENTS

APPENDIX

The completeness relation of the spherical harmonics $Y_{lm}(\theta, \varphi)$ [14,16] is

$$\sum_{l=0}^{\infty} \sum_{m=-l}^{l} Y_{lm}^*(\theta', \varphi') Y_{lm}(\theta, \varphi)$$
$$= \delta(\varphi - \varphi') \delta(\cos\theta - \cos\theta'), \qquad \text{(A1)}$$

where

$$Y_{lm}(\theta, \varphi) = \sqrt{\frac{2l+1}{4\pi} \frac{(l-m)!}{(l+m)!}} P_l^m(\cos\theta) \exp(im\varphi). \tag{A2}$$

Then, do an integral over φ from 0 to 2π of both sides of Eq. (A1),

$$\sum_{l=0}^{\infty} \sum_{m=-l}^{l} \frac{2l+1}{4\pi} \frac{(l-m)!}{(l+m)!} P_l^m(\cos\theta) P_l^m(\cos\theta')$$

$$\times \int_0^{2\pi} \exp[im(\varphi - \varphi')] d\varphi$$

$$= \sum_{l=0}^{\infty} \sum_{m=-l}^{l} \frac{2l+1}{4\pi} \frac{(l-m)!}{(l+m)!} P_l^m(\cos\theta) P_l^m(\cos\theta') 2\pi \delta_{m0}$$

$$= \sum_{l=0}^{\infty} \frac{2l+1}{4\pi} P_l(\cos\theta) P_l(\cos\theta') 2\pi$$

$$= \delta(\cos\theta - \cos\theta') \int_0^{2\pi} \delta(\varphi - \varphi') d\varphi = \delta(\cos\theta - \cos\theta'),$$
$$\tag{A3}$$

i.e.,

$$\sum_{l=0}^{\infty} (2l+1) P_l(\cos\theta) P_l(\cos\theta') = 2\delta(\cos\theta - \cos\theta'). \tag{A4}$$

[1] C. G. A. Hoelen, F. F. M. de Mul, R. Pongers, and A. Dekker, Opt. Lett. **23**, 648 (1998).

[2] R. A. Kruger, W. L. Kiser, K. D. Miller, H. E. Reynolds, D. R. Reinecke, G. A. Kruger, and P. J. Hofacker, Proc. SPIE **3916**, 150 (2000).

[3] K. P. Köstli, D. Frauchiger, J. J. Niederhauser, G. Paltauf, H. P. Weber, and M. Frenz, IEEE J. Sel. Top. Quantum Electron. **7**, 918 (2001).

[4] R. O. Esenaliev, A. A. Karabutov, and A. A. Oraevsky, IEEE J. Sel. Top. Quantum Electron. **5**, 981 (1999).

[5] G. Ku and L.-H. V. Wang, Med. Phys. **28**, 4 (2001).

[6] M. Xu, G. Ku, and L.-H. V. Wang, Med. Phys. **28**, 1958 (2001).

[7] M. Xu and L.-H. V. Wang, IEEE Trans. Med. Imaging **21**, 814 (2002).

[8] Y. Xu, D.-Z. Feng, and L.-H. V. Wang, IEEE Trans. Med. Imaging **21**, 823 (2002).

[9] Y. Xu, M. Xu, and L.-H. V. Wang, IEEE Trans. Med. Imaging **21**, 829 (2002).

[10] M. Xu and L.-H. V. Wang, Med. Phys. **29**, 1661 (2002).

[11] M. Xu, Y. Xu, and L.-H. V. Wang, IEEE Trans. Biomed. Eng. (to be published).

[12] Y. Xu and L.-H. Wang (unpublished).

[13] A. C. Tam, Rev. Mod. Phys. **58**, 381 (1986).

[14] G. B. Arfken and H. J. Weber, *Mathematical Methods for Physicists* (Academic, San Diego, 1995).

[15] M. Abramowitz and I. A. Stegun, *Handbook of Mathematical Functions with Formulas, Graphs, and Mathematical Tables* (Dover, New York, 1965).

[16] J. D. Jackson, *Classical Electrodynamics* (Wiley, New York, 1999).

[17] P. M. Morse and K. U. Ingard, *Theoretical Acoustics* (McGraw-Hill, New York, 1968).

Time-Domain Reconstruction Algorithms and Numerical Simulations for Thermoacoustic Tomography in Various Geometries

Minghua Xu, Yuan Xu, and Lihong V. Wang*, *Senior Member, IEEE*

Abstract—In this paper, we present time-domain reconstruction algorithms for the thermoacoustic imaging of biological tissues. The algorithm for a spherical measurement configuration has recently been reported in another paper. Here, we extend the reconstruction algorithms to planar and cylindrical measurement configurations. First, we generalize the rigorous reconstruction formulas by employing Green's function technique. Then, in order to detect small (compared with the measurement geometry) but deeply buried objects, we can simplify the formulas when two practical conditions exist: 1) that the high-frequency components of the thermoacoustic signals contribute more to the spatial resolution than the low-frequency ones, and 2) that the detecting distances between the thermoacoustic sources and the detecting transducers are much greater than the wavelengths of the high-frequency thermoacoustic signals (i.e., those that are useful for imaging). The simplified formulas are computed with temporal back projections and coherent summations over spherical surfaces using certain spatial weighting factors. We refer to these reconstruction formulas as modified back projections. Numerical results are given to illustrate the validity of these algorithms.

Index Terms—Algorithm, geometry, imaging, photoacoustics, reconstruction, thermoacoustics, time-domain, tomography.

I. INTRODUCTION

RECENT research has suggested that thermoacoustic tomography using either pulsed radio-frequency (RF) [1]–[8] or pulsed laser [9]–[12] can be a powerful imaging technology with good spatial resolution. Within this technique, when a pulsed electromagnetic irradiation is absorbed by a tissue, the heating and subsequent expansion of the tissue give rise to an instantaneous acoustic stress or pressure distribution inside the tissue. Directly following the pulse irradiation, the induced pressure distribution prompts acoustic wave propagation toward the surface of the tissue with various time delays. Ultrasound detectors are placed around the tissue to record the outgoing acoustic waves. These detected acoustic waves can be used to inversely compute the distribution of the initial acoustic pressure or electromagnetic absorption, which is related to the properties of the tissue.

In fact, electromagnetic fields in the RF range of 300 to 3000 MHz are the most useful in the study of soft tissues sized in centimeters. The RF penetration depth at this frequency range varies depending on the tissue properties and the RF frequency [3], [13], [14]. For example, the penetration depths for muscle and fat are about 1.2 and 9 cm at 3 GHz, respectively, and about 4 and 30 cm at 300 MHz, respectively; most other soft tissues have penetration depths that fall between these values. In addition, in this frequency range, there is very little scattering by the tissues [13].

In a typical application of thermoacoustic imaging using RF, a short-pulsed RF field illuminates the tissue. The most investigated and documented effect of RF power on biological tissues is the transformation of energy entering the tissues into increased kinetic energy in the absorbing molecules, thereby producing a general heating in the medium [13]. The heating results from both ionic conduction and vibration of the dipole molecules of water and proteins [13]. The energy absorbed by the tissue produces a temperature rise that is dependent on the cooling mechanism of tissue [13]. Human exposure to RF power must be limited for safety reasons, and within the mandated safety limits, the temperature rise per short pulse (such as 1 μs) in soft tissue is very small (on the order of milli-degrees) [6].

Nevertheless, this small temperature rise causes linear expansion of the tissue. The heating and expansion are greatest in those regions of the tissue that absorb the most RF power. Therefore, a distribution of acoustic pressure or stress inside the tissue is induced immediately during the short RF-pulse irradiation period due to heterogeneities of the RF energy deposition and the Grüneisen parameter inside the inhomogeneous tissue. Thermal expansion due to energy deposition is commonly referred to as the *thermoelastic effect* [15]. The generated acoustic pressure is on the order of mBar [6]. Such a small value does not cause tissue damage.

Subsequently, after the RF-pulse irradiation, the acoustic stresses inside the tissue relax. They act as instantaneous acoustic sources inside the tissue, which promote acoustic wave propagation. These acoustic waves contain acoustic frequencies ranging from very low frequencies to high frequencies that approximate the reciprocal of the RF pulse duration. The acoustic detectors, called ultrasound transducers [16], which can convert mechanical stresses into electrical signals, are placed around the tissue to record these outgoing acoustic waves, commonly

referred to as *thermoacoustic or photoacoustic signals*. These thermoacoustic signals carry information about the RF absorption or initiated stress as well as about the acoustic properties of the tissue. Since the RF absorption or initiated stress is directly related to certain tissue properties (i.e., ionic conductivity and water components, etc.), the key problem is how to reconstruct the distribution of the RF absorption or initiated stress from the measured thermoacoustic signals around the tissue surface.

The short duration of the RF pulse allows one to restrict the RF energy deposition within the absorbing volume and minimize the thermal diffusion effect on the thermoacoustic waves. In thermoacoustic imaging, the RF pulse duration, τ_p, is typically shorter than the thermal transport time of absorbed RF energy in thermal conduction, τ_{th}, the condition that is commonly referred to as *thermal confinement* [17]. The condition for thermal confinement can be expressed as $\tau_p < \tau_{th} \sim l_p^2/\alpha$, where α is the thermal diffusivity of the irradiated material and l_p is the RF penetration depth or the size of the absorbing structure. For most soft tissues, $\alpha \sim 10^3$ cm$^2 \cdot$ s^{-1} [14]. For example, we are interested in the detection of small absorbers in sizes from submillimeters to centimeters inside the tissue. We choose $l_p \sim$ mm to underestimate the thermal transport time $\tau_{th} \sim 10$ μs. The RF pulse used, τ_p, is typically less than 1 μs, which is much less than τ_{th}. Moreover, the time required for an acoustic wave to traverse the absorption depth l_p approximates to $\sim l_p/c \approx 0.7$ μs, which is also much shorter than τ_{th}, where c is the sound speed that is around 1.5 mm/μs in most soft tissues [14]. In other words, even in 1 μs of RF pulse duration, the heat transports a length of $\sqrt{\alpha \tau_p} \sim 0.3$ mm, while in the same amount of time, the acoustic wave propagates a distance of $c\tau_p \sim 1.5$ mm, which is far away from the thermal diffusion region of 0.3 mm. Of course, thermal diffusion will slightly blur the reconstructed images. But, when we try to investigate targets that are bigger than the thermal diffusion region, for instance, > 0.3 mm, if the RF pulse duration is less than 1 μs, the thermal effect on the thermoacoustic waves in soft tissue can be ignored. In addition, the thermoacoustic signal excited by a RF pulse with finite width can be regarded as a convolution with the RF pulse profile and the thermoacoustic signal excited by a $\delta(t)$ RF irradiation. For theoretical analysis, the short pulse can be regarded as a delta function.

In general, thermoacoustic imaging can be used for the investigation of soft tissues with inhomogeneous RF absorption but relatively homogeneous acoustic properties including the speed of sound and low acoustic attenuation. For practical purposes, speed dispersion can be neglected in soft tissues; typically, the speed increases by about 0.01% MHz^{-1} [16]. In most soft tissues, the speed of sound is relatively constant at ~ 1.5 mm/μs with a small variation about 5% [14], [16]. Acoustic attenuation in soft tissues is primarily due to the spectra of the relaxation processes, which account for the nearly linear frequency dependence [16]. The total acoustic attenuation in soft tissues results from combined losses due to absorption and scattering [14], [16]. In the low megahertz range, acoustic scattering in soft tissues accounts for only about 10% of the total acoustic attenuation [14]. A mean value of the acoustic energy attenuation in soft tissue is equal to 0.6 dB$\cdot$cm$^{-1}\cdot$MHz^{-1} [16]. Typically, the total energy attenuation for a 1-MHz signal after a 5-cm prop-

agation is about 3 dB, and the corresponding amplitude attenuates approximately to 70% of the initial value. Such attenuation is still acceptable, although the spatial resolution will be blurred at a certain level due to the loss of the high-frequency signal. For simplicity, the acoustic attenuation is neglected here. Pure acoustic property differentiation should appeal to conventional ultrasound imaging [16]. The unique advantage of thermoacoustic imaging is its ability to detect the inhomogeneous RF absorption property of tissues when the acoustic property is homogeneous. An obvious application is the detection of breast cancer tumors. People have observed that tumors in the breast have a stronger rate of RF absorption than the surrounding tissues; by contrast, the ultrasonic contrast in soft tissues is quite low [8].

In previous papers [2]–[4], the authors have presented studies on scanning thermoacoustic tomography using focused ultrasonic transducers as in conventional pulse-echo ultrasound imaging [16]. Each scan line is converted into a one-dimensional (1-D) image along the axis of the focused transducer, and only a simple calculation is required to construct cross-sectional images from all of the scan lines. However, the lateral resolution of this approach is determined by the focal diameter of the transducer as with conventional ultrasound, and the imaging region is also limited to the focal length of the transducer. To obtain a larger imaging view, we use unfocused wide-band point transducers to record the thermoacoustic signals. In this approach, a complicated reconstruction algorithm has to be derived for computing the images from a set of data measured around the tissue under study. Different recording geometric configurations result in different reconstruction formulas.

The puzzle of finding good reconstruction algorithms has not yet been resolved. Some researchers have resorted to approximated reconstruction algorithms, such as the Radon transform in the far-field approximation [7], [9], the weighted delay-and-sum method with experiential weighting factors [10], or the optimal statistical approach [18]. To date, some rigorous reconstruction algorithms have been reported for idealized measurement configurations, such as for the fully enclosing spherical recording surface [5], the planar recording surface of an infinite extent [19], [20] and the cylindrical recording surface of an infinite length [21]. However, in practical applications, the recording surfaces are generally finite and partially enclosing.

In this paper, we will first discuss the inverse problem of thermoacoustic imaging. Then, by employing the Green's function technique, we will generalize the rigorous reconstruction formulas for three types of recording surfaces: a planar, a spherical, and a cylindrical surface, which enclose the sample under study. In order to detect small but relatively deeply buried targets, we will introduce the following two conditions (details given in Section II): the high-frequency components of thermoacoustic signals contribute more to spatial resolution than the low-frequency ones, and the detecting distances between the thermoacoustic sources and the detecting transducers are much larger than the wavelengths of the high-frequency thermoacoustic signals that are useful for imaging. Taking these conditions into account, we will simplify the rigorous formulas and present time-domain reconstruction algorithms, which can be computed by temporal back projections and coherent summations over

spherical surfaces with certain spatial weighting factors. Finally, numerical experiments will be conducted to demonstrate the validity of these formulas.

II. INVERSE PROBLEM

As discussed in Section I, in typical thermoacoustic measurements, the RF pulse duration is so short that the thermal conduction time is far greater than the thermoacoustic transit time and the effect of thermal diffusion on the thermoacoustic wave in the tissue can be ignored. We focus on small-amplitude thermoacoustic propagation using safe levels of RF irradiation. Thus, the inverse problem that we want to solve is a linear acoustic-wave equation.

The pressure $p(\mathbf{r}, t)$ at position $\mathbf{r}$ and time t in an acoustically homogeneous medium in response to a heat source $H(\mathbf{r}, t)$ obeys the following equation [5], [23]:

$$\nabla^2 p(\mathbf{r}, t) - \frac{1}{c^2}\frac{\partial^2}{\partial t^2}p(\mathbf{r}, t) = -\frac{\beta}{C_p}\frac{\partial}{\partial t}H(\mathbf{r}, t) \qquad (1)$$

where C_p is the specific heat, $H(\mathbf{r}, t)$ is the heating function defined as the thermal energy deposited by the energy source per time and volume, β is the isobaric volume expansion coefficient, and c is the speed of sound. The heating function can be written as the product of a spatial absorption function and a temporal illumination function of the RF source

$$H(\mathbf{r}, t) = A(\mathbf{r})I(t). \qquad (2)$$

As discussed in Section I, the short RF pulse can be regarded as a Dirac delta function

$$I(t) = \delta(t). \qquad (3)$$

Substituting (2) and (3) into (1) and taking the Fourier transform on variable $\bar{t} = ct$ of (1), one gets

$$(\nabla^2 + k^2)\widetilde{p}(\mathbf{r}, k) = ikc^2\eta A(\mathbf{r}) \qquad (4)$$

where $\eta = \beta/C_p$, and the following Fourier transform pair exists:

$$\widetilde{p}(\mathbf{r}, k) = \int_{-\infty}^{+\infty} p(\mathbf{r}, \bar{t})\exp(ik\bar{t})d\bar{t}, \qquad (5)$$

$$p(\mathbf{r}, \bar{t}) = \frac{1}{2\pi}\int_{-\infty}^{+\infty} \widetilde{p}(\mathbf{r}, k)\exp(-ik\bar{t})dk \qquad (6)$$

where the acoustic wave number $k = \omega/c$ and ω is the angular frequency and equal to $2\pi f$; and $\widetilde{p}(\mathbf{r}, k)$ is the frequency spectrum of the thermoacoustic signal $p(\mathbf{r}, \bar{t})$. Equation (4) is a nonhomogeneous Helmholtz equation. Assume that the thermoacoustic signals are measured on a surface S_0 that encloses the sample under study, the frequency spectrum of the thermoacoustic pressure measured at the position $\mathbf{r}_0$ on surface S_0 can be expressed as [22]

$$\widetilde{p}(\mathbf{r}_0, k) = -ikc^2\eta \iiint_V d^3r A(\mathbf{r})\widetilde{G}_k(\mathbf{r}, \mathbf{r}_0) \qquad (7)$$

where $\widetilde{G}_k(\mathbf{r}, \mathbf{r}_0)$ is the Green's function of the nonhomogeneous equation

$$(\nabla^2 + k^2)\widetilde{G}_k(\mathbf{r}, \mathbf{r}_0) = -\delta(\mathbf{r} - \mathbf{r}_0). \qquad (8)$$

In general, Green's function in three dimensions can be written as [22]

$$\widetilde{G}_k(\mathbf{r}, \mathbf{r}_0) = \frac{\exp(ik|\mathbf{r} - \mathbf{r}_0|)}{4\pi|\mathbf{r} - \mathbf{r}_0|}. \qquad (9)$$

Now, the inverse problem is to reconstruct the absorption distribution $A(\mathbf{r})$ from a set of data $p(\mathbf{r}_0, t)$ or $\widetilde{p}(\mathbf{r}_0, k)$ measured at position $\mathbf{r}_0$. Equation (7) shows a linear mapping connecting $A(\mathbf{r})$ and $\widetilde{p}(\mathbf{r}_0, k)$. The solution of $A(\mathbf{r})$ can be expected in a similar form—a linear integral

$$A(\mathbf{r}) = \iint_{S_0} dS_0 \int_k dk\widetilde{p}(\mathbf{r}_0, k)\widetilde{K}_k(\mathbf{r}_0, \mathbf{r}) \qquad (10)$$

where $dS_0 = d^2\mathbf{r}_0$, S_0 is the total recording surface, and the integral kernel $\widetilde{K}_k(\mathbf{r}_0, \mathbf{r})$ needs to be determined. As shown in Section III, the integral kernel is complicated. But under most practical conditions, as discussed below, it can be simplified to a linear relation with the Green's function.

The greatest challenge is to detect small (compared with measurement geometry) but deeply buried targets inside the tissue. Let us check the property of the frequency spectrum of acoustic waves generated from a small object. Assume there is a homogeneous RF absorption sphere with a size of $2a$ in diameter, i.e., the spatial absorption function $A(\mathbf{r}) = U(a-r)$, where the step function $U(\xi) = 1, \xi \geq 0$ and $U(\xi) = 0, \xi < 0$. With a $\delta(t)$ RF illumination, the radiated acoustic wave from this sphere can be expressed as $p(r, t) = \eta c^2 U(a - |r - ct|)(r - ct)/(2r)$ [23]. Applying the Fourier transform gives the frequency spectrum $\sim j_1(ka)$, where $j_1(ka)$ is the spherical Bessel function of the first kind. The main beam of the above spectrum is in a belly shape with maximum amplitude at the central frequency $f_c \approx 0.7c/(2a)$. For example, for an object with a size of 1 mm, $f_c = 0.7 \times 1.5 \ (\text{mm}/\mu\text{s})/(1 \ \text{mm}) \approx 1$ MHz. Below 100 KHz, the spectrum amplitude is less than 0.1 of the maximum value, and particularly at 0 Hz, the spectrum amplitude is zero, which can be proved using (7) letting $k = 0$. In general, the frequency spectrum of acoustic waves generated from a small object concentrates in the relatively high-frequency region. The dominating frequency or central frequency f_c can be approximated by the reciprocal of the required time τ for an acoustic wave to traverse the object length l, i.e., $f_c \approx 1/\tau = c/l$. In addition, the boundaries of large objects can also be regarded as small structures, which are also determined by relatively high-frequency signals. In other words, only the relatively high-frequency thermoacoustic signals can restore small absorbers as well as the boundaries of big absorbers.

During measurement, the transducer for ultrasonic imaging [16] can be employed to receive thermoacoustic signals. The ideal transducer for receiving ultrasound would have a wide dynamic range and a wide frequency response. Most commonly, transducers are operated over a band of frequencies containing

a resonant frequency, which is determined by the physical property of the transducer [16]. A transducer with a resonant or central frequency of 1–3 MHz could be perfectly matched to millimeter-sized small absorbers in soft tissues. The real-time localization of targets should employ transducer arrays, in which all of the small elements serve independent ultrasound detectors and simultaneously receive thermoacoustic signals at different positions around the investigated tissue [16]. Currently, a linear or circular array with hundreds of small elements, in which each element has a size of ∼sub-mm with a total length of perhaps ∼10 cm, is available on the market or can be customized and manufactured in a research lab [16]. In addition, the measurement geometry is relatively big compared with the small targets. For example, when using a spherical measurement configuration with a radius $r_0 = 5$ cm, even at $f = 100$ KHz, $kr_0 \approx 20 \gg 1$. In another example, for a target inside a tissue with a distance to the nearest detection element $d = 1$ cm, at $f = 1$ MHz, $kd \approx 40 \gg 1$ and even at $f = 100$ KHz, $kd \approx 4 > 1$.

Therefore, for practical applications, we introduce the following two conditions: the high-frequency components of the thermoacoustic signals contribute more to the spatial resolution than the low-frequency ones, and the detecting distances between the thermoacoustic sources and the detecting transducers are much larger than the wavelengths of the high-frequency thermoacoustic signals. Taking these conditions into account, we will simplify the rigorous formulas and present time-domain reconstruction algorithms in the following sections.

III. RECONSTRUCTION FORMULAS

A. Planar Measurement Configuration

The Cartesian coordinate system $\mathbf{r} = (x, y, z)$ suits this situation. As shown in Fig. 1(a), we assume that the measurement surface is the $z = 0$ plane, i.e., $\mathbf{r}_0 = (x_0, y_0, 0)$. The sample lies above the plane, i.e., $A(\mathbf{r}) = A(x, y, z)$ where $z > 0$ and $A(\mathbf{r}) = 0$ when $z < 0$. Taking Fourier transforms on both sides of (8) on variables x, y and z, it can be shown that the Green's function is a triple Fourier integral [22]

$$\widetilde{G}_k(\mathbf{r}, \mathbf{r}_0) = \frac{1}{(2\pi)^3} \int\!\!\!\int_{-\infty}^{+\infty}\!\!\!\int dK_x dK_y dK_z$$

$$\cdot \frac{\exp\left[iK_x(x_0 - x) + iK_y(y_0 - y) - iK_z z\right]}{K_x^2 + K_y^2 + K_z^2 - k^2}. \quad (11)$$

Considering the above expansion, and referencing the mathematical techniques in Norton's work on ultrasonic reflectivity imaging [24], we can derive a rigorous reconstruction formula in the form of (10) as (see Appendix A)

$$A(x, y, z) = \int\!\!\!\int_{-\infty}^{+\infty} dx_0 dy_0 \int_{-\infty}^{+\infty} dk \widetilde{p}(x_0, y_0, k) \widetilde{K}_k(\mathbf{r}_0, \mathbf{r}) \quad (12)$$

with

$$\widetilde{K}_k(\mathbf{r}_0, \mathbf{r}) = \frac{1}{4\pi^3 c^2 \eta} \int\!\!\!\int_{\rho=0}^{\rho=|k|} du\, dv \exp\left[-iz\,\mathrm{sgn}(k)\sqrt{k^2 - \rho^2}\right]$$

$$\cdot \exp[iu(x_0 - x) + iv(y_0 - y)] \quad (13)$$
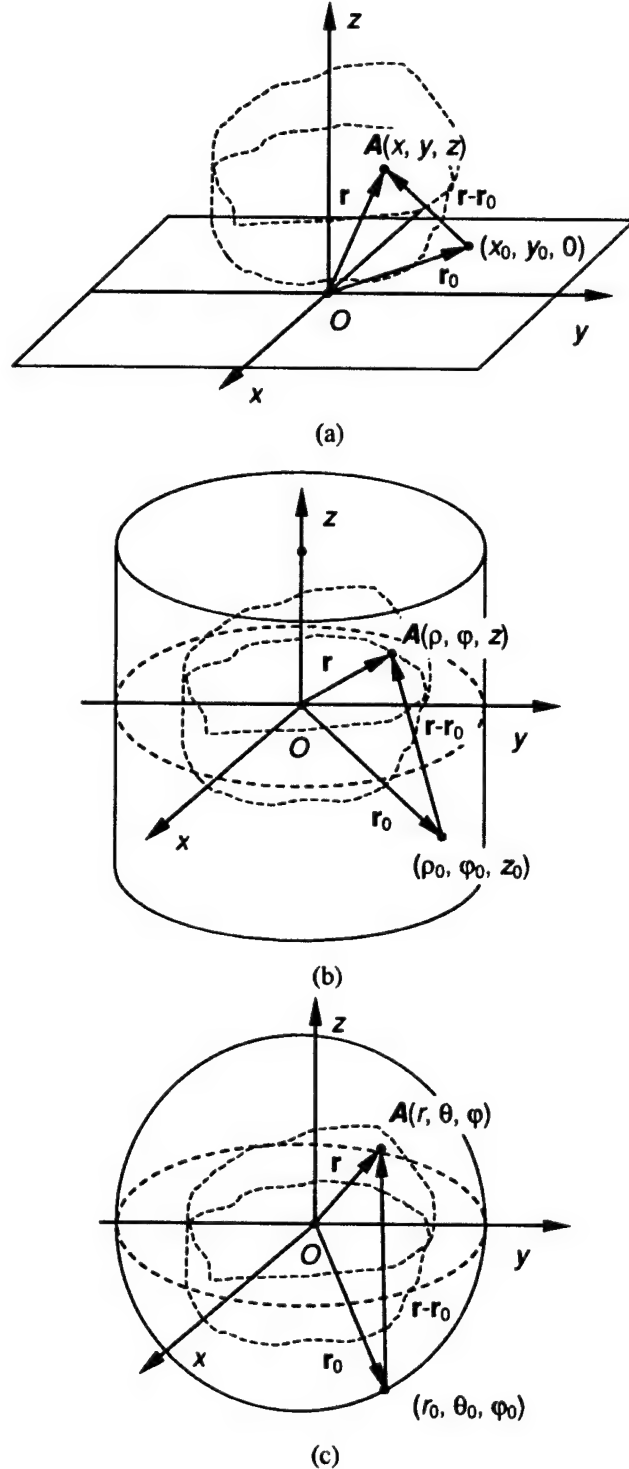
Fig. 1. Diagram of the measurement: (a) planar measurement configuration, (b) cylindrical measurement configuration, and (c) spherical measurement configuration.

where $\rho = \sqrt{u^2 + v^2}$, and the sign function: $\mathrm{sgn}(k) = 1$ if $k > 0$, and $\mathrm{sgn}(k) = -1$ if $k < 0$.

Under the condition $|k||\mathbf{r} - \mathbf{r}_0| \gg 1$, which means that the detecting distances between the thermoacoustic sources and the detecting transducers are much greater than the wavelengths of

the thermoacoustic signals that are useful for imaging, (13) reduces to (see Appendix A)

$$\widetilde{K}_k(\mathbf{r}_0, \mathbf{r}) \approx \frac{i2k}{\pi c^2 \eta} \frac{z}{|\mathbf{r} - \mathbf{r}_0|} \widetilde{G}_k^*(\mathbf{r}, \mathbf{r}_0), \qquad (14)$$

where "$*$" stands for the complex conjugate.

It can be shown that $\mathbf{n} \cdot \mathbf{n}_0 = z/|\mathbf{r} - \mathbf{r}_0|$, where $\mathbf{n}$ and $\mathbf{n}_0$ are unit vectors pointing along the z axis and along the line joining $\mathbf{r}$ and $\mathbf{r}_0$, respectively. Substituting (14) into (12), we get

$$A(\mathbf{r}) = \iint_{S_0} dS_0 \int_{-\infty}^{+\infty} dk \frac{i2k}{\pi c^2 \eta} \widetilde{p}(\mathbf{r}_0, k) \widetilde{G}_k^*(\mathbf{r}, \mathbf{r}_0)[\mathbf{n} \cdot \mathbf{n}_0]$$

$$= -\frac{1}{\pi c^2 \eta} \iint_{S_0} dS_0 \cdot \frac{1}{2\pi} \int_{-\infty}^{+\infty} dk (-ik) \widetilde{p}(\mathbf{r}_0, k)$$

$$\times \frac{\exp\left(-ik|\mathbf{r} - \mathbf{r}_0|\right)}{|\mathbf{r} - \mathbf{r}_0|} [\mathbf{n} \cdot \mathbf{n}_0] \qquad (15)$$

where $dS_0 = dx_0 dy_0$. Recalling the inverse Fourier transform of (6), (15) reduces to

$$A(\mathbf{r}) = -\frac{1}{\pi c^4 \eta} \iint_{S_0} dS_0 [\mathbf{n} \cdot \mathbf{n}_0] \frac{1}{t} \left. \frac{\partial p(\mathbf{r}_0, t)}{\partial t} \right|_{t = \frac{|\mathbf{r}_0 - \mathbf{r}|}{c}}. \quad (16)$$

This is a modified back projection formula of quantity $-(1/t)(\partial p(\mathbf{r}_0, t)/\partial t)$ with a weighting factor $[\mathbf{n} \cdot \mathbf{n}_0]$. The required condition is $|k||\mathbf{r} - \mathbf{r}_0| >> 1$.

B. Cylindrical Measurement Configuration

In this case, a circular cylindrical coordinate system $\mathbf{r} = (\rho, \varphi, z)$ is convenient. As shown in Fig. 1(b), we assume that the measurement surface is a circular cylindrical surface $\mathbf{r}_0 = (\rho_0, \varphi_0, z_0)$. The sample (of a finite size) lies inside the cylinder. The Green's function can be expressed in the cylindrical coordinates ($k > 0$) (see Appendix B for detail)

$$\widetilde{G}_k(\mathbf{r}, \mathbf{r}_0) = \frac{1}{4\pi^2} \sum_{m=-\infty}^{+\infty} \exp\left[im(\varphi - \varphi_0)\right]$$

$$\cdot \int_{-\infty}^{+\infty} dk_z \exp\left[ik_z(z - z_0)\right] g_{mk}(\rho, \rho_0, k_z) \quad (17)$$

where if $k_z^2 < k^2$, $g_{mk}(\rho, \rho_0, k_z) = (i\pi/2) J_m(\mu\rho) H_m^{(1)}(\mu\rho_0)$ with $\mu = \sqrt{k^2 - k_z^2}$; if $k_z^2 > k^2$, $g_{mk}(\rho, \rho_0, k_z) = I_m(-i\mu\rho) K_m(-i\mu\rho_0)$ with $\mu = i\sqrt{k_z^2 - k^2}$. $J_m(\cdot)$, $H_m^{(1)}(\cdot)$, $I_m(\cdot)$ and $K_m(\cdot)$ are the Bessel function of the first kind, the Hankel function of the first kind, the modified Bessel function of the first kind, and the modified Bessel function of the second kind, respectively.

After some deduction (see Appendix B), we get the reconstruction formula in the form of (10) as

$$A(\rho, \varphi, z) = \iint_{S_0} dS_0 \int_0^{+\infty} dk \widetilde{p}(\mathbf{r}_0, k) \widetilde{K}_k(\mathbf{r}_0, \mathbf{r}) \quad (18)$$

where $dS_0 = \rho_0 d\varphi_0 dz_0$, and

$$\widetilde{K}_k(\mathbf{r}_0, \mathbf{r}) = \frac{1}{2\pi^3 c^2 \eta \rho_0} \int_{-k}^{+k} d\gamma \exp\left[i\gamma(z_0 - z)\right]$$

$$\cdot \sum_{n=-\infty}^{+\infty} \exp\left[in(\varphi_0 - \varphi)\right] \frac{J_n(\rho\sqrt{k^2 - \gamma^2})}{H_n^{(1)}(\rho_0\sqrt{k^2 - \gamma^2})}. \quad (19)$$

Under the conditions introduced in Section II, i.e., $\rho_0 k \gg 1$, (19) approximates to (see Appendix B)

$$\widetilde{K}_k(\mathbf{r}_0, \mathbf{r}) \approx \frac{i2k}{\pi c^2 \eta} \sqrt{1 - \frac{(z_0 - z)^2}{|\mathbf{r} - \mathbf{r}_0|^2}} \widetilde{G}_k^*(\mathbf{r}, \mathbf{r}_0). \quad (20)$$

Adding the complex conjugate of (18) onto itself and then dividing the summation by two, and further considering $\widetilde{p}^*(\mathbf{r}_0, k) = \widetilde{p}(\mathbf{r}_0, -k)$ and the approximation (20), one gets

$$A(\rho, \varphi, z) = \iint_{S_0} dS_0 \int_{-\infty}^{+\infty} dk \frac{ik}{c^2 \eta \pi} \widetilde{p}(\mathbf{r}_0, k)$$

$$\cdot \frac{\exp\left(-ik|\mathbf{r} - \mathbf{r}_0|\right)}{4\pi |\mathbf{r} - \mathbf{r}_0|} \sqrt{1 - \frac{(z_0 - z)^2}{|\mathbf{r} - \mathbf{r}_0|^2}}$$

$$= -\frac{1}{2\pi c^2 \eta} \iint_{S_0} dS_0 \sqrt{1 - \frac{(z_0 - z)^2}{|\mathbf{r} - \mathbf{r}_0|^2}}$$

$$\cdot \frac{1}{2\pi} \int_{-\infty}^{+\infty} (-ik) dk \widetilde{p}(\mathbf{r}_0, k) \frac{\exp\left(-ik|\mathbf{r} - \mathbf{r}_0|\right)}{|\mathbf{r} - \mathbf{r}_0|}.$$

$$(21)$$

It can be shown that

$$\mathbf{n} \cdot \mathbf{n}_0 = \frac{|\boldsymbol{\rho} - \boldsymbol{\rho}_0|}{|\mathbf{r} - \mathbf{r}_0|}$$

$$= \sqrt{\frac{\rho^2 + \rho_0^2 - 2\rho\rho_0 \cos(\varphi_0 - \varphi)}{|\mathbf{r} - \mathbf{r}_0|^2}}$$

$$= \sqrt{1 - \frac{(z_0 - z)^2}{|\mathbf{r} - \mathbf{r}_0|^2}} \quad (22)$$

where $\boldsymbol{\rho}$ and $\boldsymbol{\rho}_0$ are the projections of $\mathbf{r}$ and $\mathbf{r}_0$ on z plane, respectively, and $\mathbf{n}$ and $\mathbf{n}_0$ are unit vectors pointing along the line joining $\boldsymbol{\rho}$ and $\boldsymbol{\rho}_0$ and along the line joining $\mathbf{r}$ and $\mathbf{r}_0$, respectively. Recalling the inverse transformation (6), we can rewrite (21) as

$$A(\rho, \varphi, z) = -\frac{1}{2\pi c^4 \eta} \iint_{S_0} dS_0 [\mathbf{n} \cdot \mathbf{n}_0] \frac{1}{t} \left. \frac{\partial p(\mathbf{r}_0, t)}{\partial t} \right|_{t = \frac{|\mathbf{r} - \mathbf{r}_0|}{c}}. \quad (23)$$

This is a modified back projection formula of quantity $-(1/t)(\partial p(\mathbf{r}_0, t)/\partial t)$ with a weighting factor $[\mathbf{n} \cdot \mathbf{n}_0]$. The required condition is $\rho_0 |k| \gg 1$ and $|k||\mathbf{r} - \mathbf{r}_0| \gg 1$.

C. Spherical Measurement Configuration

This instance has been reported in another paper [5]. As a consequence, we only briefly review the results here for completeness.

We use the spherical polar coordinate system $\mathbf{r} = (r, \theta, \varphi)$. As shown in Fig. 1(c), we assume that the recording surface is a spherical surface $\mathbf{r}_0 = (r_0, \theta_0, \varphi_0)$. The sample lies inside the sphere, i.e., $A(\mathbf{r}) = A(r, \theta, \varphi)$ where $r < r_0$ and $A(\mathbf{r}) = 0$ when $r > r_0$. The Green's function can be expanded as a series based on the spherical Bessel function of the first kind $j_l(\cdot)$, the spherical Hankel function of the first kind $h_l(\cdot)$, and the Legendre polynomial $P_l(\cdot)$

$$\widetilde{G}_k(\mathbf{r}, \mathbf{r}_0) = \frac{ik}{4\pi} \sum_{l=0}^{\infty} (2l + 1) j_l(kr) h_l^{(1)}(kr_0) P_l(\mathbf{n} \cdot \mathbf{n}_0), \quad (k > 0) \tag{24}$$

where $\mathbf{n} = \mathbf{r}/r$, and $\mathbf{n}_0 = \mathbf{r}_0/r_0$.

We find the rigorous reconstruction formula as

$$A(r, \theta, \varphi) = \iint_{S_0} dS_0 \int_0^{+\infty} dk \widetilde{p}(\mathbf{r}_0, k) \widetilde{K}_k(\mathbf{r}_0, \mathbf{r}) \tag{25}$$

where $dS_0 = r_0^2 \sin \theta_0 d\theta_0 d\varphi_0$, and

$$\widetilde{K}_k(\mathbf{r}_0, \mathbf{r}) = \frac{1}{2\pi^2 c^2 \eta r_0^2} \sum_{m=0}^{\infty} \frac{(2m + 1) j_m(kr)}{h_m^{(1)}(kr_0)} P_m(\mathbf{n} \cdot \mathbf{n}_0). \tag{26}$$

Under the condition $kr_0 \gg 1$, one can approximate

$$\widetilde{K}_k(\mathbf{r}_0, \mathbf{r}) \approx \frac{i2k}{\pi c^2 \eta} \widetilde{G}_k^*(\mathbf{r}, \mathbf{r}_0). \tag{27}$$

Adding the complex conjugate of (25) onto itself and then dividing the summation by two, and further considering $\widetilde{p}^*(\mathbf{r}_0, k) = \widetilde{p}(\mathbf{r}_0, -k)$ and the approximation (27), we get

$$A(r, \theta, \varphi) = -\frac{1}{2\pi c^2 \eta} \iint_{S_0} dS_0$$

$$\cdot \frac{1}{2\pi} \int_{-\infty}^{+\infty} dk \widetilde{p}(\mathbf{r}_0, k)(-ik) \frac{\exp(-ik|\mathbf{r}_0 - \mathbf{r}|)}{|\mathbf{r}_0 - \mathbf{r}|}. \tag{28}$$

Recalling the inverse Fourier transform (6), (28) reduces to

$$A(r, \theta, \varphi) = -\frac{1}{2\pi c^4 \eta} \iint_{S_0} dS_0 \frac{1}{t} \left. \frac{\partial p(\mathbf{r}_0, t)}{\partial t} \right|_{t = \frac{|\mathbf{r}_0 - \mathbf{r}|}{c}}. \tag{29}$$

Equation (29) shows that the absorption distribution can be calculated by means of back projection of the quantity $-(1/t)(\partial p(\mathbf{r}_0, t)/\partial t)$. The required condition is $|k|r_0 \gg 1$.

As expected, all of the reconstruction formulas—(16) for the planar measurement configuration, (23) for the cylindrical measurement configuration, and (29) for the spherical measurement configuration—can be carried out in the time domain. They share a similar expression, except for the weighting factor $[\mathbf{n} \cdot \mathbf{n}_0]$. These formulas can be referred to as modified back-projections. Compared with (16), (23) and (29) have an additional factor 1/2. This is because the planar measurement configuration can cover a solid angle of up to 2π only while the other two configurations can cover a full 4π solid angle.

IV. NUMERICAL EXPERIMENTS

Now we want to conduct some numerical experiments to demonstrate the validity of the above time-domain reconstruction formulas for thermoacoustic imaging.
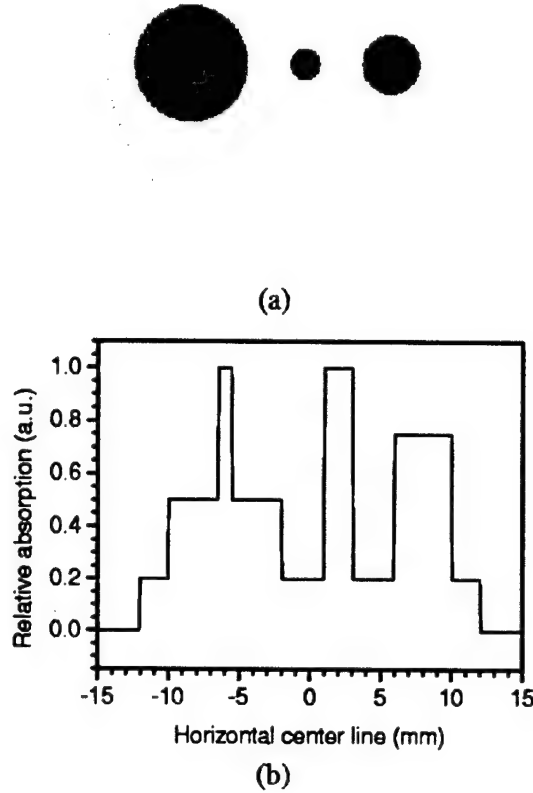

(a)

(b)

Fig. 2. Original sample. (a) Cross-sectional image. (b) Profile along the horizontal center line.

We consider uniform spherical absorbers surrounded by a nonabsorbing background medium. For convenience, we use the centers of the absorbers to denote their positions. The uniform spherical absorber can be written as $A(\mathbf{r}) = A_0 U(a - |\mathbf{r} - \mathbf{r}_a|)$, where A_0 is the absorption intensity, and a and $\mathbf{r}_a$ are the radius and the center of the sphere, respectively. As shown in Fig. 2(a), assume a sample contains five spherical absorbers with different absorption intensities and the centers of these spheres lie in a line parallel to the x axis. For convenience, we call this line the horizontal center line. As shown in Fig. 2(b), from the smallest to the biggest, the radii are 0.5, 1, 2, 4, and 12 mm, respectively, and the relative absorption intensities are 1, 1, 0.75, 0.5, and 0.2, respectively. We also assume that the RF pulse duration is very short and can be regarded as a delta function, and, consequently, that the thermoacoustic signal $p(\mathbf{r}_0, t)$ irradiated from a uniform sphere can be calculated by $\eta c^2 U(a - |R - ct|)(R - ct)/(2R)$, where R is the distance between the detection position $\mathbf{r}_0$ and the absorber center $\mathbf{r}_a$ ($R = |\mathbf{r}_0 - \mathbf{r}_a|$) [23]. The quantity $\partial p(\mathbf{r}_0, t)/\partial t$ in the reconstruction formulas (16), (23), and (29) can be calculated through the Fourier transform

$$\frac{\partial p(\mathbf{r}_0, t)}{\partial t} = \text{IFFT}\{-i\omega p(\mathbf{r}_0, \omega) W_\Omega(\omega)\} \tag{30}$$

where IFFT denotes the inverse fast Fourier transform, $W_\Omega(\omega)$ is a window function, and the Fourier transform defines

$$\bullet(\omega) = \int\limits_{-\infty}^{+\infty} \bullet(t) \exp(i\omega t) dt. \tag{31}$$

As we discussed in [6], the factor ω in (30) actually represents a pure ramp filter, which will significantly depress the low-frequency signal. It is helpful for guaranteeing the validity of the reconstruction (16), (23), and (29). It also indicates that the relatively high-frequency component of the signals play the primary role in the restoration of the RF absorption distribution inside the tissue. But, the ramp filter can also amplify the high-frequency noise in such a way that the reconstructed image is not acceptable from the physical point of view. In order to avoid this effect, it is necessary to introduce a relatively low-pass filter $W_\Omega(\omega)$ characterized by a cutoff angular frequency $\Omega = 2\pi f_\Omega$. A Hanning window is our choice in this case

$$W_\Omega(\omega) = \begin{cases} 0.5 + 0.5 \cos\left(\pi \frac{\omega}{\Omega}\right), & \text{if } |\omega| < \Omega, \\ 0, & \text{otherwise.} \end{cases} \tag{32}$$

In addition, $W_\Omega(\omega)$ also reflects the limited bandwidth of the detected thermoacoustic signals that is due to the finite bandwidth of the detector. We assume the thermoacoustic waves to be in a frequency range below 4 MHz, and choose $f_\Omega = 4\,\text{MHz}$; then the dominative frequency in $\omega W_\Omega(\omega)$ is 1.7 MHz. Here, the data sampling frequency is 20 MHz.

A. Planar Measurement Configuration

We use the planar measurement configuration as shown in Fig. 1(a). Assume that the measurement area is 120 mm × 120 mm in the $z = 0$ plane and that the thermoacoustic signals are collected at 3600 total detection positions that are evenly distributed in the measurement area. Such a measurement can be realized by using a rectangular ultrasonic array or by scanning a linear array or even by scanning a single detector to cover the measurement area. The center of the measurement area is (0, 0, 0). The sample center (0, 0, 30) lies 30 mm above the measurement area. Fig. 3(a) shows the reconstructed RF absorption distribution of the $z = 30\,\text{mm}$ plane, and Fig. 3(b) shows the comparison of the original and reconstructed absorption profiles along the horizontal center line.

B. Cylindrical Measurement Configuration

We employ the cylindrical measurement configuration as shown in Fig. 1(b). Assume the measurement area is a cylindrical surface with a length of 90 mm and a radius of 50 mm. One can use a linear ultrasound array, which is vertically placed and has 30 elements evenly distributed a length of 90 mm, to horizontally scan the sample, with a step size of 3° to cover the measurement area. One can also vertically scan a circular ultrasound array with a step size of 3 mm, where the circular array may have 120 elements evenly distributed in the array. In these ways, the measurement covers 3600 detection positions, which are approximately evenly distributed in the measurement area. The sample center lies at (0, 0, 0), the center of the measurement cylindrical surface. Fig. 4(a) shows the reconstructed RF absorption distribution in the $z = 0\,\text{mm}$
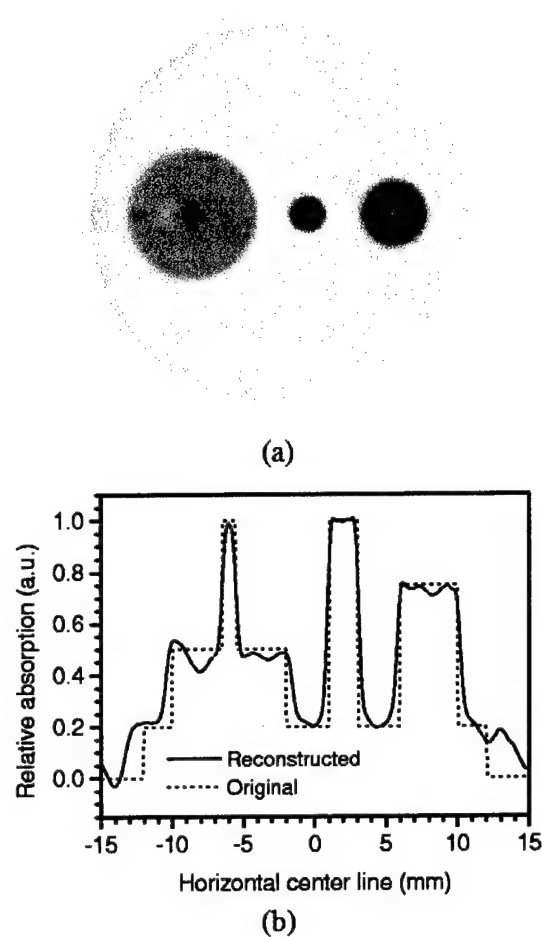

(a)

(b)

Fig. 3. Reconstructed image from planar measurement configuration using 3600 detector positions with high cutoff frequency 4 MHz. (a) Cross-sectional image at the $z = 30\,\text{mm}$ plane. (b) Comparison of the original and reconstructed absorption profiles along the horizontal center line.

plane and Fig. 4(b) shows the comparison of the original and reconstructed absorption profiles along the horizontal center line.

C. Spherical Measurement Configuration

Fig. 1(c) shows the spherical measurement configuration. To simulate a practical condition, we adopt only a half-spherical measurement area in the upper half space $(z > 0)$. Suppose a quarter circular array has 30 elements and the radius of the array is 50 mm. Then one can rotationally scan the array along its radius with a step size of 3° to cover a half spherical measurement area. In this way, the, the measurement contains 3600 detection positions, which are approximately evenly distributed in the measurement area. The sample center lies (0, 0, 12 mm) inside the measurement surface. Fig. 5(a) shows the reconstructed RF absorption distribution of the $z = 12\,\text{mm}$ plane, and Fig. 5(b) shows the comparison of the original and reconstructed absorption profiles along the horizontal center line.

The above examples demonstrate the performance of the time-domain formulas for different measurement configurations. The reconstructed profiles are in good agreement with the original distributions. As mentioned before, with a cutoff
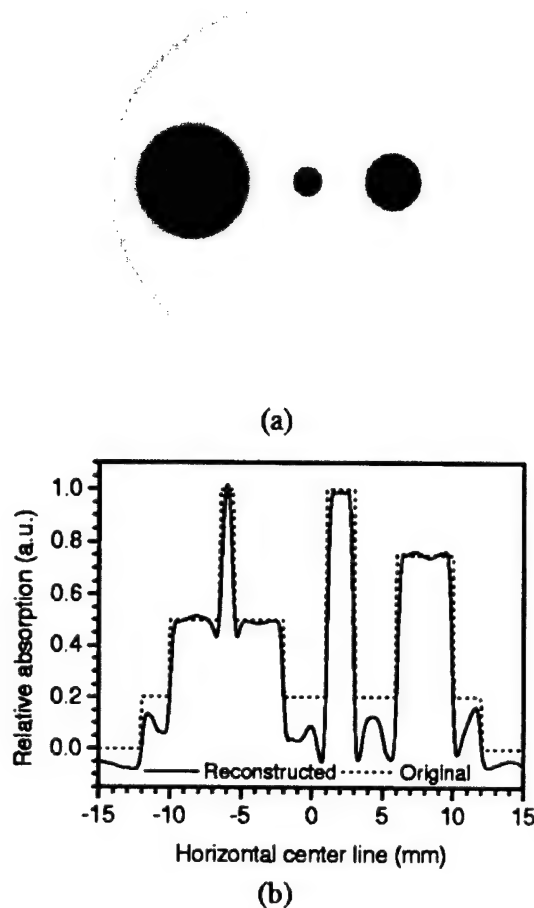
(a)

(b)

Fig. 4. Reconstructed image from cylindrical configuration using 3600 detector positions with high cutoff frequency 4 MHz. (a) Cross-sectional image at the $z = 0$ mm plane. (b) Comparison of the original and reconstructed absorption profiles along the horizontal center line.

(a)

(b)

Fig. 5. Reconstructed image from spherical measurement configuration using 3600 detector positions with high cutoff frequency 4 MHz. (a) Cross-sectional image at the $z = 12$ mm plane. (b) Comparison of the original and reconstructed absorption profiles along the horizontal center line.

frequency $f_\Omega = 4$ MHz, the dominative frequency in $\omega W_\Omega(\omega)$ is 1.7 MHz, which corresponds to an acoustic wavelength of 0.9 mm. That explains why the small absorbers, as well as the boundaries of the big absorbers, can be faithfully reconstructed. As predicted, the flat bases of the big absorbers are not faithfully recovered, which results from the approximations of the algorithms.

However, in the absence of a high-frequency signal, the small size structure will be lost. For example, if the cutoff frequency $f_\Omega = 1.5$ MHz, the dominative frequency in $\omega W_\Omega(\omega)$ is about 0.6 MHz, which corresponds to an acoustic wavelength of 2.5 mm. Without loss of generality, we will take the spherical measurement configuration as an example. The other parameters in the numerical experiment are the same as the example shown in Fig. 5. As shown in Fig. 6, not only is the small absorber nearly corrupted, but also the originally sharp borders of the big absorbers are greatly degraded.

Only a small number of detector positions affect the reconstructed images. We will again take the spherical measurement configuration as an example. Suppose a quarter circular array has only eight elements and the radius of the array is 50 mm.
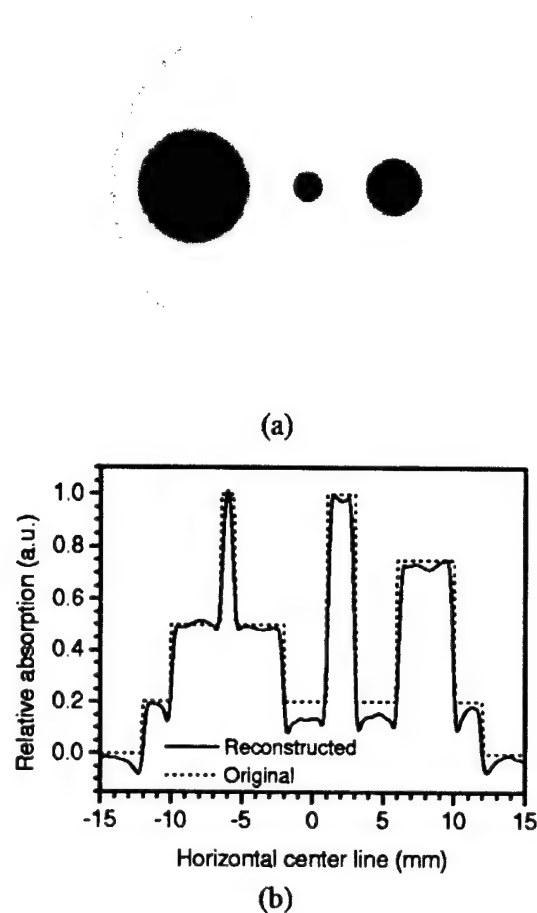
One must rotationally scan the array along its radius with a step size of 11.25° to cover a half spherical measurement area. The other parameters in the numerical experiment are the same as in the example shown in Fig. 5. In this way, the measurement has only 256 detection positions. As shown in Fig. 7, the main structure of the sample is recovered in the reconstructed image, but a lot of noisy artifacts occur.

In addition, the signal-to-noise ratio (SNR) should be carefully considered in thermoacoustic imaging, since the amplitude of the thermoacoustic signal is small as was mentioned in Section I. In general, white noise can be suppressed by averaging over many identical data acquisitions. Denoising can also be accomplished with more elaborate methods including Fourier-based filtering and wavelet-based filtering [25]. Fortunately, reconstruction in thermoacoustic imaging is a linear addition process as shown in (16), (23), and (29). The white noise in each detector is independent of every other. If there are n detectors, the SNR in the image will be improved by the square root of n times through summation of the data. Of course, more detectors and more data acquisitions will increase the cost of the data acquisition time as well as the detection equipment. Actu-
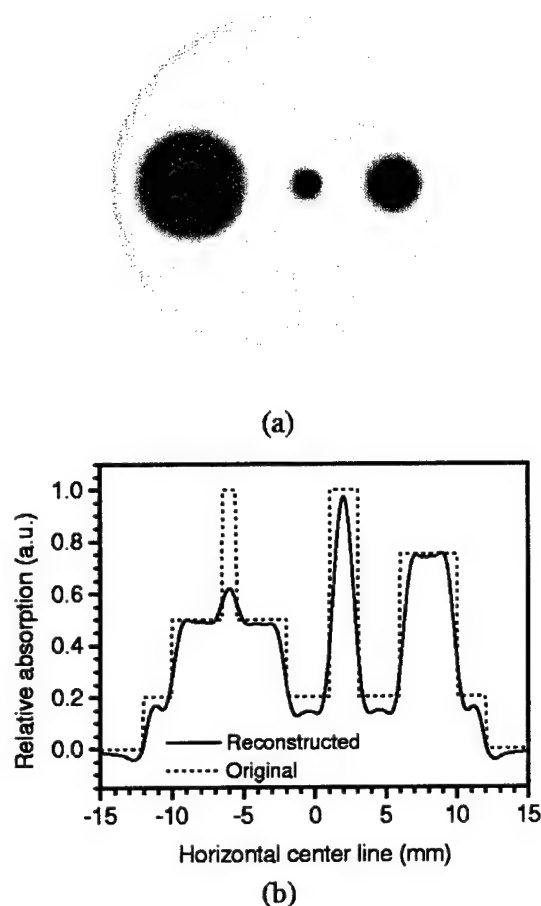
(a)

(b)

Fig. 6. Reconstructed image from spherical measurement configuration using 3600 detector positions with high cutoff frequency 1.5 MHz. (a) Cross-sectional image at the $z = 12$ mm plane. (b) Comparison of the original and reconstructed absorption profiles along the horizontal center line.
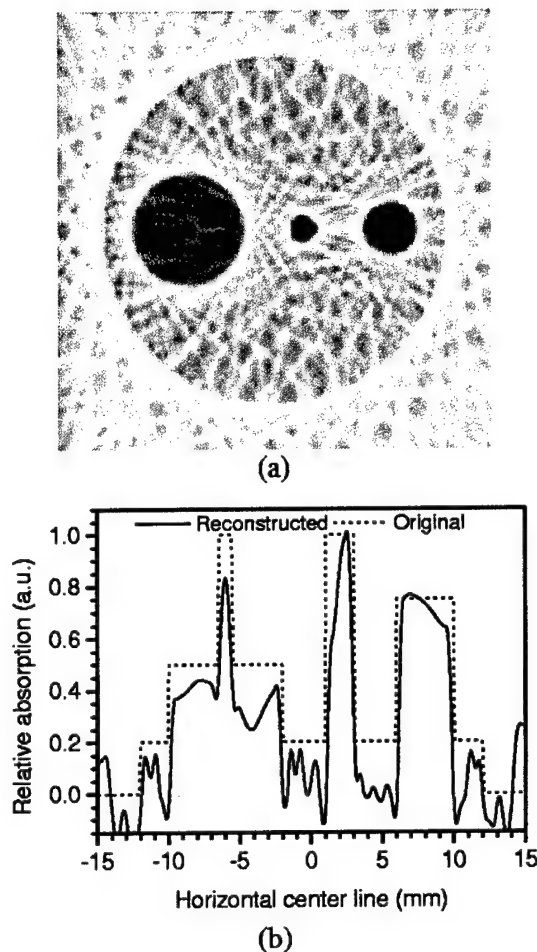

(a)

(b)

Fig. 7. Reconstructed image from spherical measurement configuration using 256 detector positions with high cutoff frequency 4 MHz. (a) Cross-sectional image at the $z = 12$ mm plane. (b) Comparison of the original and reconstructed absorption profiles along the horizontal center line.

ally, as with other imaging modalities, such as magnetic resonance imaging, there is a tradeoff between SNR and the cost of data acquisition time and equipment.

In the above simulations, we consider the point-detectors. In fact, a finite detector area will limit the lateral spatial resolution and affect the axial resolution slightly [6]. A complete analytical explanation of spatial resolution related to bandwidth and detector aperture size will be reported in another paper [26].

V. PRACTICAL APPLICATIONS

The time-domain reconstruction formulas—termed modified back projections—can be derived under the practical conditions discussed above. We have shown that modified back projection formulas closely approximate the rigorous formulas under the above conditions. Unlike the filtered back projection algorithm used in X-ray tomography, which uses the surface integration over intersecting planes, the modified formulas in our problems are calculated through temporal back projection and coherent summation over spherical surfaces with certain spatial weighting factors. Fortunately, due to the advantage of coherent summation, these formulas are still applicable to practical con-

ditions with a finite extension or partial enclosure even though they are derived from idealized recording surfaces. Of course, finite recording surfaces only provide limited spatial views, but that is adequate in practical applications.

The planar, spherical, and cylindrical recording surfaces may cover most measurement configurations. Among them the planar measurement geometry may be the easiest to implement. A two-dimensional (2-D) planar ultrasonic transducer array can be used to detect the thermoacoustic signals as in conventional ultrasound imaging. For example, Hoelen *et al.* [10] used this kind of recording geometry in their photoacoustic imaging. They adopted a delay-and-sum algorithm with experiential weighting factors, which worked well in dealing with their experimental data. Our research shows that the spatial weighting factor $[n, n_0]$ does exist in the back projection formula of (16) for the planar recording configuration. This is an interesting result in our theoretical analysis, which indicates that (16) should be a more accurate form than the one used by Hoelen *et al.*.

The spherical recording configuration may be more suitable for external organ imaging such as breast cancer detection where

in practice, only a semispherical measurement surface can be implemented. For example, Kruger *et al.* employed this kind of measurement geometry [7]. In their experimental system, multiple discrete transducers were mounted on a hemispherical bowl and could scan nearly a 2π solid angle surrounding the breast volume. In the data processing, they assumed that the size of a typical absorbing object was much smaller than the detecting distance, and that the spherical surface, on which the surface integral was computed, approximated a plane. Therefore, the inverse Radon transform was approximately used to reconstruct the image as in X-ray tomography. Obviously, the above far-field condition is not strict, especially when the absorption source is far away from the center of the spherical geometry and results in reconstruction artifacts. Our theoretical analysis gives a more reasonable reconstruction formula (29), which can improve the quality of the reconstructed images.

The cylindrical recording configuration partially combines the properties of planar geometry and of spherical geometry. The reconstruction formula (23) shows a spatial weighting factor $[\mathbf{n}, \mathbf{n}_0] \leq 1$, which is dependent on $|z - z_0|$. The weighting factor reaches the maximum value $[\mathbf{n}, \mathbf{n}_0] = 1$ at $z = z_0$, which indicates that the cross-sectional image of any z_0 plane is primarily determined by the data measured on the circle of the same plane. For example, if some small strong absorption sources at a size of several millimeters lie on the z_0 plane inside a weak absorption background at a size of several centimeters in diameter, a set of circular measurement data detected on a circle with a radius of several centimeters on the z_0 plane would be sufficient to yield a good cross-sectional image. In our initial work [5], [6], we used this kind of circular measurement to investigate some phantom samples and the reconstructed images agreed with the samples very well. But, if there are other absorbers outside the z_0 plane, the thermoacoustic signals from these absorbers also reach the detectors in the z_0 plane. Thus, a set of circular measurement data on the z_0 plane only could not distinguish between the absorbers on or outside of the plane. In this case, three-dimensional measurement and reconstruction must be used.

In fact, the choice of measurement configuration depends on the practical needs. From the physical point of view, these reconstruction formulas, (16), (23), and (29) for planar, cylindrical, and spherical configurations, respectively, are the same, except that the spatial weighting factors resulted from the measurement geometries. In addition, the weighting factors in the above equations are obtained through first-order approximations. In principle, high-order approximations can be derived.

Finally, it has to be pointed out that an inhomogeneous acoustic property, such as the speed of sound variation, might blur the reconstructed images. The experiments as shown in [5] and [6] demonstrated that the small speed variations between fat and muscle or gelatin did not result in significant reconstruction artifacts. The reason is that thermoacoustic waves are produced internally by RF absorption and are propagated one-way to the detectors. Thus, a small speed variation does not affect the travel time of the sound very much in a finite-length path, for example, 10 cm, which is a typical breast diameter. Therefore, in thermoacoustic tomography, satisfactory contrast

and resolution are obtainable even in tissue with a small degree of acoustic inhomogeneity.

VI. CONCLUSION

In this paper, we have presented time-domain reconstruction algorithms for the thermoacoustic imaging of biological tissues. They are computed through temporal back projections and coherent summations over spherical surfaces with certain spatial weighting factors. Numerical experiments have demonstrated the validity of their applications. These formulas (or high-order approximations of the rigorous reconstruction formulas) can serve as the basis for time-domain thermoacoustic or photoacoustic imaging in biological tissues.

APPENDIX A

The delta function can be written in the Cartesian coordinates as

$$\delta(\mathbf{r} - \mathbf{r}_0) = \delta(x - x_0)\delta(y - y_0)\delta(z). \tag{A1}$$

Taking Fourier transforms on both sides of (8) on variables x, y, and z, it can be shown that the Green's function is a triple Fourier integral of (11). If the recording surface S_0 is infinite, we may take 2–D Fourier transforms on x_0 and y_0 of $\widetilde{p}(x_0, y_0, k)$, i.e., multiplying both sides of (7) by $\exp(iux_0 + ivy_0)$ and integrating with respect to x_0 and y_0 from $-\infty$ to $+\infty$, one gets

$$\iint\limits_{-\infty}^{+\infty} dx_0 dy_0 \exp(iux_0 + ivy_0)\widetilde{p}(x_0, y_0, k)$$

$$= \frac{-ikc^2\eta}{2\pi} \int\limits_{0}^{+\infty} dz \iint\limits_{-\infty}^{+\infty} dx dy A(x, y, z) \exp(iux + ivy)$$

$$\cdot \int\limits_{-\infty}^{+\infty} dK_z \frac{\exp(-iK_z z)}{K_z^2 + \rho^2 - k^2} \tag{A2}$$

where $\rho = \sqrt{u^2 + v^2}$, $(\rho \geq 0)$.

The integral of the far right of (A2) can be computed by the contour integration $(z > 0)$, because there will always be some damping of the wave in a physical system [22], [24]

$$\int\limits_{-\infty}^{+\infty} dK_z \frac{\exp(-iK_z z)}{K_z^2 + \rho^2 - k^2}$$

$$= \begin{cases} i\pi \mathrm{sgn}(k) \dfrac{\exp\left[iz\,\mathrm{sgn}(k)\sqrt{k^2 - \rho^2}\right]}{\sqrt{k^2 - \rho^2}}, & |k| > \rho \\[3mm] -\pi \dfrac{\exp\left[-z\sqrt{\rho^2 - k^2}\right]}{\sqrt{\rho^2 - k^2}}, & |k| < \rho \end{cases} \tag{A3}$$

where $\mathrm{sgn}(k) = 1$ for $k \geq 0$ and $\mathrm{sgn}(k) = -1$ for $k < 0$.

Here, we use the values of k for $|k| > \rho$ to do the reconstruction. Those of k for $|k| < \rho$ correspond to evanescent waves and will have no contribution to the reconstruction.

In the case $|k| > \rho$ and $z > 0$, (A2) becomes

$$
\iint\limits_{-\infty}^{+\infty} dx_0 dy_0 \exp(iux_0 + ivy_0) \frac{2}{kc^2\eta} \widetilde{p}(x_0, y_0, k)
$$

$$
= \int\limits_{0}^{+\infty} dz \iint\limits_{-\infty}^{+\infty} dxdy A(x, y, z) \exp(iux + ivy)
$$

$$
\cdot \operatorname{sgn}(k) \frac{\exp\left[iz\operatorname{sgn}(k)\sqrt{k^2-\rho^2}\right]}{\sqrt{k^2-\rho^2}}. \tag{A4}
$$

Multiplying both sides of (A4) by $\exp(-iux' - ivy')$ and integrating with respect to u and v letting ρ from 0 to $|k|$, and further multiplying both sides of (A4) by $k\exp\lfloor -iz'\operatorname{sgn}(k)\sqrt{k^2-\rho^2}\rfloor$ and integrating with respect to k from $-\infty$ to $+\infty$, gives

$$
\iint\limits_{-\infty}^{+\infty} dx_0 dy_0 \int\limits_{-\infty}^{+\infty} dk \iint\limits_{\rho=0}^{\rho=|k|} dudv
$$

$$
\times \exp[iu(x_0 - x')] \exp[iv(y_0 - y')]
$$

$$
\cdot \frac{2\widetilde{p}(x_0, y_0, k)}{kc^2\eta} k \exp\left[-iz'\operatorname{sgn}(k)\sqrt{k^2-\rho^2}\right]
$$

$$
= \int\limits_{0}^{+\infty} dz \iint\limits_{-\infty}^{+\infty} dxdy A(x, y, z)
$$

$$
\cdot \int\limits_{-\infty}^{+\infty} kdk\operatorname{sgn}(k) \frac{\exp\left[i(z-z')\operatorname{sgn}(k)\sqrt{k^2-\rho^2}\right]}{\sqrt{k^2-\rho^2}}
$$

$$
\cdot \iint\limits_{\rho=0}^{\rho=|k|} dudv \exp[iu(x-x')] \exp[iv(y-y')]. \tag{A5}
$$

Rearranging the orders of integration of the right-hand side of (A5), we get

$$
\text{right} = \int\limits_{0}^{+\infty} dz \iint\limits_{-\infty}^{+\infty} dxdy A(x, y, z) \iint\limits_{-\infty}^{+\infty} dudv
$$

$$
\times \exp[iu(x-x')] \exp[iv(y-y')]
$$

$$
\cdot \left[\int\limits_{\rho}^{+\infty} kdk \frac{\exp\left[i(z-z')\sqrt{k^2-\rho^2}\right]}{\sqrt{k^2-\rho^2}} \right.
$$

$$
\left. + \int\limits_{-\infty}^{-\rho} kdk \frac{\exp\left[-i(z-z')\sqrt{k^2-\rho^2}\right]}{-\sqrt{k^2-\rho^2}} \right]. \tag{A6}
$$

If we let $w = \operatorname{sgn}(k)\sqrt{k^2-\rho^2}$, (A6) reduces to

$$
\text{right} = \int\limits_{0}^{+\infty} dz \iint\limits_{-\infty}^{+\infty} dxdy A(x, y, z) \cdot \iiint\limits_{-\infty}^{+\infty} dudvdw
$$

$$
\times \exp[iu(x-x')] \exp[iv(y-y')] \exp[i(z-z')w]
$$

$$
= \int\limits_{0}^{+\infty} dz \iint\limits_{-\infty}^{+\infty} A(x, y, z) dxdy
$$

$$
\cdot (2\pi)^3 \delta(x-x')\delta(y-y')\delta(z-z')
$$

$$
= (2\pi)^3 A(x', y', z'). \tag{A7}
$$

Then, substituting (A7) into (A5) and dropping the primes, we get (12) and (13).

Next, we want to show that under certain practical conditions, (12) reduces to a modified back projection formula. Replacing K_x and K_y in (11) with u and v, and then taking complex conjugates of (11) and (A3), one gets

$$
\widetilde{G}_k^*(\mathbf{r}, \mathbf{r}_0) = \frac{1}{(2\pi)^3} \iint\limits_{-\infty}^{+\infty} dudv \exp[iu(x_0 - x) + iv(y_0 - y)]
$$

$$
\cdot \int\limits_{-\infty}^{+\infty} dK_z \frac{\exp(iK_z z)}{K_z^2 + \rho^2 - k^2} \tag{A8}
$$

and

$$
\int\limits_{-\infty}^{+\infty} dK_z \frac{\exp(iK_z z)}{K_z^2 + \rho^2 - k^2}
$$

$$
= \begin{cases} -i\pi\operatorname{sgn}(k) \\ \quad \times \dfrac{\exp\left[-iz\operatorname{sgn}(k)\sqrt{k^2-\rho^2}\right]}{\sqrt{k^2-\rho^2}}, & |k| > \rho, \\ -\pi \dfrac{\exp\left[-z\sqrt{\rho^2-k^2}\right]}{\sqrt{\rho^2-k^2}}, & |k| < \rho. \end{cases} \tag{A9}
$$

Then, substituting (A9) into (A8), taking the first derivative on variable z of (A8) and then making a comparison with (13), one finds

$$
\frac{\partial}{\partial z}\widetilde{G}_k^*(\mathbf{r}, \mathbf{r}_0) = -\frac{\pi c^2\eta}{2}\widetilde{K}_k(\mathbf{r}_0, \mathbf{r}) + \widetilde{\varepsilon}_k(\mathbf{r}_0, \mathbf{r}), \tag{A10}
$$

where

$$
\widetilde{\varepsilon}_k(\mathbf{r}, \mathbf{r}_0) = \frac{1}{8\pi^2} \iint\limits_{\rho=|k|}^{\rho=+\infty} dudv \exp[iu(x_0 - x)]
$$

$$
\times \exp[iv(y_0 - y)]
$$

$$
\cdot \exp\left[-z\sqrt{\rho^2-k^2}\right]. \tag{A11}
$$

If letting $u = \rho\cos\psi$, $v = \rho\sin\psi$, $x_0 - x = R\cos\alpha$, and $y_0 - y = R\sin\alpha$, where $\rho = \sqrt{u^2 + v^2}$ and $R = \sqrt{(x_0 - x)^2 + (y_0 - y)^2}$, through changing the variables of integration, using the identity

$$
\frac{1}{2\pi}\int\limits_{0}^{2\pi} d\phi \exp[i\rho\phi\cos(\phi-\alpha)] = J_0(\rho R) \tag{A12}
$$

one can rewrite (A11) as

$$
\widetilde{\varepsilon}_k(\mathbf{r}, \mathbf{r}_0) = \frac{1}{4\pi}\int\limits_{|k|}^{+\infty} \rho d\rho J_0(\rho R)\exp\left[-z\sqrt{\rho^2-k^2}\right]. \tag{A13}
$$

As [24] shows

$$
|\widetilde{\varepsilon}_k(\mathbf{r}, \mathbf{r}_0)| \leq |\widetilde{\varepsilon}_0(\mathbf{r}, \mathbf{r}_0)| = \frac{1}{4\pi}\int\limits_{0}^{+\infty} \rho d\rho J_0(\rho R)\exp(-z\rho)
$$

$$
= \frac{z}{4\pi(z^2 + \rho^2)^{\frac{3}{2}}}
$$

$$
= \frac{z}{4\pi|\mathbf{r} - \mathbf{r}_0|^3}. \tag{A14}
$$

However

$$\frac{\partial}{\partial z}\widetilde{G}_k^*(\mathbf{r},\mathbf{r}_0) = \frac{\partial}{\partial z}\left[\frac{\exp(-ik|\mathbf{r}-\mathbf{r}_0|)}{4\pi|\mathbf{r}-\mathbf{r}_0|}\right]$$

$$= \frac{-z}{|\mathbf{r}-\mathbf{r}_0|}\left(\frac{1}{|\mathbf{r}-\mathbf{r}_0|}+ik\right)\widetilde{G}_k^*(\mathbf{r},\mathbf{r}_0). \quad (A15)$$

Therefore, under the condition $|k||\mathbf{r}-\mathbf{r}_0| \gg 1$, one gets

$$\left|\frac{\partial}{\partial z}\widetilde{G}_k^*(\mathbf{r},\mathbf{r}_0)\right| > \frac{z|k|}{4\pi|\mathbf{r}-\mathbf{r}_0|^2} \gg \frac{z}{4\pi|\mathbf{r}-\mathbf{r}_0|^3} \ge |\widetilde{\varepsilon}_k(\mathbf{r},\mathbf{r}_0)|. \quad (A16)$$

This means that the evanescent contribution $\widetilde{\varepsilon}$ is negligible when $|k||\mathbf{r}-\mathbf{r}_0| \gg 1$ holds. Then, from (A10), we get

$$\widetilde{K}_k(\mathbf{r}_0,\mathbf{r}) \approx -\frac{2}{\pi c^2\eta}\frac{\partial}{\partial z}\widetilde{G}_k^*(\mathbf{r},\mathbf{r}_0) \approx \frac{i2k}{\pi c^2\eta}\frac{z}{|\mathbf{r}-\mathbf{r}_0|}\widetilde{G}_k^*(\mathbf{r},\mathbf{r}_0). \quad (A17)$$

APPENDIX B

The delta function can be expressed in the circular cylindrical coordinates [22]

$$\delta(\mathbf{r}-\mathbf{r}_0) = \frac{1}{\rho}\delta(\rho-\rho_0)\delta(\varphi-\varphi_0)\delta(z-z_0)$$

$$= \frac{1}{\rho}\delta(\rho-\rho_0)\frac{1}{2\pi}\sum_{m=-\infty}^{+\infty}\exp[im(\varphi-\varphi_0)]$$

$$\cdot\frac{1}{2\pi}\int_{-\infty}^{+\infty}\exp[ik_z(z-z_0)]\,dk_z. \quad (B1)$$

Assuming a similar expansion of the Green's function as

$$\widetilde{G}_k(\mathbf{r},\mathbf{r}_0) = \frac{1}{4\pi^2}\sum_{m=-\infty}^{+\infty}\exp[im(\varphi-\varphi_0)]$$

$$\int_{-\infty}^{+\infty}dk_z\exp[ik_z(z-z_0)]\cdot g_{mk}(\rho,\rho_0,k_z). \quad (B2)$$

Substituting (B1) and (B2) into (8), we get

$$\rho^2\frac{d^2g_{mk}}{d\rho^2}+\rho\frac{dg_{mk}}{d\rho}+\left[(k^2-k_z^2)\rho^2-m^2\right]g_{mk} = -\rho\delta(\rho-\rho_0). \quad (B3)$$

For the $k > 0$ case, by letting $\mu = \sqrt{k^2-k_z^2}$, one obtains

$$g_{mk}(\rho,\rho_0,k_z) = \frac{i\pi}{2}J_m(\mu\rho)H_m^{(1)}(\mu\rho_0) \quad (B4)$$

where if $k_z^2 > k^2$, $g_{mk}(\rho,\rho_0,k_z) = I_m(-i\mu\rho)K_m(-i\mu\rho_0)$ with $\mu = i\sqrt{k_z^2-k^2}$. Therefore, (7) can be expressed in the following form:

$$\frac{\widetilde{p}(\mathbf{r}_0,k)}{-ikc^2\eta} = \frac{1}{4\pi^2}\int\int\int_V d^3rA(\mathbf{r})\sum_{m=-\infty}^{+\infty}\exp[im(\varphi-\varphi_0)]$$

$$\cdot\int_{-\infty}^{+\infty}dk_z\exp[ik_z(z-z_0)]g_{mk}(\rho,\rho_0,k_z). \quad (B5)$$

For the idealized cylindrical recording geometry, $\widetilde{p}(\mathbf{r}_0,k)$ is a periodical function of angular variable φ_0 with a 2π period

and its extent along z is infinite. Therefore, we may take a series expansion of the recorded data on variable φ_0 and a 1-D Fourier transform on variable z_0. Multiplying both sides of (B5) by $\exp(i\gamma z_0)$ and integrating with respect to z_0 from $-\infty$ to $+\infty$, and further multiplying both sides by $\exp(in\varphi_0)$ and integrating with respect to φ_0 from 0 to 2π, one obtains

$$\int_0^{2\pi}d\varphi_0\int_{-\infty}^{+\infty}dz_0\frac{\widetilde{p}(\mathbf{r}_0,k)}{-ikc^2\eta}\exp(in\varphi_0)\exp(i\gamma z_0)$$

$$= \frac{1}{4\pi^2}\int\int\int_V d^3rA(\mathbf{r})\sum_{m=-\infty}^{+\infty}\exp(im\varphi)$$

$$\times\int_0^{2\pi}d\varphi_0\exp[i(n-m)\varphi_0]$$

$$\cdot\int_{-\infty}^{+\infty}dk_z\exp(ik_zz)g_{mk}(\rho,\rho_0,k_z)$$

$$\times\int_{-\infty}^{+\infty}dz_0\exp[i(\gamma-k_z)\varphi_0]$$

$$= \frac{1}{4\pi^2}\int\int\int_V d^3rA(\mathbf{r})\sum_{m=-\infty}^{+\infty}\exp(im\varphi)2\pi\delta_{nm}$$

$$\cdot\int_{-\infty}^{+\infty}dk_z\exp(ik_zz)g_{mk}(\rho,\rho_0,k_z)2\pi\delta(\gamma-k_z)$$

$$= \int\int\int_V d^3rA(\mathbf{r})\exp(in\varphi)$$

$$\times\exp(i\gamma z)g_{nk}(\rho,\rho_0,\gamma). \quad (B6)$$

Here we use the values of k for $\gamma^2 < k^2$ to do the reconstruction. Those values of k for which $\gamma^2 > k^2$ represent the evanescent waves play no role in the reconstruction. In the case of $\gamma^2 < k^2$, we can rewrite (B6) as

$$\int_0^{2\pi}d\varphi_0\int_{-\infty}^{+\infty}dz_0\frac{2}{\pi}\frac{\widetilde{p}(\mathbf{r}_0,k)}{kc^2\eta}$$

$$\times\exp(in\varphi_0)\exp(i\gamma z_0) = \int\int\int_V d^3rA(\mathbf{r})\exp(in\varphi)$$

$$\times\exp(i\gamma z)J_n(\mu\rho)$$

$$\times H_n^{(1)}(\mu\rho_0). \quad (B7)$$

Multiplying both sides of (B7) by $\mu J_n(\mu\rho')/H_n^{(1)}(\mu\rho_0)$ and integrating them with respect to μ from 0 to $+\infty$, then multiplying both sides by $\exp(-in\varphi')$ and summing n from $-\infty$ to $+\infty$, and further multiplying both sides by $\exp(-i\gamma z')$ and integrating them with respect to γ from $-\infty$ to $+\infty$, one gets

$$\int_0^{2\pi}d\varphi_0\int_{-\infty}^{+\infty}dz_0\int_{-\infty}^{+\infty}d\gamma\exp[i\gamma(z_0-z')]\int_0^{+\infty}\mu d\mu\frac{2}{\pi}\frac{\widetilde{p}(\mathbf{r}_0,k)}{kc^2\eta}$$

$$\cdot\sum_{n=-\infty}^{+\infty}\exp[in(\varphi_0-\varphi')]\frac{J_n(\mu\rho')}{H_n^{(1)}(\mu\rho_0)}$$

$$= \int_{-\infty}^{+\infty} dz \int_0^{\rho_0} \rho d\rho \int_0^{2\pi} d\varphi A(\mathbf{r}) \int_0^{+\infty} d\gamma \exp\left[i\gamma(z - z')\right]$$

$$\cdot \sum_{n=-\infty}^{+\infty} \exp\left[in(\varphi - \varphi')\right] \int_0^{+\infty} \mu d\mu J_n(\mu\rho) J_n(\mu\rho')$$

$$= \int_{-\infty}^{+\infty} dz \int_0^{\rho_0} \rho d\rho \int_0^{2\pi} d\varphi A(\mathbf{r}) \cdot 2\pi\delta(z - z')$$

$$\cdot 2\pi\delta(\varphi - \varphi') \cdot \frac{\delta(\rho - \rho')}{\rho}$$

$$= (2\pi)^2 A(\rho', \varphi', z'). \tag{B8}$$

By dropping the primes, changing the integral variable from μ to k according to $\mu = \sqrt{k^2 - \gamma^2}$ and rearranging the orders of the integration, one can rewrite the (B8) as

$$A(\rho, \varphi, z) = \frac{1}{2\pi^3} \int_0^{2\pi} d\varphi_0 \int_{-\infty}^{+\infty} dz_0 \int_{-\infty}^{+\infty} d\gamma \int_{+|\gamma|}^{+\infty} k dk \frac{\widetilde{p}(\mathbf{r}_0, k)}{kc^2\eta}$$

$$\cdot \sum_{n=-\infty}^{+\infty} \exp\left[in(\varphi_0 - \varphi)\right]$$

$$\times \frac{J_n\left(\rho\sqrt{k^2 - \gamma^2}\right)}{H_n^{(1)}\left(\rho_0\sqrt{k^2 - \gamma^2}\right)} \exp\left[i\gamma(z_0 - z)\right]$$

$$= \frac{1}{2\pi^3} \int_0^{2\pi} d\varphi_0 \int_{-\infty}^{+\infty} dz_0 \int_0^{+\infty} dk \frac{\widetilde{p}(\mathbf{r}_0, k)}{c^2\eta}$$

$$\cdot \sum_{n=-\infty}^{+\infty} \exp\left[in(\varphi_0 - \varphi)\right]$$

$$\times \int_{-k}^{+k} d\gamma \frac{J_n\left(\rho\sqrt{k^2 - \gamma^2}\right)}{H_n^{(1)}\left(\rho_0\sqrt{k^2 - \gamma^2}\right)} \exp\left[i\gamma(z_0 - z)\right]. \tag{B9}$$

Equation (B9) can be easily written in the forms of (18) and (19).

Next, we want to show that (18) can be reduced to a modified back projection under certain conditions. When $\xi \gg 1$, according to the asymptotic expansions of the Hankel function, we get

$$H_n^{(1)}(\xi) H_n^{(2)}(\xi) \approx \frac{2}{\pi\xi}. \tag{B10}$$

Assuming $\rho_0\sqrt{k^2 - \gamma^2} \gg 1$, i.e., $\rho_0 k \gg 1$, one can approximate

$$\frac{1}{H_n^{(1)}\left(\rho_0\sqrt{k^2 - \gamma^2}\right)} \approx \frac{\pi}{2}\rho_0\sqrt{k^2 - \gamma^2} H_n^{(2)}\left(\rho_0\sqrt{k^2 - \gamma^2}\right). \tag{B11}$$

Therefore

$$\widetilde{K}_r(\mathbf{r}, \mathbf{r}_0) \approx \frac{1}{4\pi^2 c^2\eta} \sum_{n=-\infty}^{+\infty} \exp\left[in(\varphi_0 - \varphi)\right]$$

$$\times \int_{-k}^{+k} d\gamma \exp\left[i\gamma(z_0 - z)\right]$$

$$\cdot \sqrt{k^2 - \gamma^2} J_n\left(\rho\sqrt{k^2 - \gamma^2}\right)$$

$$\times H_n^{(2)}\left(\rho_0\sqrt{k^2 - \gamma^2}\right). \tag{B12}$$

We can argue that the values of γ for $\gamma^2 > k^2$ do not contribute to the reconstruction. Taking the complex conjugate of the Green's function in (B2) and replacing k_z by γ, we may exclude these γ satisfying $\gamma^2 > k^2$ and approximate the Green's function as

$$\widetilde{G}_k^*(\mathbf{r}, \mathbf{r}_0) \approx -\frac{i}{8\pi} \sum_{n=-\infty}^{+\infty} \exp[in(\varphi_0 - \varphi)] \int_{-k}^{+k} d\gamma \exp\left[i\gamma(z_0 - z)\right]$$

$$\cdot J_n\left(\rho\sqrt{k^2 - \gamma^2}\right) H_n^{(2)}\left(\rho\sqrt{k^2 - \gamma^2}\right). \tag{B13}$$

Letting $z_1 = z_0 - z$, the second-order partial derivative of (B13) with respect to z_1 has the following relation:

$$\frac{\partial^2}{\partial z_1^2} \sim -\gamma^2. \tag{B14}$$

Comparing (B12) with (B13), we get

$$\widetilde{K}_k(\mathbf{r}_0, \mathbf{r}) = \frac{i2k}{\pi c^2\eta} \sqrt{1 + \frac{1}{k^2} \frac{\partial^2}{\partial z_1^2}} \widetilde{G}_k^*(\mathbf{r}, \mathbf{r}_0). \tag{B15}$$

Under the condition $k|\mathbf{r} - \mathbf{r}_0| \gg 1$

$$\frac{1}{k^2} \frac{\partial^2}{\partial z_1^2} \widetilde{G}_k^*(\mathbf{r}, \mathbf{r}_0) = \frac{1}{k^2} \frac{\partial^2}{\partial z_1^2} \left[\frac{\exp\left(-ik|\mathbf{r} - \mathbf{r}_0|\right)}{4\pi|\mathbf{r} - \mathbf{r}_0|}\right]$$

$$\approx -\frac{(z_0 - z)^2}{|\mathbf{r} - \mathbf{r}_0|^2} \widetilde{G}_k^*(\mathbf{r}, \mathbf{r}_0). \tag{B16}$$

Then, (B15) approximates to

$$\widetilde{K}_k(\mathbf{r}, \mathbf{r}_0) \approx \frac{i2k}{\pi c^2\eta} \sqrt{1 - \frac{(z_0 - z)^2}{|\mathbf{r} - \mathbf{r}_0|^2}} \widetilde{G}_k^*(\mathbf{r}, \mathbf{r}_0). \tag{B17}$$

REFERENCES

[1] R. A. Kruger, K. K. Kopecky, A. M. Aisen, D. R. Reinecke, G. A. Kruger, and W. L. Kiser, "Thermoacoustic CT with radio waves: A medical imaging paradigm," *Radiology*, vol. 211, pp. 275–278, 1999.

[2] G. Ku and L.-H. V. Wang, "Scanning thermoacoustic tomography in biological tissues," *Med. Phys.*, vol. 27, pp. 1195–1202, 2000.

[3] ——, "Scanning microwave-induced thermoacoustic tomography: Signal, resolution, and contrast," *Med. Phys.*, vol. 28, pp. 4–10, 2001.

[4] M.-H. Xu, G. Ku, and L.-H. V. Wang, "Microwave-induced thermoacoustic tomography using multi-sector scanning," *Med. Phys.*, vol. 28, pp. 1958–1963, 2001.

[5] M.-H. Xu and L.-H. V. Wang, "Time-domain reconstruction for thermoacoustic tomography in a spherical geometry," *IEEE Med. Imag.*, vol. 21, pp. 814–822, July 2002.

[6] ——, "Pulsed-microwave-induced thermoacoustic tomography: Filtered backprojection in a circular measurement configuration," *Med. Phys.*, vol. 29, pp. 1661–1669, 2002.

[7] R. A. Kruger, D. R. Reinecke, and G. A. Kruger, "Thermoacoustic computed tomography—technical considerations," *Med. Phys.*, vol. 26, pp. 1832–1837, 1999.

[8] R. A. Kruger, K. D. Miller, H. E. Reynolds, W. L. Kiser, Jr, D. R. Reinecke, and G. A. Kruger, "Breast cancer *in vivo*: Contrast enhancement with thermoacoustic CT at 434 MHz—feasibility study," *Radiology*, vol. 216, pp. 279–283, 2000.

[9] P. Y. Liu, "The P-transform and photoacoustic image reconstruction," *Phys. Med. Biol.*, vol. 43, pp. 667–674, 1998.

[10] C. G. A. Hoelen and F. F. M. de Mul, "Image reconstruction for photoacoustic scanning of tissue structures," *Appl. Opt.*, vol. 39, no. 31, pp. 5872–5883, Nov. 2000.

[11] R. O. Esenaliev, A. A. Karabutov, and A. A. Oraevsky, "Sensitivity of laser opto-acoustic imaging in detection of small deeply embedded tumors," *IEEE J. Sel. Top. Quantum Electron.*, vol. 5, pp. 981–988, July-Aug. 1999.

[12] K. P. Kostli, M. Frenz, H. P. Weber, G. Paltauf, and H. Schmidt-Kloiber, "Optoacoustic infrared spectroscopy of soft tissue," *J. Appl. Phys.*, vol. 88, pp. 1632–1637, 2000.

[13] C. C. Johnson and A. W. Guy, "Nonionizing elecromagnetic wave effects in biological materials and systems," *Proc. IEEE*, vol. 60, pp. 692–718, 1972.

[14] F. A. Duck, *Physical Properties of Tissue*. San Diego, CA: Academic, 1990.

[15] V. E. Gusev and A. A. Karabutov, *Laser Optoacoustics*. New York: American Institute of Physics, 1993.

[16] P. N. T. Wells, "Ultrasonic imagining of the human body," *Rep. Prog. Phy.*, vol. 62, pp. 671–722, 1999.

[17] L. V. Zhigilei and B. J. Garrison, "Microscopic mechanisms of laser ablation of organic solids in the thermal and stress confinement irradiation regimes," *J. Appl. Phys.*, vol. 88, pp. 1281–1298, 2000.

[18] Y. V. Zhulina, "Optimal statistical approach to optoacoustic image reconstruction," *Appl. Opt.*, vol. 39, no. 32, pp. 5971–5977, Nov. 2000.

[19] K. P. Kostli, M. Frenz, H. Bebie, and H. P. Weber, "Temporal backward projection of optoacoustic pressure transients using Fourier transform methods," *Phys. Med. Biol.*, vol. 46, pp. 1863–1872, 2001.

[20] Y. Xu, D. Feng, and L.-H. V. Wang, "Exact frequency-domain reconstruction for thermoacoustic tomography-I: Planar geometry," *IEEE Med. Imag.*, vol. 21, pp. 823–828, July 2002.

[21] Y. Xu, M.-H. Xu, and L.-H. V. Wang, "Exact frequency-domain reconstruction for thermoacoustic tomography-II: Cylindrical geometry," *IEEE Med. Imag.*, vol. 21, pp. 829–833, July 2002.

[22] G. B. Arfken and H. J. Weber, *Mathematical Methods for Physicists*. San Diego, CA: Academic, 1995.

[23] G. J. Diebold, T. Sun, and M. I. Khan, "Photoacoustic monopole radiation in one, two, and three dimensions," *Phys. Rev. Lett.*, vol. 67, pp. 3384–3387, 1991.

[24] S. J. Norton and M. Linzer, "Ultrasonic reflectivity imaging in three dimensions: Exact inverse scattering solutions for plane, cylindrical, and spherical apertures," *IEEE Trans. Biomed. Eng.*, vol. BME-28, pp. 202–220, 1981.

[25] *The Image Processing Handbook*, CRC, Boca Raton, FL, 1992.

[26] M.-H. Xu and L.-H. V. Wang, "Analytic explanation of spatial resolution related to bandwidth and detector aperture size in thermoacoustic or photoacoustic reconstruction," *Phys. Rev. E*, vol. 67, no. 056605, 2003.

Minghua Xu received the B.S. degree in physics from Qingdao University of Oceanography, Qingdao, China, in 1994, and the M.S. and Ph.D. degrees in acoustics from Nanjing University, Jiangsu, China, in 1996 and 1999, respectively. He is working towards the Ph.D. degree in biomedical engineering at Texas A&M University, College Station.

His main research topic is biomedical imaging.

Yuan Xu received the B.S. degree in physics from Wuhan University, Wuhan, P. R. China, in 1992, the M.S. degree in physics from Shanghai Institute of Optics and Fine Mechanics, Shanghai, P. R. China, in 1995, and the Ph.D. degree in physics from Institute of Physics, Chinese Academy of Sciences, Beijing, P. R. China, in 1999. He is now a graduate student with the department of Biomedical Engineering in Texas A&M University, College Station.

His special fields of interest are thermoacoustic tomography and ultrasound tomography, and their applications to medical imaging.

Lihong V. Wang (M'96–SM'00) received the Ph.D. degree in electrical engineering from Rice University, Houston, TX, in 1992.

He worked for University of Texas M.D. Anderson Cancer Center, a top-ranked cancer institution, as an Assistant Professor. He was promoted to Professor of Biomedical Engineering and Electrical Engineering at Texas A&M University, College Station, in 2002. His research focus is on nonionizing biophotonic imaging for early cancer detection. His group pioneered acousto-optical tomography, spectroscopic oblique-incidence reflectometry, thermo-acoustic tomography, photo-acoustic tomography, and Mueller-matrix optical coherence tomography. His program for Monte Carlo modeling of photon transport in biological tissues has been used worldwide (available at http://oilab.tamu.edu).

Dr. Wang is a fellow of American Institute for Medical and Biological Engineering, and a member of American Physical Society, Biomedical Engineering Society, Engineering in Medicine and Biology, Society Optical Society of America, and Society of Photo-Optical Instrumentation Engineers. He received the NIH FIRST Award, NSF CAREER Award, Johnson & Johnson Outstanding Young Scientist Award, Texas A&M TEES Select Young Faculty Award, Texas A&M TEES Faculty Fellow Award (twice), Texas A&M Ernest A. Baetz Faculty Fellow Award, Texas A&M TEES Senior Faculty Fellow Award, and Texas A&M University Faculty Fellow. He is listed in *Who's Who in Science and Engineering*. He has been an associate editor for the *Annals of Biomedical Engineering*, *Journal of Biomedical Optics*, and *Applied Optics*.

Effects of Acoustic Heterogeneity in Breast Thermoacoustic Tomography

Yuan Xu and Lihong V. Wang, *Senior Member, IEEE*

Abstract—The effects of wavefront distortions induced by acoustic heterogeneities in breast thermoacoustic tomography (TAT) are studied. Amplitude distortions are shown to be insignificant for different scales of acoustic heterogeneities. For wavelength-scale, or smaller, heterogeneities, amplitude distortion of the wavefront is minor as a result of diffraction when the detectors are placed in the far field of the heterogeneities. For larger-scale heterogeneities at the parenchyma wall, by using a ray approach (geometric optics), we show that no refraction-induced multipath interference occurs and, consequently, that no severe amplitude distortion, such as is found in ultrasound tomography, exists. Next, we consider the effects of phase distortions (errors in time-of-flight) in our numerical studies. The numerical results on the spreads of point sources and boundaries caused by the phase distortions are in good agreement with the proposed formula. After that, we demonstrate that the blurring of images can be compensated for by using the distribution of acoustic velocity in the tissues in the reconstructions. The effects of the errors in the acoustical velocities on this compensation also are investigated. An approach to implement the compensation using only TAT data is proposed. Lastly, the differences in the effects of acoustic heterogeneity and the generation of speckles in breast TAT and breast ultrasound imaging are discussed.

I. INTRODUCTION

WHEN an electromagnetic pulse is absorbed by biological tissue, the heating and subsequent expansion causes the emission of acoustic signals; this phenomenon is called the thermoacoustic effect. In thermoacoustic tomography (TAT), the thermoacoustic signals from a tissue sample are collected to map the distribution of the radiation absorption within the sample. Radiation absorption is closely related to the physiological and pathological status of the tissue. For example, the microwave absorption rate of cancerous breast tissue is two to five times greater than that of the surrounding normal breast tissue. This difference has been attributed to an increase in the amount of bound water and sodium within malignant cells [1]-[3].

The TAT combines good imaging resolution with high imaging contrast. Microwave imaging alone has the ad-

vantage of good imaging contrast but suffers from poor spatial resolution [4]-[7]. On the other hand, purely ultrasonic imaging has good spatial resolution but poor contrast. TAT capitalizes on the advantages of both methods.

There are a variety of reconstruction algorithms for TAT [8]-[13]. By using the approximation that the distance between the detector and the absorbing object is much larger than the dimensions of the absorbing object, a three-dimensional (3-D) radon transform has been used to reconstruct objects in TAT [8]. A time-domain, focused-beam-forming technique also has been applied to image reconstruction in the photoacoustic scanning of tissue structures [9], and a delay-and-sum algorithm has been applied to microwave-induced TAT [12]. The above reconstructions were implemented in the time domain. In the frequency domain, exact reconstruction algorithms for TAT have been implemented in planar, cylindrical, and spherical configurations with series expansion techniques [11]-[13].

An important assumption in the above reconstruction algorithms is that the tissue is acoustically homogeneous. For many medical imaging applications, including imaging of the female breast, this assumption is an approximation. For example, the speed of sound in the breast can vary from 1400 m/s to 1550 m/s. Errors due to the assumption of a constant acoustic speed, which has never been studied in TAT, potentially can have a pronounced effect on image quality. In breast ultrasound tomography (UT), however, wavefront distortion has been studied extensively [14]-[17]. The amplitude distortion caused by refraction dominates the phase distortion induced by acoustic speed variation in the breast UT [15]. Refraction occurs where there is a speed mismatch across a tissue interface. Because of refraction, rays from a single source can reach the same receiver by different paths, as shown in Fig. 1. The interference between these rays causes strong amplitude distortions in breast UT. Different deaberration methods have been proposed to compensate for phase distortion in UT [18], [19]. However, so far they have been inadequate to correct the strong amplitude distortion caused by refraction [20].

The effects of acoustic heterogeneity on breast TAT are estimated to be weaker than those in breast UT for the following reasons. First, signals in breast TAT are primarily in a lower frequency range (usually below 1.5 MHz [21]) than those in UT. Ultrasound scattering in this frequency range is weak. Second, in TAT, the acoustic source is induced by electromagnetic absorption; therefore, only one-way distortion on reception wave propagation occurs. As shown in Fig. 2, an acoustic ray, for example SB_1D, needs to pass through interface Σ only once. In contrast, in pure
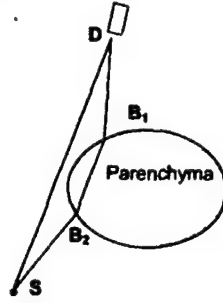
Fig. 1. Multipath interference caused by refraction at boundary points B_1 and B_2 in breast ultrasound imaging in transmission mode. S is a point source and D is a detector.
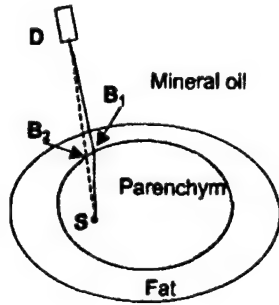

Fig. 2. Ray refraction at the parenchyma wall with breast TAT. The outer oval represents the breast surface, in which there is negligible refraction due to the good match of acoustic speed between fat and mineral oil. The solid line SB_1D represents a ray in the heterogeneous model; the dashed line SB_2D represents that in a homogeneous model. S is a point source and D is a detector; B_1, B_2 are two points at the parenchyma wall.

ultrasound imaging, either in the pulse-echo mode or in the transmission mode, ultrasound distortion includes two parts: distortion during both transmission and reception wave propagation. Therefore, the acoustic wave has to pass through the interface at least twice, as shown in SB_2B_1D in Fig. 1. Third, if the detection distance from the objects are properly chosen, the effects of amplitude distortion can be minimized in breast TAT, as will be shown in Section III.

In our work, we analyze the effects of amplitude distortion and numerically simulate the effects of phase distortion with the truncated conjugate gradient [22] (TCG) method. In Section II, we derive equations for the forward problem in an acoustically homogeneous model, which yields acoustic pressure from a known distribution of microwave absorption. In Section III, we investigate the effects of refraction on the wavefront amplitude and phase in breast TAT. We prove that, in breast TAT, a convex parenchyma wall (when observed from the outside of the parenchyma tissue) does not cause multipath interference and that the effects of amplitude distortion also are not severe for a concave boundary. An equation for the for-

ward problem in an acoustically heterogeneous model also is introduced at the end of Section III. The inversion algorithm of TCG, and the model and parameters used in the numerical simulations, are presented in Section IV. In Section V, the effects of phase distortion are studied numerically. We show how the degradation of the reconstructed images depends on acoustic heterogeneity when acoustic heterogeneity is not considered in the reconstruction algorithm. Correction of phase distortion should be the first step for improving image quality in breast TAT because phase is much more important in imaging than amplitude when there is no severe amplitude distortion [23], [24]. Therefore, the reconstructions are implemented with consideration of acoustic velocity heterogeneity to illustrate how the imaging degradation can be compensated for. The effects of the errors in the acoustical velocities on this compensation also are investigated. In Section VI, an approach to implement compensation with only TAT data is proposed. The differences between breast TAT and breast ultrasound imaging on the effects of acoustic heterogeneity and speckles are explained by their differences in central ultrasound frequency and detection geometry. Section VII presents conclusions.

II. THE FORWARD PROBLEM IN A HOMOGENEOUS MODEL

We begin by deriving a formula for the forward problem for an acoustically homogeneous model, then modify it at the end of Section III to consider velocity heterogeneity. In the case of thermal confinement, the acoustic wave at point $\mathbf{r}$ and time t, $p(\mathbf{r}, t)$, is related to the microwave absorption $H(\mathbf{r}, t)$ by the following wave equation [25]:

$$\frac{\partial^2 p(\mathbf{r}, t)}{\partial t^2} - v_{s0}^2 \nabla^2 p(\mathbf{r}, t) = \frac{\beta}{C} \frac{\partial H(\mathbf{r}, t)}{\partial t}, \qquad (1)$$

where v_{s0} is the acoustic speed, C is the specific heat, and β is the coefficient of the volume thermal expansion. (1) can be rewritten in terms of $H(\mathbf{r}, t)$:

$$p(\mathbf{r}, t) = \frac{\beta}{4\pi C} \iiint \frac{\partial H(\mathbf{r}', t')}{\partial t'} \frac{d\mathbf{r}'}{|\mathbf{r} - \mathbf{r}'|}, \qquad (2)$$

where $t' = t - |\mathbf{r} - \mathbf{r}'|/v_s$. The source term $H(\mathbf{r}, t)$ can further be written as the product of a spatial component and a temporal component, i.e.:

$$H(\mathbf{r}, t) = I_0 \varphi(\mathbf{r}) \eta(t), \qquad (3)$$

where I_0 is a scaling factor proportional to the incident radiation intensity, $\varphi(\mathbf{r}')$ describes the to-be-reconstructed microwave absorption properties of the medium at $\mathbf{r}'$, and $\eta(t)$ describes the shape of the irradiating pulse. Substituting (3) into (4) results in:

$$p(\mathbf{r}, t) = \frac{\beta I_0}{4\pi C} \iiint \varphi(\mathbf{r}') \frac{d\eta(t')}{dt'} \frac{d\mathbf{r}'}{|\mathbf{r} - \mathbf{r}'|}. \qquad (4)$$

We proceed by transforming the time-dependent wave equation into the temporal-frequency domain. Denoting the Fourier transforms of p and η by $\bar{p}$ and $\bar{\eta}$, respectively, we have:

$$p(\mathbf{r}, t) = \int_{-\infty}^{\infty} \bar{p}(\mathbf{r}, k) \exp(ikt) dk,$$
$$\eta(t) = \int_{-\infty}^{\infty} \bar{\eta}(k) \exp(ikt) dk. \tag{5}$$

Substituting (5) into (4) results in:

$$\bar{p}(\mathbf{r}, k) = \frac{i\beta I_0 k \bar{\eta}(k)}{4\pi C} \iiint \varphi(\mathbf{r}') \frac{\exp(-ik|\mathbf{r} - \mathbf{r}'|/v_{s0})}{|\mathbf{r} - \mathbf{r}'|} d\mathbf{r}'. \tag{6}$$

Define $\bar{p}_1(\mathbf{r}, k) = \bar{p}(\mathbf{r}, k)/(2\pi\eta(k))$, substitute it into (6), apply an inverse Fourier transform to both sides of the equation, and obtain the following equation:

$$p_1(\mathbf{r}, t) = \frac{v_{s0}\beta I_0}{4\pi C} \frac{\partial}{\partial t} \iint_{t=t_f(\mathbf{r}',\mathbf{r})} \frac{\varphi(\mathbf{r}')}{|\mathbf{r} - \mathbf{r}'|} d\mathbf{r}', \tag{7}$$

where

$$t_f(\mathbf{r}', \mathbf{r}) = |\mathbf{r} - \mathbf{r}'|/v_{s0}, \tag{8}$$

is the time-of-flight (TOF) from to $\mathbf{r}'$ to $\mathbf{r}$; $p_1(\mathbf{r}, t)$ is the deconvolution of $p(\mathbf{r}, t)$ with respect to the length of the microwave pulse and can be interpreted as the detected pressure signal when the microwave pulse is infinitely narrow. The physical meaning of this equation is that, in an acoustically homogenous medium, the pressure p_1, at a spatial point $\mathbf{r}$ and time t, is proportional to the first-order temporal derivative of the integration of the absorbed microwave energy over a spherical surface [a circle in the two-dimensional (2-D) case]. The spherical surface is centered at $\mathbf{r}$ and has a radius of $t v_{s0}$.

III. THE EFFECT OF ACOUSTIC HETEROGENEITY IN TAT

A TAT model is shown in Fig. 2. In our imaging system, mineral oil is chosen as the coupling medium for both microwaves and ultrasonic waves. The acoustic speed in mineral oil is 1437 m/s [26], which is very close to that in fat [27]. Therefore, there should be negligible refraction at the boundary between the breast and the mineral oil; consequently, we will consider only the effects of the acoustical heterogeneity within the breast. More details on our TAT experimental setup can be found in [12].

A. Amplitude Distortion Caused by Refraction

Fig. 1 shows the multipath interference in breast ultrasound imaging in transmission mode. The acoustic ray from source S can travel to detector D by two different paths, SD and SB_2B_1D, due to refraction at the interfaces between different tissues. The interference between
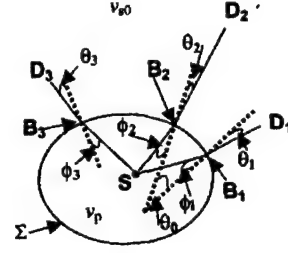

Fig. 3. Diagram showing that no two rays from a point source S will intersect with each other after being refracted at a convex boundary Σ and entering a medium with a slower acoustic speed. S is a point source; D_1 and D_2 are detectors; ϕ_1, ϕ_2, and ϕ_3 are the incidence angles; θ_1, θ_2, and θ_3 are the transmission angles; the solid lines represent acoustic rays; B_1, B_2, B_3 are three points at the parenchyma wall; v_p, v_{s0} are the mean acoustic speeds in the parenchyma tissue and the fat tissue, respectively; and $v_p > v_{s0}$.

the two rays can cause amplitude distortion [15]. In the following subsections, we will first prove that there is no multipath interference in the case of a convex parenchyma wall in breast TAT. Then, we will show that the amplitude distortion also is not severe for a concave parenchyma wall.

1. Convex Boundary: In this subsection, we will show that there is no multipath interference in the TAT of the breast with a convex parenchyma wall by proving that no two rays from a source within the parenchyma will intersect with each other after refractions at the wall. The model is shown in Fig. 3, where S is an acoustic source; v_p and v_{s0} are the acoustic speed in the breast parenchyma and the medium (also the fat), respectively ($v_p > v_{s0}$); the dashed lines are the normals of the boundary at points B_1, B_2, B_3, respectively; ϕ_1, ϕ_2, and ϕ_3 are the angles of incidence; θ_1, θ_2, and θ_3 and are the angles of transmission; and the solid lines represent the acoustic rays. Because the boundary is convex, it can be inferred that rotation from the normal at point B_2 to the normal at point B_1 is clockwise and the angle is θ_0 (positive). We also have $\phi_2 < \theta_0 + \phi_1$, which can be seen by extending lines SB_2 and SB_1 to the outside of the boundary and noticing that SB_2 and SB_1 will never intersect outside the boundary. To prove B_2D_2 and B_1D_1 will not intersect outside the boundary, we need to show $\theta_2 < \theta_0 + \theta_1$. According to Snell's law, we have:

$$\sin\theta_2 = (1 - \alpha)\sin\phi_2,$$
$$\sin\theta_1 = (1 - \alpha)\sin\phi_1, \tag{9}$$

where $\alpha = 1 - v_{s0}/v_p$, which is positive when $v_p > v_{s0}$. The problem can be discussed under two conditions:

$\phi_2 < \phi_1$. In this case, according to (9), we have $\theta_2 < \theta_1$ and therefore $\theta_2 < \theta_0 + \theta_1$. And

$\phi_2 \geq \phi_1$. (9) can be transformed to:

$$\sin\left(\frac{\theta_1 - \phi_1}{2}\right) = -\frac{\alpha\sin(\phi_1)}{2\cos((\theta_1 + \phi_1)/2)},$$
$$\sin\left(\frac{\theta_2 - \phi_2}{2}\right) = -\frac{\alpha\sin(\phi_2)}{2\cos((\theta_2 + \phi_2)/2)}. \tag{10}$$

Because $\phi_2 \geq \phi_1$ and consequently $\theta_2 \geq \theta_1$, it is straightforward to obtain $\theta_2 - \phi_2 \leq \theta_1 - \phi_1$ from (10). Using $\phi_2 < \theta_0 + \phi_1$, we have $\theta_2 < \theta_0 + \theta_1$. In conclusion, we prove that, after the rays from a point source go into another medium with a slower acoustic speed, the rays cannot intersect with each other when the interface is convex. In another words, for any pairing of point source and detector, there is only one acoustic path that satisfies Snell's law. Consequently, no multipath interference occurs and amplitude distortion can be ignored. This conclusion also can be applied to a boundary with wavelength-scale concave segments. This kind of boundary can be treated as a convex boundary approximately because the effects of the small concave segments can be neglected when the detectors are placed in the far field of the segments, as will be shown in the following subsection. In contrast, multipath interference does occur after rays pass a convex parenchyma wall in ultrasound imaging, as shown in Fig. 1. This difference makes the amplitude distortion in TAT of the breast with a convex, or approximately convex parenchyma wall, smaller than that in pure ultrasound imaging.

2. Concave Boundary: We realize that, in reality, the boundary between mammary tissue and subcutaneous fat tissue might be concave and quite irregular. In this subsection, we will show that the amplitude distortion caused by a concave boundary is not severe. Basically, this conclusion can be explained as follows. With wavelength-scale or smaller heterogeneities, amplitude distortion of the wavefronts is minor due to diffraction when the detectors are placed in the far field of the irregular boundary segment. When the size of the concave segment is larger, according to the imaging formula of concave boundaries shown below, only imaginary images exist after the wavefronts from real objects pass through the concave boundary. Equivalently, no two rays from a point source will intersect with each other after passing through the concave boundary segment and no strong amplitude distortion occurs. In the following subsection, we will define two kinds of multipath interference: focusing-type and nonfocusing-type interferences. The former can induce amplitude distortion in both narrowband and broadband signals; the latter can induce only amplitude distortion in narrowband signals. As a consequence, we need only examine in detail the focusing-type interference, because signals in breast TAT are broadband.

Definition of focusing-type and nonfocusing-type interferences. Fig. 4 shows the two different kinds of multipath interferences. Three different ray paths SB_1D, SB_2D, SB_3D from source S to detector D are shown, and each of them is assumed to satisfy the refraction law. The SB_1D and SB_2D can be considered as a small modification of the straight line SD due to weak heterogeneity, and SB_3D is far away from SD. We use focusing-type interference to refer to the interference between pulses along the paths with the same TOFs. The interference between SB_1D and SB_2D is of this type. This is because SB_1D and SB_2D satisfy the refraction law, and their TOFs are local minima according to Fermat's principle [28]. Conse-
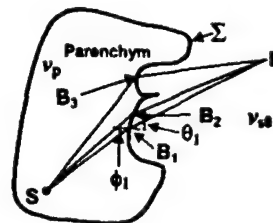

Fig. 4. Diagram to show two types of multipath interferences caused by a concave boundary: focusing-type interference between SB_1D and SB_2D and nonfocusing-type interference between SB_1D (SB_2D) and SB_3D. In a focusing-type interference, the different rays have approximately the same TOF, which consequently yields constructive interference and strong amplitude distortion. In this case, the boundary segment around B_1B_2 can be considered as a lens. In nonfocusing-type interference, the difference of the TOFs along two rays is larger than the pulse width; consequently, the pulses are separated temporally and no strong amplitude distortion occurs. See Fig. 3 for the symbols' definitions.

quently the rays around SB_1D and SB_2D should have almost the same TOF. After noticing that B_1 and B_2 are close to each other, it can be inferred that SB_1D and SB_2D have the same TOFs. Actually, the boundary segment around B_1B_2 can be considered a focusing lens and can produce strong amplitude distortion even for broadband pulses, as verified by the strong amplitude distortion in broadband breast ultrasound imaging [15]. As a contrast, we use nonfocusing-type interference to refer to the interference between the pulses along paths with different TOFs. The interference between SB_3D and SB_1D (SB_2D) is a nonfocusing-type interference, because B_3 is far from B_1 and B_2, and generally it can be assumed that $|t_{SB_1D} - t_{SB_3D}|$ and $|t_{SB_2D} - t_{SB_3D}|$ (t_{SB_1D}, t_{SB_2D}, and t_{SB_3D} are the TOFs along ray paths SB_1D, SB_2D, and SB_3D, respectively) are larger than 1 μs, the average pulse width of thermoacoustic signals in our RF TAT experiments. Consequently, the pulse along SB_3D is separated temporally from the pulses along SB_1D, SB_2D, and the interference between SB_3D and SB_1D (SB_2D) is insignificant. Similar analyses can be found in the pure ultrasound imaging literature [15].

The signals along SB_3D may introduce artifacts in the reconstructed images because detector D receives two pulses from source S—one along SB_1D and SB_2D, and the other along SB_3D. To estimate the effects of signals along path SB_3D, we numerically simulate refractions at arbitrary boundaries, at which the locations of source S and detector D are randomly chosen. We find that the SB_3D-type refraction rarely occurs. Therefore, we expect the artifacts introduced by the signals along SB_3D to be insignificant; and, in the following studies, we consider only focusing-type interference.

Analysis of focusing-type interference. For a boundary segment with a size of $2a$ much larger than the wavelength of interest λ, we will use a ray model to study the effects of refraction. To have focusing-type interference, the posi-

tions of the source and detector must satisfy the following equation:

$$\frac{1}{l_{SB_1}/\cos\phi_1} + \frac{1}{l_{B_1D}(1-\alpha)/\cos\phi_1} = \frac{\alpha}{R_1} = \frac{1}{f}, \quad (11)$$

where f is the focal length of segment B_1B_2 in Fig. 4 and $f = R_l/\alpha$; R_l is the radius of the segment; and l_{SB_1} and l_{B_1D} are the lengths of line SB_1 and DB_1, respectively. The derivation of (11) can be found in Appendix A. To have a real image, or equivalently to have two rays intersect after passing through boundary segment B_1B_2, (11) requires:

$$l_{SB_1}/\cos(\phi_1) > R_l/\alpha. \quad (12)$$

Next, we derive another requirement due to diffraction for the occurrence of strong amplitude distortion. The smallest beam width after a wavefront passes through a boundary segment with a size of $2a$ is $l_{B_1D}\lambda/a$, where λ is the wavelength of the acoustic wavefront. To induce strong focusing, for example, to have a beam width smaller than a at D, we need to have:

$$l_{B_1D} < a^2/\lambda. \quad (13)$$

The right-hand side of the above inequality is the same as the definition of the near-field length of a plain transducer when a is considered as the radius of the transducer. It is well-known that the amplitude can change rapidly in the near field due to the acoustic interference, but it is much smoother in the far field. Similarly, if the detector is placed within the far field of the concave boundary segment, the amplitude distortion will be less severe in TAT.

Eq. (13) is derived for the case in which a wavefront propagates perpendicularly to the boundary segment. When a wavefront is incident obliquely upon the segment B_1B_2, the effective size of the lens in (13) should be the projection of its geometrical size onto the plane perpendicular to the propagation direction of the incident wave. Then we have:

$$l_{B_1D} < (a\cos\phi_1)^2/\lambda. \quad (14)$$

By combining (14), (12), and $R_l > a$, we obtain the following requirement for inducing strong amplitude distortion after passing through the boundary:

$$l_{SB_1} > \frac{\sqrt{l_{B_1D}\lambda}}{\alpha}. \quad (15)$$

It can be seen from this equation that when l_{B_1D} is large enough:

$$l_{B_1D} > \frac{(l_{SB_1}\alpha)^2}{\lambda}, \quad (16)$$

the strong amplitude distortion can be minimized. Notice that the required minimum detection distance in (16) increases linearly with the frequency of the wave.

In the derivation of (11), ray theory is utilized. Ray theory is valid under the following conditions [29]:

$$l_{B_1D} \ll 4a^2/\lambda, \quad (17)$$

and

$$2a \gg \lambda. \quad (18)$$

Eq. (17) is similar to (13), but the former is stronger; (17) states that the ray model is valid when the wave propagation distance from the heterogeneity is much smaller than $4a^2/\lambda$; beyond that distance, diffraction must be considered. In our analysis of amplitude distortion in TAT, we extend the effective range of the ray model from (17) to (13). This is based on the assumption that the ray model overestimates the wavefront distortions due to ignorance of the diffraction effect. Therefore, if the analysis using ray theory shows that there is only minor amplitude distortion when (16) and (18) are met, the analysis from the exact wave equation should yield the same result.

For a wavelength-scale boundary segment (e.g., $2a < 4\lambda$), (18) is violated, and (16) cannot be applied. In this case, strong amplitude distortion can be minimized by placing the detector within the far field of the heterogeneity:

$$l_{B_1D} > 4\lambda, \quad (19)$$

where we have substituted $2a < 4\lambda$ into (13). Combining (16) and (19), we obtain the minimum detection distance for avoiding strong amplitude distortion induced by different scales of heterogeneities:

$$l_{B_1D} > \max\left[\frac{(l_{SB_1}\alpha)^2}{\lambda}, 4\lambda\right], \quad (20)$$

where max[] represents computing the maximum. Using the following parameters, $l_{SB_1} < 10$ cm (the assumed size of the breast parenchyma), and $\alpha = 0.07$, in which the mean velocity in the subcutaneous zone v_f and the breast parenchyma v_p are assumed to be 1437 m/s [28] and 1546 m/s [30], respectively, we have $l_{B_1D} > 4.9$ cm for 1.5 MHz ultrasound and $l_{B_1D} > 1.63$ cm for 0.5 MHz ultrasound. These requirements can be met easily in TAT experiments. For ultrasound waves with a frequency less than 0.5 MHz, it is not necessary to apply (20), because ultrasound scattering by soft tissue in this frequency range can be neglected and no severe amplitude distortion is expected.

The above analysis is made for 2-D TAT. This corresponds to the experimental configuration in which a linear, or ring array of transducers with a cylindrical surface is used, and a section image of the breast in the detection plane is desired. However, because of the refraction at the parenchyma wall, the thermoacoustic waves from the objects within the detection plane might deviate out of the plane. On the other hand, the signals collected in the detection plane are transmitted by the objects out of the

detection plane rather than within it. Consequently, the obtained image is actually a projection of the out-of-plane objects onto the detection plane. To reduce this kind of error, we can use the technique of compressing the breast against the chest wall, which has proven to be effective in reducing wavefront distortions in breast ultrasound imaging. After the compression, the acoustic signals can pass through the interface more or less perpendicularly. However, the ultimate solution to this problem is 3-D TAT. Most of the 2-D results on amplitude distortions (e.g., (14), (16), (20), and the results on phase distortions shown later) can be directly applied to 3-D TAT; (11) also can be applied to analyze a 3-D convex boundary locally by substituting $-R_l$ for R_l. Then, it is straightforward to see that in a 3-D case no two rays can intersect with each other after passing a convex boundary segment.

In summary, our analysis shows that, in RF breast TAT, if the detection is made at a distance to the breast surface required by (20), the amplitude distortion caused by the refraction at the parenchyma wall is not important because of the diffraction effect and the fact that TAT signals are broadband, have low central frequency, and experience only one-way transmission through the parenchyma wall. The effect of intramammary fat lobules will be addressed in Section VI. Therefore, in the following analysis and simulations, we will consider only phase distortion.

B. Phase Distortion Caused by Refraction and Speed Variation

If the background is acoustically homogeneous, an acoustic ray from source S in Fig. 2 goes along the straight line SD to reach detector D. When there is acoustic heterogeneity, an acoustic ray goes along line SB_1D because of refraction at the interface. Assume there is no change in the shape of the acoustic pulse caused by acoustic heterogeneity. The TOF from source S to detector D in the acoustically heterogeneous model is:

$$t_{SB_1D} = \int_{SB_1D} dl/v_s(\mathbf{r}''), \tag{21}$$

where $v_s(\mathbf{r}'')$ is the local acoustic speed, and $\mathbf{r}''$ is a point within line SB_1D. Now, we will show that t_{SB_1D} can be approximated to the second order of a small value $\varepsilon = (v_s(\mathbf{r}'') - v_{s0})/v_{s0}$ by $t_{SD} = \int_{SD} dl/v_s(\mathbf{r}'')$, where v_{s0} is the velocity used in the acoustically homogeneous model. According to Fermat's principle, an acoustic ray travels on the fastest path. In other words, SB_1D is a local minimum of TOF. Now assume B_1 is displaced to B' by a small distance $q = |BB'|$,

$$\frac{q}{l_{SD}} = o(\varepsilon). \tag{22}$$

After expanding $t_{SB'D}$ around t_{SB_1D} with respect to q, we have:

$$t_{SB'D} = t_{SB_1D} + q\left.\frac{\partial t_{SB'D}}{\partial q}\right|_{q=0} + o(\varepsilon^2). \tag{23}$$

Recalling that SB_1D is a local minimum, we have $\left.\frac{\partial t_{SB'D}}{\partial q}\right|_{q=0}$. Substituting it into (23) and assuming $l_{B_2B_1}/l_{SD} = o(\varepsilon)$ due to the weak acoustic heterogeneity in breast tissue, we have:

$$t_{SD} = \int_{SD} dl/v_s(\mathbf{r}'') = t_{SB_1D} + o(\varepsilon^2). \tag{24}$$

The above result can be understood in the following way. Although the path length of SB_1D in Fig. 2 is longer than that of SD and $(l_{SB_1} + l_{DB_1} - l_{SD})/l_{SD} = o(\varepsilon)$, path SD has a longer part within the slow-speed area than path SB_1D. The combination of the two opposite effects leads to the cancellation of the first-order term of ε in (24).

Next we will show that the approximation of t_{SB_1D} by t_{SD} includes most of the flight-time variation induced by acoustic heterogeneity. The TOF from source S to detector D in an acoustically homogeneous and heterogeneous model is l_{SD}/v_{s0} and t_{SB_1D}, respectively. The difference between them is:

$$\begin{aligned} \delta t &= |t_{SB_1D} - l_{SD}/v_{s0}| \\ &= |t_{SB_1D} - t_{SD} + t_{SD} - l_{SD}/v_{s0}| \\ &\approx |o(\varepsilon^2) + t_{SD} - l_{SD}/v_{s0}| \approx o(\varepsilon), \end{aligned} \tag{25}$$

where we used (24). Combining δt with (24), we have:

$$\frac{|t_{SD} - t_{SB_1D}|}{\delta t} = o(\varepsilon). \tag{26}$$

Therefore, the error in the approximation of t_{SB_1D} by t_{SD} is not important. At last, it should be pointed out that our analysis of TOF can be applied to both 2-D and 3-D TAT.

C. Forward Formula in an Acoustically Heterogeneous Model

In our analysis of TOF, we consider only a single interface. The results can be extended to the case involving several interfaces. In general, the TOF from $\mathbf{r}$ to $\mathbf{r}'$ can be expressed as:

$$t_f(\mathbf{r}', \mathbf{r}) = \int_{L(\mathbf{r}',\mathbf{r})} dl/v_s(\mathbf{r}'') + o(\varepsilon^2), \tag{27}$$

where $L(\mathbf{r}', \mathbf{r})$ is the straight line from $\mathbf{r}'$ to $\mathbf{r}$, and $\mathbf{r}''$ lies within the line L. Combining (27) and (7), we obtain the forward formula for acoustically heterogeneous TAT.

Our analysis of TOF is in agreement with the results from a more rigid model [31]. It was reported that the variation in travel time caused directly by acoustic speed heterogeneity is a first-order perturbation, and that the effect of the ray bending on the travel times is a second-order one. For breast tissue, which is weakly acoustically heterogeneous, it is enough to consider the first-order perturbation by computing the integral of the slowness perturbation along straight lines, as shown in (27).

IV. IMPLEMENTATION AND MODELING OF NUMERICAL SIMULATIONS

A. Numerical Implementation

It can be seen from (7) that $p_1(\mathbf{r}, t)$ can be obtained from $\varphi(\mathbf{r}')$ after applying two linear operations to it: one is integration over the object space, the other is differentiation over t. Therefore, in its discrete form, (7) is a set of linear equations:

$$\mathbf{M}\varphi = \mathbf{p}. \qquad (28)$$

where $\mathbf{M}$ is the matrix representing the product of the two linear operators. The standard techniques of solving a linear equation system can be used. We adopted the TCG method to minimize the object function $\|\mathbf{M}\varphi - \mathbf{p}\|$ in the sense of least square root and no preconditioner is used. In the implementation of TCG, instead of the whole matrix $\mathbf{M}$, a function that gives the multiplication of matrix $\mathbf{M}$ and its adjoin with an arbitrary vector is required. Consequently, the demand on computer memory is reduced greatly, compared with many other techniques that require storing the whole matrix $\mathbf{M}$ in memory. Another advantage of TCG is that an approximate result can be obtained by stopping the iteration before reaching the full convergence. The truncation not only saves computation time but also provides a way of regularization for stabilizing the results. In (28), we use the Savitzky-Golay smoothing method [32], rather than the finite differentiation method to implement the operation of the first-order temporal derivative, as the former yields a much smoother and more accurate result than the latter when data are noisy. We truncated our simulations after 15 iterations, which corresponds to the relative changes in the norms of the results, about 0.7% for the acoustically homogeneous model and up to 6% for the acoustically heterogeneous model. In both cases, further iterations yield little visible improvement to image and may induce instability.

In our simulations, we choose the 2-D case rather than the 3-D case because the computational complexity can be reduced and because it is much easier to interpret and graph a 2-D image. For the 2-D case, the integration in (7) is over a curve instead of a spherical surface:

$$p_1(\mathbf{r}, t) = \frac{\beta I_0 v_{s0}}{4\pi C} \frac{\partial}{\partial t} \oint_{t=t_f(\mathbf{r}', \mathbf{r})} \frac{\varphi(\mathbf{r}')}{|\mathbf{r} - \mathbf{r}'|} d\mathbf{r}', \qquad (29)$$

where t_f is determined by (27). Nevertheless, the conclusions of a 2-D case can be extended to a 3-D one.

B. Model and Parameters in Numerical Simulations

Fig. 5(a) and (b) illustrate the acoustic and RF absorption models of the breast, respectively. The acoustic model of the breast in our simulations is based on experimental results on the distribution of acoustic speed in the breast [27]–[30]. Acoustic speed in the breast may vary
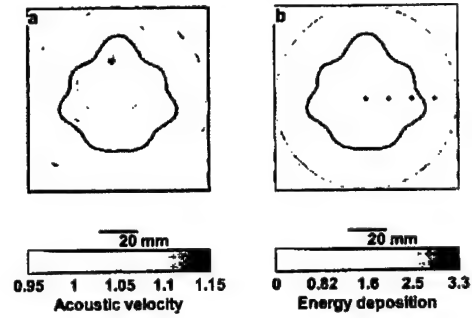

Fig. 5. (a) Distribution of acoustic velocity normalized to v_{s0} for a breast model. The breast surface is represented by the outer circle; the wall between the breast parenchyma and the subcutaneous fat is represented by the inner irregular boundary. (b) The microwave absorption distribution in our model. The four small spots represent the assumed tumors.

from 1400 m/s to 1550 m/s. Generally, a zone of low velocity (1400–1450 m/s) characterizes subcutaneous fat [33]. The speed in normal dense parenchyma is higher, varying from 1500 m/s to 1550 m/s [30]. In Fig. 5 the outer circles, with a radius of 50 mm, represent the breast surface. The inner irregular boundaries, which are generated by randomly modifying a circle, represent the walls of the breast parenchyma. The size of the parenchyma tissue was changed in different simulations because the ratio of breast parenchyma to subcutaneous fat may change with age. Usually, a young female breast has less fat than an older one does. The mean velocity in the subcutaneous zone v_f and the breast parenchyma v_p are set to be 1437 m/s [27] and 1546 m/s [30], respectively. A random component, which is a normal distribution with a mean of zero and a variance of 33 m/s, is added to the velocity distribution to simulate the velocity fluctuations in the subcutaneous zone [33] and the breast parenchyma [30]. Later, our simulation results show that the random component of velocity will induce little spread in the images due to the cancellation after integration. To ensure that the acoustic speed does not change sharply within each tissue, the random component is smoothed spatially by introducing a correlation length as shown below. The imaged area is divided into patches with side dimensions of a correlation length. The value of the random component at the center of each patch is determined according to the normal distribution mentioned above; then the random component within the patch decreases linearly to zero at the boundary of the patch. We tried different correlation lengths in our simulations, from 12 mm (about the size of fat lobules in parenchyma tissue) to 3 mm. The image degrades more with increasing correlation length, but the difference is minor. The correlation length was chosen to be about 6 mm for the reported results. The speed distribution in Fig. 5 was normalized to 1437 m/s, which is assumed to be the acoustic velocity in the medium surrounding the breast and the mean acoustic speed in the subcutaneous fat.

The RF absorption model of the breast is shown in Fig. 5(b). The boundary shapes are the same as in Fig. 5(a). The RF absorption coefficients in fat, tumors, and the coupling oil are set to be 0.3, 3, and 0 after being normalized to that in the parenchyma. The tumors, shown in Fig. 5(b) as dark spots, are placed evenly along the horizontal direction to study the dependence of the distortions in the images on the tumor locations. We set the radii of the four tumors to about 1.2 mm to simulate approximately the point-source spread caused by acoustic heterogeneity.

The parenchyma wall in our simulation is generated as the following equation: $r(\theta) = r_p(1 + Ag(\theta))$, where $r(\theta)$ is the radius of the boundary at angle θ, r_p is the mean radius of the boundary and is used to represent the size of the parenchyma tissue, A is the distortion amplitude, and $g(\theta)$ generates random numbers within $[-1, 1]$.

The parameters in our simulations are chosen as follows unless stated otherwise. Noise is added to the generated signals so that the frequency range with signal-to-noise ratio (SNR) larger than unity is from 0 to 1.5 MHz, which approximates our experimental results [21]. The radius of the circle of detection is set to be 125 mm to meet (16); the angle range of detection is 2π with 400 steps. An insufficient number of scanning steps can cause radial aliases in the reconstructed image [13]. Thermoacoustic signals are sampled for 108 μs at a sampling rate of about 14 MHz, which is sufficient to meet the Nyquist criteria. The 100 mm by 100 mm imaging field is mapped with a 256 by 256 mesh. In our simulations, the thermoacoustic signals are generated in an acoustically inhomogeneous model, and the reconstruction is implemented for two cases—with and without the consideration of acoustic heterogeneity.

V. NUMERICAL RESULTS

We first study the effect of acoustic heterogeneity on imaging when acoustic heterogeneity is considered in the forward problem but not in the reconstruction. In the reconstruction, $v_s(\mathbf{r})$ in (27) is set to be v_{s0}. Then we show how to improve image resolution after considering acoustic heterogeneity in the reconstructions. And, the effects of measurement errors in v_f, v_p and Σ on the improvement are investigated.

A. Reconstruction Without Considering Heterogeneity

Fig. 6(a)–(d) shows the results when acoustic heterogeneity is not considered in the reconstructions. In the four simulations, the mean radii of the parenchyma wall r_p are set to be 0.8, 0.6, 0.4, and 0.2 of the breast radius. The wall is distorted randomly in the simulations, and the distortion amplitude is 0.1. We measure the point-spread width (PSW), which is the width of the image of a point source along a specific direction minus its real size, 2.4 mm, and the boundary spread width (BSW), which is the width of the blurred parenchyma wall Σ in an image. It is clear from
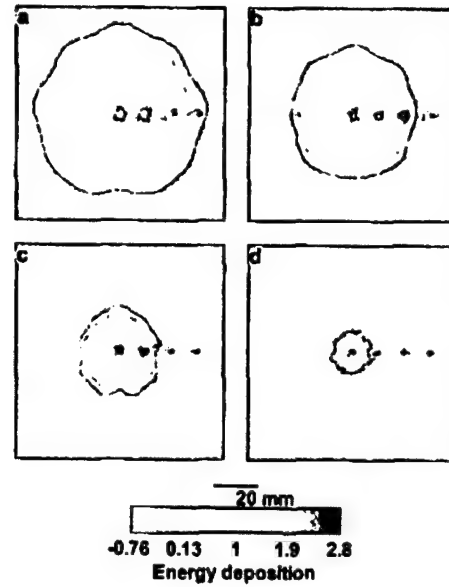

Fig. 6. Images when acoustic heterogeneity is not considered in the reconstructions. The mean radii of the parenchyma wall are set to be (a) 0.8, (b) 0.6, (c) 0.4, and (d) 0.2 of the breast radius, respectively. The point-spread width and the boundary-spread width increase linearly with the size of the parenchyma tissue. Note that the spread of points outside the parenchyma tissue are much smaller than the spread inside.
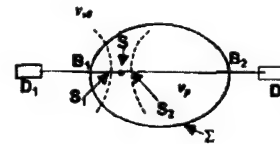

Fig. 7. Diagram for deriving (30), which estimates the spread of a point source S along line $D_1 D_2$ due to TOF error. S_1 is the intersection of $D_1 D_2$ with the backprojection arch of the signal transmitted by source S and detected by detector D_1; S_2 is the corresponding one at D_2.

Fig. 6 that PSW and BSW increase with the radius of the parenchyma wall. It is proved in Appendix B that the two widths can be estimated by the following equation:

$$w = l_p \alpha, \qquad (30)$$

where l_p is $2r_p$ in the case of BSW; in the case of PSW, l_p is the length of a ray within the parenchyma tissue along a specific direction (for example the length of $B_1 B_2$ in Fig. 7). The PSW is anisotropic because l_p depends on direction. This anisotropy of PSW can be verified by the observation that the three tumors within the parenchyma tissue in Fig. 6(a) and (b) have the same spread along the horizontal direction, and their spreads along the vertical direction decrease when the tumors are located away from the center.
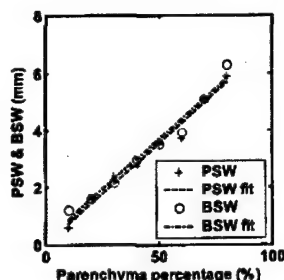
Fig. 8. Quantitative results of the point-spread width and boundary-spread width along the horizontal direction in eight simulations in which the mean radius of the parenchyma wall changes from 0.1 to 0.8 of the breast radius using a step of 0.1. The corresponding linear fittings of PSW (dashed) and BSW (dash-dotted) are in good agreement with the proposed formula (30).
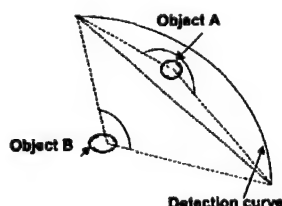

Fig. 9. Diagram showing that in TAT a π or wider view can provide complete data for reconstruction. A view means the angle subtended by the detection curve when observed from the to-be-imaged object. Object A has a view larger than π, and object B has a view less than π.

Fig. 10. (a) Compensation for the degradation in images when complete acoustic heterogeneity information is included in the reconstructions. (b) Only exact v_p, v_f, and Σ are included to show the insensitivity of improvement to a random component of the acoustic-velocity distribution. (c) and (d) Images in which there are (c) 1% and (d) 3% errors in v_p, respectively. (e) Images in which Σ is scaled down by 10%. (f) Images in which 20% random error is introduced in Σ. These results show the stability of the improvement to the errors in v_p, v_f, and Σ.

Fig. 8 shows the quantitative results (with an error of ± 0.8 mm) of the PSW and BSW along the horizontal direction in eight simulations in which the radius changes from 0.1 to 0.8 of the breast radius with a step of 0.1. The corresponding linear fitting results for the PSW and BSW are shown as dashed and dash-dotted lines, respectively. The slopes of the two lines are 0.071 and 0.0705, respectively, both of which are close to the estimated rate of 0.07 derived from (30) after substituting the parameters used in our simulations, the radius of the breast $r_b = 50$ mm and $\alpha = 0.07$.

Another interesting point in Fig. 6 is that the PSW of the objects outside the parenchyma tissue are affected little by acoustic heterogeneity. Only minor artifacts are observed near them. This is because in TAT a π or wider view can provide complete data for reconstruction [34]. Here, a view means the angle subtended by the detection curve when observed from the to-be-imaged object. For example, object A in Fig. 9 has a view larger than π, and object B's is less than π. If an object is outside the parenchyma tissue, it has at least a π-view detection range in which the medium between the object and the detectors is acoustically homogeneous. Therefore, a perfect image can be reconstructed from this part of the data. On the other hand, the image reconstructed from the part of signals that experience the heterogeneous medium is weak
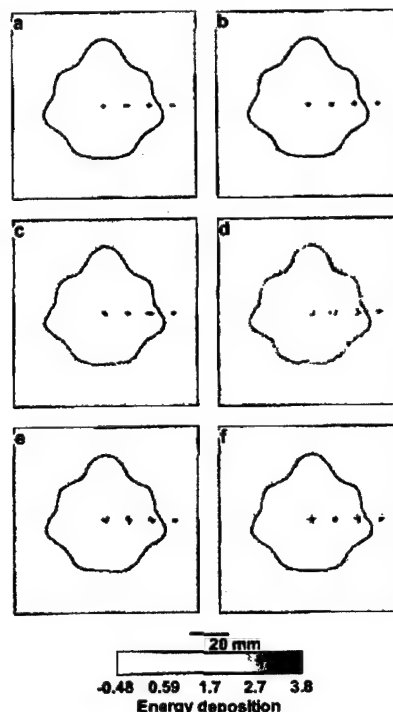
in amplitude because the flight-time errors compromise the build-up strength of the signals.

In addition to blurring of images, acoustic heterogeneity increases the background noise level and decreases the values of reconstructed tumors, which consequently reduces the contrast of tumors in the images and the detectability of small tumors. A comprehensive quantitative study of this issue will depend on the SNR of the hardware of the imaging system, the parameters of the imaging system and reconstruction algorithms, and the contrast of the to-be-imaged objects. Meaningful conclusions should be made based on relevant experimental data which we leave for future study.

B. Reconstruction with the Consideration of Heterogeneity

The exact distribution of acoustic velocity is included in the model in Fig. 10(a). Although the result is good, it is not practical, because it is not feasible to obtain the exact distribution of velocity in the breast by current technology. A much more practical situation is when the mean velocities v_f, v_p, and boundary profile Σ are approximately known and the velocity fluctuation within each area is un-
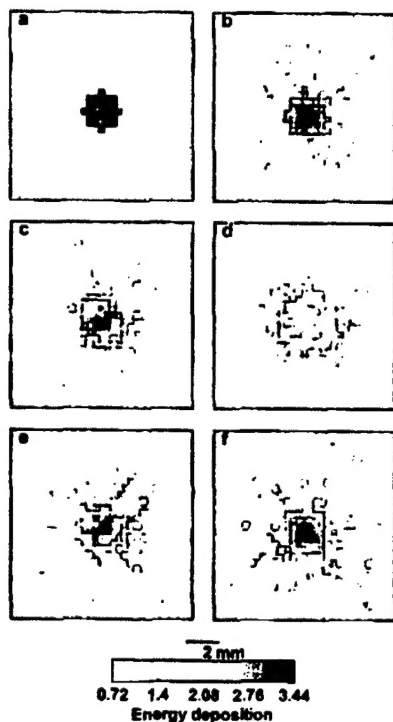
Fig. 11. (a)–(f) Close-up images around the central tumor in Fig. 10. Compensation for the degradation in images when complete acoustic heterogeneity information is included in the reconstructions. (b) Only exact v_p, v_f, and Σ are included to show the insensitivity of improvement to a random component of the acoustic-velocity distribution. (c) and (d) Images in which there are (c) 1% and (d) 3% errors in v_p, respectively. (e) Image in which Σ is scaled down by 10%. (f) Image in which 20% random error is introduced in Σ.

known. Different approaches to obtain v_f, v_p, and boundary profile Σ will be explored in Section VI. Here, we will show the effectiveness of our compensation method. Figs. 10(b)–(f) show the images reconstructed from the same data as in Fig. 10(a), but the reconstruction algorithm used only v_f, v_p, and Σ to study the effects of the measurement errors in v_f, v_p, and Σ on the improvement. In Figs. 10(b)–(f), the random component of the acoustic-velocity distribution is ignored. In addition, v_p is decreased by 1% and 3% in Figs. 10(c) and (d), respectively; Σ is scaled down by 10% in Fig. 10(e); and a 20% random error is introduced to Σ in Fig. 10(f). Figs. 11(a)–(f) are the corresponding close-up images around the central tumor in Fig. 10. The r_p in these simulations is 0.6 of the breast radius, and the distortion amplitude of the parenchyma wall is 0.2.

1. Effect of Errors in Velocities: There is little difference between the resolution of the reconstructed images when we consider [Fig. 11(a)] and do not consider [Fig. 11(b)] the random component of velocity distribution, although the artifacts in the background in Fig. 11(b) are a little stronger than those in Fig. 11(a). The good resolution, after ignoring the random component of the

acoustic-velocity distribution in Fig. 11(b), can be explained by modifying (30) to:

$$w = \int_{B_1 B_2} \alpha(\mathbf{r}'') dl_p, \qquad (31)$$

where $\alpha(\mathbf{r}'') = 1 - v_{x0}/v_p(\mathbf{r}'')$ and is spatially dependent; the integration is over the line $B_1 B_2$ in Fig. 7. It can be found that the contributions of the random component of velocity are canceled in some degree after the integration over an acoustic ray.

Comparing Figs. 11(c) and (d) with Fig. 11(b), it can be noticed that a 1% error in v_p does not degrade the imaging quality much, but a 3% error in v_p greatly deteriorates the imaging resolution and contrast. This is because in our model the difference between v_f and v_p is about 7% of their speeds, and a 3% error in v_p actually accounts for 42% of the difference between v_f and v_p. Therefore, we conclude that an accuracy of 1% in the determination of v_p is sufficient for significant improvement in imaging resolution.

2. Effects of Errors in Determining Σ: In the model in Fig. 11(e), the boundary Σ is scaled down by 10%. In Fig. 11(f), a random component is added to the real boundary, which is implemented by multiplying the real radii of a boundary with uniform random numbers within $[0.8, 1.2]$. After comparing Figs. 11(e) and (f) with other components of Fig. 11, it is found that compensation is less sensitive to error in determining Σ as v_p. This is because a 10% error, which is about 6 mm in the diameter of the parenchyma wall, adds an error of at most 0.42 mm to the PSW and BSW according to (30).

VI. DISCUSSION

A. Effect of Small Fat Lobules

In breast UT, centimeter-scale fat lobules in the parenchyma tissue also can cause significant distortion. In breast TAT, the amplitude distortion due to centimeter-scale fat lobules is estimated to be insignificant because of the diffraction effect, as discussed in Section III-A,2. For example, substituting $a = 1$ cm, $\lambda = 1.5$ mm in (13), we obtain a near-field length of 6.7 cm. Therefore, no strong amplitude distortion is expected when detectors are placed farther than 6.7 cm from the lobule. In addition, Figs. 6 (b)–(d) show that the images of point sources outside an acoustic heterogeneity are affected little by the acoustic heterogeneity due to the completeness of the π-view detection in TAT. This explanation also can be applied to the distortion caused by fat lobules. When a fat lobule on one side of an acoustic source causes severe distortion, the signals that are spared from severe distortion in other directions still can produce good images.

B. Determine v_f and v_p in Experiments

Our simulation results in Fig. 10(c) and Fig. 11(c) show that a 1% error in v_f and v_p will lead to minor blurring but that we still have enough definition to determine the configuration and location of the imaged objects. To determine v_f and v_p within 1% accuracy, we can try different speeds around the averages, which are 1437 m/s and 1546 m/s for fat and breast tissue, respectively, with a step size of 1% velocity. Optimum speeds can be determined by choosing the reconstructed image with the sharpest parenchyma wall, because errors in v_f and v_p will cause the spread of this boundary. Because the variations of v_f and v_p between individuals are about 2% and 4%, respectively, only 15 trials are needed to scan all the combinations. Furthermore, the backprojection method [12] can be used in each trial because the boundary of the reconstructed image can be recovered well with this method [34], [35]. Therefore, the additional computation cost in the trials is estimated to be only double the total computation complexity.

C. Determine Σ in Experiments

There are two ways to obtain Σ. The first method uses only TAT signals. It takes advantage of the fact that fat and parenchyma have both acoustic and microwave contrasts. A TAT image is first reconstructed with an acoustically homogeneous model. Then an approximate Σ can be extracted from the image and plugged into an acoustically heterogeneous reconstruction model to obtain a more accurate TAT image. As shown in Fig. 6, the boundary spread of the parenchyma wall in TAT images is at most 7% of its real size (if $\alpha = 0.07$) when an acoustically homogeneous reconstruction model is used. Our studies of the effects on the reconstruction of the errors in the boundary profile, shown in Fig. 10(e) and Fig. 11(e), reveal that this level of error has little effect on the images reconstructed from a heterogeneous model. We intend to implement this method in our future work.

The second method for determining Σ is the coregistration of ultrasound B-scan imaging and TAT. In principle, this can be accomplished in the same set-up. The TAT data is acquired, then the transducers work in pulse-echo mode to determine an approximate Σ. This boundary information can be included in the reconstruction algorithm of TAT.

D. Differences Between TAT and UT

The studies we presented in Section III show that there should be no severe amplitude distortion in breast TAT, but severe amplitude distortion caused by refraction has been observed in both narrowband and broadband breast UT [15]. The difference between the effects of acoustic heterogeneity on TAT and UT can be explained by the different central frequencies. In UT, the central frequency

is above 3 MHz, and in TAT the central frequency is below 1 MHz. The higher frequency in UT results in stronger wavefront distortion due to the following reasons. First, the scattering effect increases rapidly with frequency; second, the minimum detection distance for avoiding strong amplitude distortion caused by an acoustic lens, which can be a boundary segment or a small inclusion, extends farther with increasing frequency. Substituting the following parameters for UT, $l_{SB_1} < 10$ cm, $\lambda = 0.5$ mm, and $\alpha = 0.07$ into (20), we have $l_{B_1 D} > 9.8$ cm. We notice that the transducer or array was placed closer than the required distance to the breast [15], [16]. Therefore, it is not surprising to observe the strong interference effect in UT.

Another important difference between TAT and UT is that there is no speckle in our TAT images [11]. Speckle is an important factor limiting the quality of pure ultrasonic imaging. In our technology, the detected signals are primary acoustic waves rather than reflective or scattered waves as in UT. Furthermore, the temporal frequency of the acoustic signals lies in a range from 0 to 1.5 MHz, which is only weakly scattered in the tissues. However, the issue of image speckle in more realistic medical imaging applications is a topic for future consideration.

E. Miscellaneous

Our analysis and numerical simulations have shown that breast TAT images can survive acoustic heterogeneity. The ultimate test, however, will come from clinical experiments on the breast in which the motion artifacts due to breathing and cardiac movement may introduce blurring. Such blurring of images is estimated to be on the order of the movement amplitude. To correct the blurring, we can monitor the breast motion, for example, placing a microwave absorber on the breast surface as a marker. Then the data on the breast motion can be used in the reconstructions to shift the detectors' positions and, consequently, compensate for the breast's displacement.

VII. CONCLUSIONS

The effects of acoustic heterogeneity on TAT in the breast are studied. Our analysis shows that the amplitude distortion in the breast TAT is minor. There is no multipath interference in the breast TAT with a convex parenchyma wall, and the amplitude distortion also is not severe for concave boundary, because the TAT signals are broadband, have low central frequency, and experience only one-way transmission through the parenchyma wall. Therefore we consider only phase distortion in our numerical studies. The numerical results on the spread of point sources and boundaries caused by the phase distortion are in good agreement with the predictions of the proposed formula. It is shown that phase distortion can be compensated for when complete or partial information on the distribution of acoustic velocity in the breast is included in the reconstruction. It is found that improvement in the re-

sults is more sensitive to measurement error in v_f, v_p than Σ. Based on this sensitivity study, an approach to implement our compensation method using only TAT data is proposed. The differences between breast TAT and breast ultrasound imaging in relation to the effects of acoustic heterogeneity and speckles are accounted for by differences in their central frequency of ultrasound and detection configuration.

APPENDIX A
DERIVATION OF (11)

Assume that the concave boundary can be approximated by an arch with a radius $R_l > a$, where a is half the size of the boundary segment. Two rays are refracted at points B_1 and B_2 in Fig. 4, where B_2 has a small displacement from B_1 along the boundary. According to the refraction law, we have:

$$\sin\theta_1 = (1-\alpha)\sin\phi_1,$$
$$\cos\theta_1 d\theta_1 = (1-\alpha)\cos\phi_1 d\phi_1, \tag{32}$$

where $d\phi_1$ is the difference between the incidence angles of the two rays and $d\theta_1$ is the transmission one. They can be expressed as:

$$d\theta_1 = \left(1 - \frac{R_l\cos\theta_1}{l_{B_1 D}}\right)d\theta,$$
$$d\phi_1 = \left(\frac{R_l\cos\phi_1}{l_{SB_1}} + 1\right)d\theta, \tag{33}$$

where l_{SB_1} and $l_{B_1 D}$ are the distances from the boundary point B_1 to source S and detector D, respectively, and $d\theta = l_{B_1 B_2}/R_l$. Combining the above equations, we have the imaging formula for the boundary segment:

$$\frac{\cos^2}{l_{SB_1}} + \frac{\cos^2\theta_1}{l_{DB_1}(1-\alpha)} = \frac{\cos\theta_1/(1-\alpha)-\cos\phi_1}{R_l}. \tag{34}$$

Because in our breast model $\alpha \approx 0.1$ is small, the above equation can be further simplified to (11) after using $\theta_1 \approx \phi_1$.

APPENDIX B
DERIVATION OF (30)

The first iteration in TCG is equivalent to the backprojection method [34]. In backprojection for an acoustically homogeneous TAT, $p(\mathbf{r}, t)$, the signal detected at $\mathbf{r}$ and time t is projected back to a sphere with a radius of tv_{s0} and a center at $\mathbf{r}$. It is shown that the boundaries of objects can be reconstructed correctly with the backprojection method [35]. Let us consider a model illustrated in Fig. 7 to estimate the spread of source S along line $D_1 D_2$, where D_1 and D_2 are two detectors, S_1 is the intersection of $D_1 D_2$ with the backprojection arch of the

signal transmitted by source S and detected by detector D_1, S_2 is the corresponding one at D_2, and Σ represents the parenchyma wall. If there is no error in computing TOFs, S_1, S_2, and S will be one point; therefore, a point image of source S can be recovered. In an acoustically heterogeneous model, however, the flight-time errors caused by the approximation of v_p by v_{s0} in the reconstruction result in the splitting of S_1 and S_2 from S, where $l_{S_1 S}$ and $l_{S_2 S}$ can be estimated by the multiplication of the flight-time errors with v_{s0}, $l_{S_1 S} = l_{B_1 S}(1 - v_{s0}/v_p) = \alpha l_{B_1 S}$ and $l_{S_2 S} = l_{B_2 S}(l - v_{s0}/v_p) = \alpha l_{B_2 S}$. Combining them, we have (30) for the spread width of source S along line $D_1 D_2$. Similar analysis can be applied to estimating BSW as well.

ACKNOWLEDGMENTS

REFERENCES

[1] W. Joines, R. Jirtle, M. Rafal, and D. Schaeffer. "Microwave power absorption differences between normal and malignant tissue," Radiation Oncology-Biology-Physics, vol. 6, pp. 681–687, 1980.

[2] S. Chaudhary, R. Mishra, A. Swarup, and J. Thomas, "Dielectric properties of normal human breast tissues at radiowave and microwave frequencies," Indian J. Biochem. Biophys., vol. 21, pp. 76–79, 1984.

[3] W. Joines, Y. Zhang, C. Li, and R. Jirtle, "The measured electrical properties of normal and malignant human tissues from 50–900 MHz," Med. Phys., vol. 21, pp. 547–550, 1994.

[4] L. E. Larsen and J. H. Jacobi, Eds. Medical Applications of Microwave Imaging. Piscataway, NJ: IEEE Press, 1986.

[5] S. Caorsi, A. Frattoni, G. L. Gragnani, E. Nortino, and M. Pastorino, "Numerical algorithm for dielectric-permittivity microwave imaging of inhomogeneous biological bodies," Med. Biol. Eng. Comput., vol. NS-29, pp. 37–44, 1991.

[6] M. S. Hawley, A. Broquetas, L. Jofre, J. C. Bolomey, and G. Gaboriaud, "Microwave imaging of tissue blood content changes," J. Biomed. Eng., vol. 13, pp. 197–202, 1991.

[7] P. M. Meaney, K. D. Paulsen, and J. T. Chang, "Near-field microwave imaging of biologically-based materials using a monopole transceiver system," IEEE Trans. Microwave Theory Tech., vol. 46, pp. 31–45, 1998.

[8] R. A. Kruger, P. Liu, Y. R. Fang, and C. R. Appledorn, "Photoacoustic ultrasound (PAUS)—reconstruction tomography," Med. Phys., vol. 22, pp. 1605–1609, 1995.

[9] C. G. A. Hoelen, F. F. M. Demul, R. Pongers, and A. Dekker, "Three-dimensional photoacoustic imaging of blood vessels in tissue," Op. Lett., vol. 23, pp. 648–650, 1998.

[10] G. Ku and L.-H. V. Wang, "Scanning thermoacoustic tomography in biological tissue," Med. Phys., vol. 27, pp. 1195–1202, 2000.

[11] Y. Xu, D. Feng, and L.-H. V. Wang, "Exact frequency-domain reconstruction for thermoacoustic tomography: 1. Planar geometry," IEEE Trans. Med. Imag., vol. 21, pp. 823–828, 2002.

[12] M. Xu and L.-H. V. Wang, "Time-domain reconstruction for thermoacoustic tomography in a spherical geometry," IEEE Trans. Med. Imag., vol. 21, pp. 814–822, 2002.

[13] Y. Xu, M. Xu, and L.-H. V. Wang, "Exact frequency-domain reconstruction for thermoacoustic tomography: II. Cylindrical geometry," IEEE Trans. Med. Imag., vol. 21, pp. 829–833, 2002.

[14] M. Moshfeghi and R. C. Waag, "In vivo and in vitro ultrasound beam distortion measurements of a large aperture and a conventional aperture focused transducer," *Ultrasound Med. Biol.*, vol. 5, pp. 415–428, 1988.

[15] Q. Zhu and B. D. Steinberg, "Large-transducer measurements of wavefront distortion in the female breast," *Ultrason. Imag.*, vol. 14, pp. 276–299, 1992.

[16] C. W. Manry and S. L. Broschat, "FDTD simulations for ultrasound propagation in a 2-D breast model," *Ultrason. Imag.*, vol. 18, pp. 25–34, 1996.

[17] P. D. Freiburger, D. C. Sullivan, B. H. Leblanc, S. W. Smith, and G. E. Trahey, "Two dimensional ultrasonic beam distortion in the breast: In vivo measurements and effects," *Ultrason. Imag.*, vol. 14, pp. 398–414, 1992.

[18] S. W. Flax and M. O'Donnell, "Phase aberration correction using signals from point reflectors and diffuse scatterers: Basic principles," *IEEE Trans. Ultrason., Ferroelect., Freq. Contr.*, vol. 35, pp. 758–767, 1988.

[19] G. E. Trahey, D. Zhao, J. A. Miglin, and S. W. Smith, "Experimental results with a real-time adaptive ultrasonic imaging system for viewing through distorting media," *IEEE Trans. Ultrason., Ferroelect., Freq. Contr.*, vol. 37, pp. 418–427, 1990.

[20] Q. Zhu and B. D. Steinberg, "Deaberration of incoherent wavefront distortion: An approach toward inverse filtering," *IEEE Trans. Ultrason., Ferroelect., Freq. Contr.*, vol. 44, pp. 575–589, 1997.

[21] Y. Xu and L.-H. V. Wang, "Signal processing in scanning thermoacoustic tomography in biological tissues," *Med. Phys.*, vol. 28, pp. 1519–1524, 2001.

[22] P. C. Hansen, *Rank-Deficient and Discrete Ill—Posed Problems*. Philadelphia, PA: SIAM Press, 1998.

[23] A. V. Oppenheim and J. S. Lim, "The importance of phase in signals," *Proc. IEEE*, pp. 529–541, 1981.

[24] B. D. Steinberg, "A theory of the effect of hard limiting and other distortions upon the quality of microwave images," *IEEE Trans. Acoust. Speech Signal Processing*, vol. ASSP-35, pp. 1462–1472, 1987.

[25] V. E. Gusev and A. A. Karabutov, *Laser Optoacoustics*. New York: American Institute of Physics, 1993.

[26] A. R. Selfridge, "Approximate properties in isotropic materials," *IEEE Trans. Sonics Ultrason.*, vol. SU-32, pp. 381–394, 1985.

[27] F. S. Foster, M. Strban, and G. Austin, "The ultrasound microscope: Initial studies of the breast tissue," *Ultrason. Imag.*, vol. 6, pp. 243–261, 1984.

[28] M. Born and E. Wolf, *Principles of Optics*. New York: Cambridge University Press, 1997.

[29] L. A. Chernov, *Wave Propagation in a Random Medium*. New York: Dover, 1960.

[30] G. Kossoff, E. K. Fry, and J. Jellins, "Average velocity of ultrasound in the human female breast," *J. Acoust. Soc. Amer.*, vol. 53, pp. 1730–1736, 1973.

[31] R. Sneider and D. F. Aldridge, "Perturbation theory for travel times," *J. Acoust. Soc. Amer.*, vol. 98, pp. 1565–1569, 1995.

[32] H. P. William, A. T. Saul, T. V. William, and P. F. Brian, *Numerical Recipes in C*. Cambridge: Cambridge Univ. Press, 1992.

[33] J. F. Greenleaf and R. C. Bahn, "Clinical imaging with transmissive ultrasonic computerized tomography," *IEEE Trans. Biomed. Eng.*, vol. BME-28, no. 2, pp. 177–185, 1981.

[34] Y. Xu and L.-H. V. Wang, "Limited-view thermoacoustic tomography and reconstruction by truncated-conjugate gradient," *IEEE Trans. Med. Imag.*, submitted for publication.

[35] A. K. Louis and E. T. Quinto, "Local tomographic methods in sonar," in *Surveys on Solution Methods for Inverse Problems*. Vienna: Springer, 2000, pp. 147–154.

Yuan Xu was born in Guangshui, China in 1971, received his Ph.D. degree in physics from the Institute of Physics, Chinese Academy of Sciences, Beijing, China, in 1999. He is studying for a Ph.D. degree in Biomedical Engineering at Texas A&M University, College Station, Texas.

His research interest is thermoacoustic tomography.

Lihong V. Wang (M'96-SM'00) was born in Guangshui, China on March 8, 1964, received his Ph.D. degree in electrical engineering from Rice University, Houston, TX, in 1992.

Dr. Wang worked for Dr. Steven Jacques initially as a postdoctoral research associate and was shortly promoted to assistant professor at the University of Texas M. D. Anderson Cancer Center, Houston, TX, a top-ranked cancer institution. He was promoted to professor in biomedical and electrical engineering, Texas A&M University, College Station, TX, in 2002.

He is a senior member of the Institute of Electrical and Electronics Engineers (IEEE), and a member of the American Physical Society (APS), Society of Photo-Optical Instrumention Engineers (SPIE), Optical Society of America (OSA), and Engineering in Medicine and Biology Society (EMBS). He received the National Institutes of Health (NIH) First award, National Science Foundation (NSF) Career award, Johnson & Johnson Outstanding Young Scientist award, Texas A&M Texas Engineering Experiment Station (TEES) Select Young Faculty award, Texas A&M TEES Faculty Fellow award (twice), Texas A&M Ernest A. Baetz Faculty Fellow award, and Texas A&M University Faculty Fellow award. He is listed in *Who's Who in Science and Engineering*. He served as a grant reviewer for NIH, NSF, the Navy, and other funding agencies. He is an associate editor for the *Annals of Biomedical Engineering, Journal of Biomedical Optics*, and *Applied Optics*.